Helicity evolution at small x: Revised asymptotic results at large N_c and N_f

Daniel Adamiak,[1,2,*] Yuri V. Kovchegov,[1,†] and Yossathorn Tawabutr[1,3,4,‡]

[1]*Department of Physics, The Ohio State University, Columbus, Ohio 43210, USA*
[2]*Jefferson Lab, Newport News, Virginia 23606, USA*
[3]*Department of Physics, University of Jyväskylä, P.O. Box 35, 40014 University of Jyväskylä, Finland*
[4]*Helsinki Institute of Physics, P.O. Box 64, 00014 University of Helsinki, Finland*

(Received 12 June 2023; accepted 8 August 2023; published 7 September 2023)

We present a numerical solution of the revised version [J. High Energy Phys. 07 (2022) 095] of the small-x helicity evolution equations from [J. High Energy Phys. 01 (2016) 072, Phys. Rev. D **99**, 054032 (2019)] at large N_c and N_f. (Here N_c and N_f are the numbers of quark colors and flavors, respectively.) The evolution equations are double-logarithmic in the Bjorken x variable, resumming powers of $\alpha_s \ln^2(1/x)$ with α_s the strong coupling constant. The large-N_c & N_f evolution we consider includes contributions of small-x quark emissions and is thus more realistic than the large-N_c one, which only involves gluon emissons. The evolution equations [J. High Energy Phys. 07 (2022) 095, J. High Energy Phys. 01 (2016) 072, Phys. Rev. D **99**, 054032 (2019)] are written for the so-called “polarized dipole amplitudes,” which are related to the helicity distribution functions and the g_1 structure function. Unlike the previously reported solution [J. High Energy Phys. 08 (2020) 014] of the earlier version of helicity evolution equations at large N_c & N_f [J. High Energy Phys. 01 (2016) 072, Phys. Rev. D **99**, 054032 (2019)], our solution does not exhibit periodic oscillations in $\ln(1/x)$ for $N_f < 2N_c$, while only showing occasional sign reversals. For $N_f = 2N_c$, we report oscillations with $\ln(1/x)$, similar to those found earlier in [J. High Energy Phys. 08 (2020) 014]. We determine the intercept of our evolution for $N_f < 2N_c$ as well as the parameters of the oscillatory behavior for $N_f = 2N_c$. We compare our results to the existing resummation [Z. Phys. C **72**, 627 (1996)] and finite-order calculations for helicity-dependent quantities in the literature.

DOI: 10.1103/PhysRevD.108.054005

I. INTRODUCTION

Small Bjorken x behavior of helicity-dependent observables has received a considerable amount of attention in recent years [1–17], with the aim of constraining the amount of the proton spin carried by the partons in that region of phase space. Apart from being a question of general interest in our understanding of the proton structure, the knowledge of helicity distributions at low x may help us solve the proton spin puzzle [18–26]. Indeed, the helicity parton distribution functions (hPDFs) for quarks ($\Delta\Sigma(x, Q^2)$, which is flavor-singlet) and gluons [$\Delta G(x, Q^2)$], when integrated over all x, give us the contributions of the quark (S_q) and gluon (S_G) helicities to the proton spin,

$$S_q(Q^2) = \frac{1}{2}\int_0^1 dx\, \Delta\Sigma(x, Q^2),$$
$$S_G(Q^2) = \int_0^1 dx\, \Delta G(x, Q^2). \tag{1}$$

These contributions, in turn, enter the spin sum rules [27] (see also [28])

$$S_q + L_q + S_G + L_G = \frac{1}{2}, \tag{2}$$

along with the orbital angular momenta (OAM) carried by the quarks (L_q) and gluons (L_G). The proton spin puzzle is a question of determining the values of all the ingredients (S_q, S_G, L_q, and L_G) of the sum rule (2) at some sufficiently high value of the resolution scale Q^2. In addition, it would be very interesting to determine the x-distributions of $\Delta\Sigma(x, Q^2)$ and $\Delta G(x, Q^2)$ (along with the similar x-dependent quantities for L_q and L_G [29–33]), to learn which regions in x carry most of the proton spin.

The efforts to develop a theoretical formalism describing and predicting helicity distributions at low x began with the pioneering work by Bartels, Ermolaev and

---

[*] adamiak.5@osu.edu
[†] kovchegov.1@osu.edu
[‡] yossathorn.j.tawabutr@jyu.fi

Ryskin (BER) [34,35] employing the infrared evolution equations (IREE) approach [36–40]. The calculation [34,35] was done in the double-logarithmic approximation (DLA), resumming powers of $\alpha_s \ln^2(1/x)$. It led to helicity phenomenology developed in [41–46].

In the more recent works [1–10,12–14,16], the question of the small-x helicity asymptotics was addressed using a different approach based on the shock wave/s-channel evolution formalism originally developed in [47–59] to describe the unpolarized eikonal scattering (see [60–67] for reviews and [3,9,68–80] for generalizations of the formalism to the subeikonal and sub-subeikonal observables). Helicity evolution equations in DLA for the subeikonal "polarized dipole amplitudes" were constructed in [2,3,6,9] (KPS) (see also [14]), with important corrections and modifications found more recently in [1] (KPS-CTT). The equations [1–3,6,9] close in the large-N_c (cf. [50–53]) and the large-N_c & N_f limits. Beyond those limits, a helicity version of the Jalilian-Marian–Iancu–McLerran–Weigert–Leonidov–Kovner (JIMWLK) [54–59] functional evolution equation was constructed in [12], though corrections from [1] have not yet been implemented for it.

Numerical and analytic solutions of the large-N_c version of KPS-CTT evolution were constructed in [1,17], respectively. The resulting small-x behavior of hPDFs was found to be of the power-law type,

$$\Delta\Sigma(x, Q^2) \sim \Delta G(x, Q^2) \sim \left(\frac{1}{x}\right)^{\alpha_h}, \tag{3}$$

with the power α_h, also known as the intercept, found explicitly, $\alpha_h \approx 3.66\sqrt{\frac{\alpha_s N_c}{2\pi}}$. While the numerical solution from [1] appeared to be in good quantitative agreement with the pure-glue limit of the earlier work by BER [34], the analytical solution found in [17] revealed differences between KPS-CTT evolution and BER. The differences appeared in the third decimal point in the intercept (that is, beyond the numerical precision achieved in [1]) and starting from four loops in the resummed polarized anomalous dimension $\Delta\gamma_{GG}(\omega)$ [17].

The KPS version of the large-N_c & N_f helicity evolution was solved numerically in [4]. In that reference, the resulting hPDF were found to exhibit an oscillatory behavior as functions of $\ln(1/x)$, in addition to the power-of-$1/x$ growth, similar to that in Eq. (3), of the amplitude of those oscillations. The goal of this paper is to revise [4] in light of the corrected KPS-CTT evolution constructed in [1]. Below we solve the revised large-N_c & N_f helicity evolution equations numerically and obtain the resulting small-x asymptotics for hPDFs and for the g_1 structure function. We find that the oscillations in $\ln(1/x)$, found in [4], are absent in the solution of the modified evolution [1] for $N_f < 2N_c$, but reappear for $N_f = 2N_c$. This appears to be slightly different from BER, whose evolution does not lead to any oscillations in hPDFs for $N_f \leq 2N_c$. In addition, for all values of $N_f \leq 2N_c$, the polarized dipole amplitudes resulting from the revised evolution [1], along with the corresponding hPDFs, do exhibit an occasional sign reversal, similar to that observed by BER in [34] for the nonzero N_c & N_f version of their IREE. We also compare the intercepts we find in the large-N_c & N_f limit to the same limit of BER intercepts for different values of N_f/N_c: as shown in Table IV, we find the two sets of intercepts very close, yet slightly different from each other, continuing the trend found in [17] at large N_c.

The paper is structured as follows. We present the equations we want to solve in Sec. II, along with the expression relating the polarized dipole amplitudes to hPDFs and the g_1 structure function. The details of the numerical solution are given in Sec. III, where we show the results of our calculations and obtain the intercepts for different values of N_f/N_c. We also demonstrate that for $N_f = 2N_c$ oscillations tend to re-appear in the revised evolution. We run several cross-checks in Sec. IV, by modifying the initial conditions and by verifying the target–projectile symmetry of the polarized dipole amplitudes. (The latter was never shown to be valid for the original KPS evolution.) We further compare our results to the finite-order exact perturbative calculations [81–92] in Sec. V. We conclude in Sec. VI.

II. SMALL-x HELICITY EVOLUTION EQUATIONS

As we mentioned above, a set of small-x evolution equations has been derived in [1–3] by applying the saturation/ color glass condensate (CGC) framework [60–67] to the helicity-dependent subeikonal contributions to the amplitudes for a color-dipole scattering on a longitudinally polarized target proton. In particular, one of the (anti)quarks in the dipole, whose helicity is tracked through its interaction with the polarized target, interacts with the target with the S-matrix corresponding to the so-called subeikonal *polarized* Wilson line, $V^{\text{pol}}_{\underline{x}',\underline{x};\sigma',\sigma}$. Here, the polarized (anti)quark is incident with helicity σ and transverse position $\underline{x}$, interacts with the target at the helicity-dependent, subeikonal level and leaves the interaction with helicity σ' and transverse position $\underline{x}'$. More details about the polarized Wilson line will be outlined below. On the other hand, the other (anti)quark in the dipole interacts with the target with the S-matrix simply corresponding to the infinite eikonal light-cone Wilson line, $V_{\underline{x}} = V_{\underline{x}}[\infty, -\infty]$, with

$$V_{\underline{x}}[x_f^-, x_i^-] = \mathcal{P} \exp\left[ig \int_{x_i^-}^{x_f^-} dx^- A^+(0^+, x^-, \underline{x})\right], \tag{4}$$

where $\mathcal{P}$ is the path-ordering operator and $A^\mu = \sum_a A^{a\mu} t^a$ is the background gluon field with t^a's the $\mathrm{SU}(N_c)$

generators in the fundamental representation. We also define similarly the adjoint-representation counterpart of the finite-length light-cone Wilson line as

$$U_{\underline{x}}[x_f^-, x_i^-] = \mathcal{P}\exp\left[ig\int_{x_i^-}^{x_f^-} dx^- \mathcal{A}^+(0^+, x^-, \underline{x})\right], \tag{5}$$

where $\mathcal{A}^\mu = \sum_a A^{a\mu} T^a$ with T^a's the $\mathrm{SU}(N_c)$ generators in the adjoint representation. Out light-cone variables are defined as $x^\pm = (t \pm z)/\sqrt{2}$, while the transverse vectors are denoted by $\underline{x} = (x^1, x^2)$.

The polarized Wilson line can be further decomposed into the *type-1* and *type-2* terms, with different helicity structure, such that [1,3]

$$V^{\mathrm{pol}}_{\underline{x}', \underline{x}; \sigma', \sigma} = \sigma \delta_{\sigma\sigma'} V^{\mathrm{pol}[1]}_{\underline{x}} \delta^2(\underline{x} - \underline{x}') + \delta_{\sigma\sigma'} V^{\mathrm{G}[2]}_{\underline{x}', \underline{x}}. \tag{6}$$

The type-1 polarized Wilson line can be further decomposed into the quark- and gluon-exchange terms,

$$V^{\mathrm{pol}[1]}_{\underline{x}} = V^{\mathrm{q}[1]}_{\underline{x}} + V^{\mathrm{G}[1]}_{\underline{x}}. \tag{7}$$

As for the type-2 counterpart, only the gluon-exchange term contributes to helicity. The three subeikonal terms in the polarized Wilson line can be written in terms of subeikonal operators and the finite-length light-cone Wilson lines as [1,3]

$$V^{\mathrm{q}[1]}_{\underline{x}} = \frac{g^2 P^+}{2s}\int_{-\infty}^{\infty} dx_1^- \int_{x_1^-}^{\infty} dx_2^- V_{\underline{x}}[\infty, x_2^-] t^b \psi_\beta(x_2^-, \underline{x}) U^{ba}_{\underline{x}}[x_2^-, x_1^-](\gamma^+\gamma^5)_{\alpha\beta} \bar{\psi}_\alpha(x_1^-, \underline{x}) t^a V_{\underline{x}}[x_1^-, -\infty], \tag{8a}$$

$$V^{\mathrm{G}[1]}_{\underline{x}} = \frac{igP^+}{s}\int_{-\infty}^{\infty} dx^- V_{\underline{x}}[\infty, x^-] F^{12}(x^-, \underline{x}) V_{\underline{x}}[x^-, -\infty], \tag{8b}$$

$$V^{\mathrm{G}[2]}_{\underline{x}', \underline{x}} = -\frac{iP^+}{s}\int_{-\infty}^{\infty} dx^- d^2 z\, V_{\underline{x}'}[\infty, x^-] \delta^2(\underline{x}' - \underline{z}) \overleftarrow{D}^i(x^-, \underline{z}) \vec{D}^i(x^-, \underline{z}) V_{\underline{x}}[x^-, -\infty] \delta^2(\underline{x} - \underline{z}). \tag{8c}$$

Here $F^{\mu\nu}$ is the gluon field strength tensor, $\vec{D}^i = \partial^i - igA^i$ and $\overleftarrow{D}^i = \overleftarrow{\partial}^i + igA^i$ are the right- and left-acting covariant derivatives ($i = 1, 2$), P^+ is the large momentum of the (proton) target, and s is the center-of-mass energy squared for the projectile–target scattering. Furthermore, the type-2 polarized Wilson line relates to the following operator [1],

$$V^{i\mathrm{G}[2]}_{\underline{x}} = \frac{P^+}{2s}\int_{-\infty}^{\infty} dx^-\, V_{\underline{x}}[\infty, x^-] \times \left[\vec{D}^i(x^-, \underline{x}) - \overleftarrow{D}^i(x^-, \underline{x})\right] V_{\underline{x}}[x^-, -\infty]. \tag{9}$$

The helicity evolution equations are derived in terms of these polarized Wilson lines and their adjoint counterparts. Similarly to the unpolarized Balitsky–Kovchegov (BK) [50–53]/JIMWLK [54–59] evolution equations, the helicity evolution equations do not close in general. Particularly, each iteration in the general evolution equations leads to more complicated forms of multipole operators, which differ from the original dipole operator. However, the evolution becomes closed and yields predictive power once the large-N_c [93] or the large-N_c & N_f limit [94] is taken. (Here, N_f is the number of quark flavor.) While the former is studied in [1,17], in this paper we focus on the large-N_c & N_f limit of the evolution equations.

A. Large-N_c & N_f limit

In the large-N_c & N_f limit, we take N_c and N_f to be large, while their ratio, N_f/N_c is fixed to a constant [94]. In the context of small-x evolution, application of the large-N_c & N_f limit is outlined in [1–3]. First, we define the fundamental dipole amplitudes of type 1 and type 2, which correspond to the respective types of polarized Wilson lines, as

$$\begin{aligned} Q(x_{10}^2, zs) &= \int d^2\left(\frac{x_0 + x_1}{2}\right) Q_{10}(zs) \\ &= \int d^2\left(\frac{x_0 + x_1}{2}\right) \frac{1}{2N_c} \mathrm{Re}\langle\langle \mathrm{T\,tr}\left[V_{\underline{0}} V^{\mathrm{pol}[1]\dagger}_{\underline{1}}\right] + \mathrm{T\,tr}\left[V^{\mathrm{pol}[1]}_{\underline{1}} V^\dagger_{\underline{0}}\right] \rangle\rangle(zs), \end{aligned} \tag{10a}$$

$$\begin{aligned} G_2(x_{10}^2, zs) &= \frac{\epsilon^{ik} x_{10}^k}{x_{10}^2} \int d^2\left(\frac{x_0 + x_1}{2}\right) G^i_{10}(zs) \\ &= \frac{\epsilon^{ik} x_{10}^k}{x_{10}^2} \int d^2\left(\frac{x_0 + x_1}{2}\right) \frac{1}{2N_c} \mathrm{Re}\langle\langle \mathrm{T\,tr}\left[V_{\underline{0}} V^{i\mathrm{G}[2]\dagger}_{\underline{1}}\right] + \mathrm{T\,tr}\left[V^{i\mathrm{G}[2]}_{\underline{1}} V^\dagger_{\underline{0}}\right] \rangle\rangle(zs), \end{aligned} \tag{10b}$$

where $V_{\underline{i}} = V_{\underline{x}_i}$ for $i = 0, 1, \ldots$, $\underline{x}_{ij} = \underline{x}_i - \underline{x}_j$, and $x_{ij} = |\underline{x}_{ij}|$. Here, the unpolarized (anti)quark in the dipole is located at $\underline{x}_0$, while the polarized (anti)quark is located at $\underline{x}_1$. The variable z (roughly) denotes the minus momentum fraction of the softest parton in a dipole. The double angle brackets denote the standard CGC averaging applied to the longitudinally polarized target and multiplied by zs, that is $\langle\langle \ldots \rangle\rangle = zs\langle \ldots \rangle$; in this rescaling z denotes the longitudinal momentum fraction of the polarized parton in the dipole. As shown in [1], the prefactor, $\epsilon^{ik} x_{10}^k / x_{10}^2$, in Eq. (10b) is chosen so as to project out the components that contribute to helicity evolution ($i, k = 1, 2$). Furthermore, we also need to consider the adjoint dipole amplitude of type 1, whose operator structure in the quark sector and evolution differ from that of its fundamental counterpart in a nontrivial manner. In the large-N_c & N_f limit where gluons are approximated by color-octet quark-antiquark pairs, the "fundamental part" of the adjoint type-1 dipole is defined by [1]

$$\begin{aligned}\tilde{G}(x_{10}^2, zs) &= \int d^2\left(\frac{\underline{x}_0 + \underline{x}_1}{2}\right) \tilde{G}_{10}(zs) \\ &= \int d^2\left(\frac{\underline{x}_0 + \underline{x}_1}{2}\right) \frac{1}{2N_c} \mathrm{Re}\langle\langle \mathrm{T\,tr}\left[V_{\underline{0}} W_{\underline{1}}^{\mathrm{pol}[1]\dagger}\right] + \mathrm{T\,tr}\left[W_{\underline{1}}^{\mathrm{pol}[1]} V_{\underline{0}}^{\dagger}\right] \rangle\rangle(zs),\end{aligned} \tag{11}$$

where

$$W_{\underline{x}}^{\mathrm{pol}[1]} = V_{\underline{x}}^{\mathrm{G}[1]} + \frac{g^2 P^+}{8s} \int_{-\infty}^{\infty} dx_1^- \int_{x_1^-}^{\infty} dx_2^- V_{\underline{x}}[\infty, x_2^-] \psi_\beta(x_2^-, \underline{x}) (\gamma^+ \gamma_5)_{\alpha\beta} \bar{\psi}_\alpha(x_1^-, \underline{x}) V_{\underline{x}}[x_1^-, -\infty]. \tag{12}$$

In addition to the three dipole amplitudes, the evolution will also lead to dipole amplitudes with the same operator definitions as Q, $\tilde{G}$, and G_2, but whose physical transverse size does not match the transverse size that determines the cutoff on the longitudinal lifetime for further evolution [1–3]. This leads to the definition of *neighbor dipole amplitudes* $\bar{\Gamma}(x_{10}^2, x_{32}^2, zs)$, $\tilde{\Gamma}(x_{10}^2, x_{32}^2, zs)$ and $\Gamma_2(x_{10}^2, x_{32}^2, zs)$ as the dipole amplitudes, Q, $\tilde{G}$ and G_2, respectively, with physical dipole transverse size x_{10} and lifetime $\sim x_{32}^2 z$ [1–3,6,9]. Note that these neighbor dipole amplitudes only appear (become needed) in the region where $x_{10} \gg x_{32}$.

Altogether, with six amplitudes in total, the large-N_c & N_f evolution equations become a system of six linear integral equations, namely [1]

$$\begin{aligned}Q(x_{10}^2, zs) = Q^{(0)}(x_{10}^2, zs) &+ \frac{\alpha_s N_c}{2\pi} \int_{\max\{\Lambda^2/s, 1/x_{10}^2 s\}}^{z} \frac{dz'}{z'} \int_{1/z's}^{x_{10}^2} \frac{dx_{21}^2}{x_{21}^2} \Big[2\tilde{\Gamma}(x_{10}^2, x_{21}^2, z's) + 2\tilde{G}(x_{21}^2, z's) \\ &+ Q(x_{21}^2, z's) - \bar{\Gamma}(x_{10}^2, x_{21}^2, z's) + 2\Gamma_2(x_{10}^2, x_{21}^2, z's) + 2G_2(x_{21}^2, z's)\Big] \\ &+ \frac{\alpha_s N_c}{4\pi} \int_{\Lambda^2/s}^{z} \frac{dz'}{z'} \int_{1/z's}^{x_{10}^2 z/z'} \frac{dx_{21}^2}{x_{21}^2} \Big[Q(x_{21}^2, z's) + 2G_2(x_{21}^2, z's)\Big],\end{aligned} \tag{13a}$$

$$\begin{aligned}\bar{\Gamma}(x_{10}^2, x_{21}^2, z's) = Q^{(0)}(x_{10}^2, z's) &+ \frac{\alpha_s N_c}{2\pi} \int_{\max\{\Lambda^2/s, 1/x_{10}^2 s\}}^{z'} \frac{dz''}{z''} \int_{1/z''s}^{\min\{x_{10}^2, x_{21}^2 z'/z''\}} \frac{dx_{32}^2}{x_{32}^2} [2\tilde{\Gamma}(x_{10}^2, x_{32}^2, z''s) \\ &+ 2\tilde{G}(x_{32}^2, z''s) + Q(x_{32}^2, z''s) - \bar{\Gamma}(x_{10}^2, x_{32}^2, z''s) + 2\Gamma_2(x_{10}^2, x_{32}^2, z''s) + 2G_2(x_{32}^2, z''s)\Big] \\ &+ \frac{\alpha_s N_c}{4\pi} \int_{\Lambda^2/s}^{z} \frac{dz''}{z''} \int_{1/z''s}^{x_{21}^2 z'/z''} \frac{dx_{32}^2}{x_{32}^2} \Big[Q(x_{32}^2, z''s) + 2G_2(x_{32}^2, z''s)\Big],\end{aligned} \tag{13b}$$

$$\begin{aligned}\tilde{G}(x_{10}^2, zs) = \tilde{G}^{(0)}(x_{10}^2, zs) &+ \frac{\alpha_s N_c}{2\pi} \int_{\max\{\Lambda^2/s, 1/x_{10}^2 s\}}^{z} \frac{dz'}{z'} \int_{1/z's}^{x_{10}^2} \frac{dx_{21}^2}{x_{21}^2} \Big[\bar{\Gamma}(x_{10}^2, x_{21}^2, z's) + 3\tilde{G}(x_{21}^2, z's) \\ &+ 2G_2(x_{21}^2, z's) + 2\Gamma_2(x_{10}^2, x_{21}^2, z's)\Big] \\ &- \frac{\alpha_s N_f}{8\pi} \int_{\Lambda^2/s}^{z} \frac{dz'}{z'} \int_{1/z's}^{x_{10}^2 z/z'} \frac{dx_{21}^2}{x_{21}^2} \Big[\bar{\Gamma}^{\mathrm{gen}}(x_{20}^2, x_{21}^2, z's) + 2\Gamma_2^{\mathrm{gen}}(x_{20}^2, x_{21}^2, z's)\Big],\end{aligned} \tag{13c}$$

$$\tilde{\Gamma}(x_{10}^2, x_{21}^2, z's) = \tilde{G}^{(0)}(x_{10}^2, zs) + \frac{\alpha_s N_c}{2\pi} \int_{\max\{\Lambda^2/s, 1/x_{10}^2 s\}}^{z'} \frac{dz''}{z''} \int_{1/z''s}^{\min\{x_{10}^2, x_{21}^2 z'/z''\}} \frac{dx_{32}^2}{x_{32}^2} \Big[\tilde{\Gamma}(x_{10}^2, x_{32}^2, z''s)$$
$$+ 3\tilde{G}(x_{32}^2, z''s) + 2G_2(x_{32}^2, z''s) + 2\Gamma_2(x_{10}^2, x_{32}^2, z''s)\Big]$$
$$- \frac{\alpha_s N_f}{8\pi} \int_{\Lambda^2/s}^{z'} \frac{dz''}{z''} \int_{1/z''s}^{x_{21}^2 z'/z''} \frac{dx_{32}^2}{x_{32}^2} \Big[\bar{\Gamma}^{\text{gen}}(x_{30}^2, x_{32}^2, z''s) + 2\Gamma_2^{\text{gen}}(x_{30}^2, x_{32}^2, z''s)\Big], \tag{13d}$$

$$G_2(x_{10}^2, zs) = G_2^{(0)}(x_{10}^2, zs) + \frac{\alpha_s N_c}{\pi} \int_{\Lambda^2/s}^{z} \frac{dz'}{z'} \int_{\max\{x_{10}^2, 1/z's\}}^{x_{10}^2 z/z'} \frac{dx_{21}^2}{x_{21}^2} \Big[\tilde{G}(x_{21}^2, z's) + 2G_2(x_{21}^2, z's)\Big], \tag{13e}$$

$$\Gamma_2(x_{10}^2, x_{21}^2, z's) = G_2^{(0)}(x_{10}^2, z's) + \frac{\alpha_s N_c}{\pi} \int_{\Lambda^2/s}^{z' x_{21}^2/x_{10}^2} \frac{dz''}{z''} \int_{\max\{x_{10}^2, 1/z''s\}}^{x_{21}^2 z'/z''} \frac{dx_{32}^2}{x_{32}^2} \Big[\tilde{G}(x_{32}^2, z''s) + 2G_2(x_{32}^2, z''s)\Big], \tag{13f}$$

where we defined the *generalized dipole amplitudes* as [9]

$$\bar{\Gamma}^{\text{gen}}(x_{10}^2, x_{32}^2, z''s) = \theta(x_{32} - x_{10}) Q(x_{10}^2, z''s) + \theta(x_{10} - x_{32}) \bar{\Gamma}(x_{10}^2, x_{32}^2, z''s) \tag{14a}$$

$$\Gamma_2^{\text{gen}}(x_{10}^2, x_{32}^2, z''s) = \theta(x_{32} - x_{10}) G_2(x_{10}^2, z''s) + \theta(x_{10} - x_{32}) \Gamma_2(x_{10}^2, x_{32}^2, z''s). \tag{14b}$$

In the above equations Λ is the scale characterizing the target proton, s is the center-of-mass energy squared for the projectile-target scattering, z is the fraction of the projectile's momentum carried by the softest parton in the dipole 10, while z' and z'' are similar fractions for the dipoles 21 and 32, respectively.

In our formalism, the g_1 structure function relates to the fundamental polarized dipole amplitudes Q and G_2 through the relation [1]

$$g_1(x, Q^2) = -\frac{N_c}{4\pi^3} \sum_f Z_f^2 \int_{\Lambda^2/s}^{1} \frac{dz}{z} \int_{1/zs}^{\min\{\frac{1}{zQ^2}, \frac{1}{\Lambda^2}\}} \frac{dx_{10}^2}{x_{10}^2} \Big[Q(x_{10}^2, zs) + 2G_2(x_{10}^2, zs)\Big], \tag{15}$$

where Z_f is the fractional charge of the quarks and the sum goes over flavors. Furthermore, the flavor-singlet quark and gluon helicity PDFs relate to the polarized dipole amplitudes by [1]

$$\Delta\Sigma(x, Q^2) = -\frac{N_c N_f}{2\pi^3} \int_{\Lambda^2/s}^{1} \frac{dz}{z} \int_{1/zs}^{\min\{\frac{1}{zQ^2}, \frac{1}{\Lambda^2}\}} \frac{dx_{10}^2}{x_{10}^2} \Big[Q(x_{10}^2, zs) + 2G_2(x_{10}^2, zs)\Big], \tag{16a}$$

$$\Delta G(x, Q^2) = \frac{2N_c}{\alpha_s \pi^2} \left[1 + x_{10}^2 \frac{\partial}{\partial x_{10}^2}\right] G_2\left(x_{10}^2, zs = \frac{Q^2}{x}\right)\bigg|_{x_{10}^2 = 1/Q^2} \approx \frac{2N_c}{\alpha_s \pi^2} G_2\left(x_{10}^2, zs = \frac{Q^2}{x}\right)\bigg|_{x_{10}^2 = 1/Q^2}. \tag{16b}$$

When writing Eqs. (15) and (16) we have been treating Λ as the infrared (IR) cutoff, as was done in [1], and not as a scale characterizing the target, as was assumed in Eq. (16b). The last step in Eq. (16b) is valid with the DLA accuracy. In Eq. (16a) we have assumed for simplicity that the dipole amplitudes are independent of quark flavors.

Eqs. (15) and (16) allow us to perform all the small-x calculation in terms of the polarized dipole amplitudes, from which the g_1 structure function and the helicity PDFs can be computed in the final step.

B. Initial conditions

In performing realistic phenomenology, the initial conditions for the small-x helicity evolution have to be deduced from the data at moderate values of Bjorken x [15]. However, this is a complicated problem in its own right and is beyond the scope of this paper. Instead, in order to obtain the asymptotic behaviors of helicity PDFs and g_1 structure function at small x, we simplify the issue by employing two different approximations to the initial conditions—the Born-level approximation and the constant approximation.

The Born-level approximation has been utilized in previous works of similar nature [1,4,7], both at large N_c and large N_c & N_f. However, to properly apply it to the large N_c & N_f evolution equation (13), we need to make a slight change described below.

In Eq. (13), Λ is taken to be an energy scale in the process characterizing the typical transverse momentum in the target. This is in contrast to the treatment in the large-N_c limit, where the corresponding distance scale $1/\Lambda$ is used as the infrared cutoff for the dipole size. Particularly, in our treatment of Eq. (13) the dipole can grow larger than $1/\Lambda$.

This leads to a necessary modification to the Born-level initial conditions. In particular, for fixed impact parameter the dipole amplitude of each type can be written at the Born level as [1,3,6,9]

$$Q_{10}^{(0)}(zs) = \tilde{G}_{10}^{(0)}(zs) = \frac{\alpha_s^2 C_F}{2N_c}\left[\frac{C_F}{|\underline{x}_1-\underline{b}_1|^2} - 2\pi\delta^2(\underline{x}_1-\underline{b}_1)\ln(zsx_{10}^2)\right], \tag{17a}$$

$$G_{10}^{i(0)}(zs) = -\frac{\alpha_s^2 C_F}{N_c}\epsilon^{ij}\frac{(\underline{x}_1^j-\underline{b}^j)}{|\underline{x}_1-\underline{b}|^2}\ln\frac{|\underline{x}_1-\underline{b}|}{|\underline{x}_0-\underline{b}|}. \tag{17b}$$

These results follow from the calculation of the helicity-dependent amplitude of the quark- and gluon-exchange diagrams for the dipole projectile interacting with a quark target located at position $\underline{b}$ in the transverse plane. In the previous works, Eq. (17) were integrated over $b_\perp$ up to $1/\Lambda$, which acted as the infrared cutoff. In this work, however, we must allow $b_\perp$ to exceed $1/\Lambda$. In order to still keep one of the integrals finite, we introduce a lower energy scale, $\Lambda_{\mathrm{IR}} \ll \Lambda$, such that the integrals over $b_\perp$ will go up to $1/\Lambda_{\mathrm{IR}}$. Doing so and modifying the polarized target from being a single polarized quark to a polarized dipole of the transverse size $\approx 1/\Lambda$ averaged over all angles leads to the following impact parameter-integrated Born-level initial conditions we will employ in this work,

$$Q^{(0)}(x_{10}^2, zs) = \tilde{G}^{(0)}(x_{10}^2, zs) = \frac{\alpha_s^2 C_F}{2N_c}\pi\left[C_F\ln\frac{zs}{\Lambda_{\mathrm{IR}}^2} - 2\ln\left(zs\min\left\{x_{10}^2, \frac{1}{\Lambda^2}\right\}\right)\right], \tag{18a}$$

$$G_2^{(0)}(x_{10}^2, zs) = -\frac{\alpha_s^2 C_F}{2N_c}\pi\left[\theta\left(\frac{1}{\Lambda}-x_{10}\right)\ln\frac{1}{x_{10}^2\Lambda^2} + \theta\left(x_{10}-\frac{1}{\Lambda}\right)\frac{1}{x_{10}^2\Lambda^2}\right] \approx -\frac{\alpha_s^2\pi C_F}{2N_c}\theta\left(\frac{1}{\Lambda}-x_{10}\right)\ln\frac{1}{x_{10}^2\Lambda^2}. \tag{18b}$$

This provides a relatively realistic approximation to the initial conditions. The second term in Eq. (18b) is not going to source DLA evolution in the equation (13), under the assumptions used in deriving these equations [1]: while a more comprehensive treatment would have required modifying Eq. (13) for the dipoles with $x_{10} > 1/\Lambda$, here we will neglect this contribution since it is suppressed by at least one logarithm compared to the contribution we have kept in Eq. (18b).

In the previous numerical solutions for the small-x helicity evolution of similar nature [1,4,7] it was observed that the asymptotic solution in the small-x region quickly becomes independent of the initial conditions, with only the overall normalization of the solution dependent on the initial conditions. This inspires an even more simplified approximation to the initial conditions, which we will call the *constant approximation* or the all-one approximation, in which we simply take

$$Q^{(0)}(x_{10}^2, zs) = \tilde{G}^{(0)}(x_{10}^2, zs) = G_2^{(0)}(x_{10}^2, zs) = 1. \tag{19}$$

Most of the numerical computation in this work will be done using the constant approximation to the initial conditions. In order to verify that it produces the same asymptotic results as the more physical Born-level approximation, we will perform several cross checks below, the results of which will be presented in Sec. IV A.

III. NUMERICAL SOLUTION

As shown in [1], parton helicity TMDs and PDFs, together with the g_1 structure function, all depend only on $Q(x_{10}^2, zs)$ and $G_2(x_{10}^2, zs)$. Hence, the main goal of this Section is to study the asymptotic form of these dipole amplitudes as zs grows large [4,7]. Owing to the complexity of the large-N_c & N_f evolution equation (13), only a numerical solution has been developed.

A. Discretization and recursive form

Since the small-x helicity evolution is double-logarithmic in $1/x$, with logarithms of x coming from both the transverse and longitudinal integrals, we begin our numerical computation by defining the following variables,

$$\eta = \sqrt{\frac{\alpha_s N_c}{2\pi}}\ln\frac{zs}{\Lambda^2}, \qquad \eta' = \sqrt{\frac{\alpha_s N_c}{2\pi}}\ln\frac{z's}{\Lambda^2} \quad \text{and} \quad \eta'' = \sqrt{\frac{\alpha_s N_c}{2\pi}}\ln\frac{z''s}{\Lambda^2},$$
$$s_{10} = \sqrt{\frac{\alpha_s N_c}{2\pi}}\ln\frac{1}{x_{10}^2\Lambda^2}, \qquad s_{21} = \sqrt{\frac{\alpha_s N_c}{2\pi}}\ln\frac{1}{x_{21}^2\Lambda^2} \quad \text{and} \quad s_{32} = \sqrt{\frac{\alpha_s N_c}{2\pi}}\ln\frac{1}{x_{32}^2\Lambda^2}. \tag{20}$$

With these changes of variables applied to the longitudinal momentum fractions and the transverse dipole sizes, we rewrite Eq. (13) as

$$
\begin{aligned}
Q(s_{10},\eta) &= Q^{(0)}(s_{10},\eta) + \frac{1}{2}\int_0^{\eta} d\eta' \int_{s_{10}+\eta'-\eta}^{\eta'} ds_{21}\Big[Q(s_{21},\eta') + 2G_2(s_{21},\eta')\Big] \\
&\quad + \int_{\max\{0,s_{10}\}}^{\eta} d\eta' \int_{s_{10}}^{\eta'} ds_{21}\Big[2\tilde{G}(s_{21},\eta') + 2\tilde{\Gamma}(s_{10},s_{21},\eta') + Q(s_{21},\eta') - \bar{\Gamma}(s_{10},s_{21},\eta') + 2\Gamma_2(s_{10},s_{21},\eta') \\
&\quad + 2G_2(s_{21},\eta')\Big],
\end{aligned}
\tag{21a}
$$

$$
\begin{aligned}
\bar{\Gamma}(s_{10},s_{21},\eta') &= Q^{(0)}(s_{10},\eta') + \frac{1}{2}\int_0^{\eta'} d\eta'' \int_{s_{21}+\eta''-\eta'}^{\eta''} ds_{32}\Big[Q(s_{32},\eta'') + 2G_2(s_{32},\eta'')\Big] \\
&\quad + \int_{\max\{0,s_{10}\}}^{\eta'} d\eta'' \int_{\max\{s_{10},s_{21}+\eta''-\eta'\}}^{\eta''} ds_{32}\Big[2\tilde{G}(s_{32},\eta'') + 2\tilde{\Gamma}(s_{10},s_{32},\eta'') + Q(s_{32},\eta'') - \bar{\Gamma}(s_{10},s_{32},\eta'') \\
&\quad + 2\Gamma_2(s_{10},s_{32},\eta'') + 2G_2(s_{32},\eta'')\Big],
\end{aligned}
\tag{21b}
$$

$$
\begin{aligned}
\tilde{G}(s_{10},\eta) &= \tilde{G}^{(0)}(s_{10},\eta) - \frac{N_f}{4N_c}\int_0^{\eta} d\eta' \int_{s_{10}+\eta'-\eta}^{\min\{s_{10},\eta'\}} ds_{21}\Big[Q(s_{21},\eta') + 2G_2(s_{21},\eta')\Big] \\
&\quad + \int_{\max\{0,s_{10}\}}^{\eta} d\eta' \int_{s_{10}}^{\eta'} ds_{21}\Big[3\tilde{G}(s_{21},\eta') + \tilde{\Gamma}(s_{10},s_{21},\eta') + 2G_2(s_{21},\eta') + 2\Gamma_2(s_{10},s_{21},\eta') \\
&\quad - \frac{N_f}{4N_c}\bar{\Gamma}(s_{10},s_{21},\eta') - \frac{N_f}{2N_c}\Gamma_2(s_{10},s_{21},\eta')\Big],
\end{aligned}
\tag{21c}
$$

$$
\begin{aligned}
\tilde{\Gamma}(s_{10},s_{21},\eta') &= \tilde{G}^{(0)}(s_{10},\eta') - \frac{N_f}{4N_c}\int_0^{\eta'+s_{10}-s_{21}} d\eta'' \int_{s_{21}+\eta''-\eta'}^{\min\{s_{10},\eta''\}} ds_{32}\Big[Q(s_{32},\eta'') + 2G_2(s_{32},\eta'')\Big] \\
&\quad + \int_{\max\{0,s_{10}\}}^{\eta'} d\eta'' \int_{\max\{s_{10},s_{21}+\eta''-\eta'\}}^{\eta''} ds_{32}\Big[3\tilde{G}(s_{32},\eta'') + \tilde{\Gamma}(s_{10},s_{32},\eta'') + 2G_2(s_{32},\eta'') + 2\Gamma_2(s_{10},s_{32},\eta'') \\
&\quad - \frac{N_f}{4N_c}\bar{\Gamma}(s_{10},s_{32},\eta'') - \frac{N_f}{2N_c}\Gamma_2(s_{10},s_{32},\eta'')\Big],
\end{aligned}
\tag{21d}
$$

$$
G_2(s_{10},\eta) = G_2^{(0)}(s_{10},\eta) + 2\int_0^{\eta} d\eta' \int_{s_{10}+\eta'-\eta}^{\min\{s_{10},\eta'\}} ds_{21}\Big[\tilde{G}(s_{21},\eta') + 2G_2(s_{21},\eta')\Big],
\tag{21e}
$$

$$
\Gamma_2(s_{10},s_{21},\eta') = G_2^{(0)}(s_{10},\eta') + 2\int_0^{\eta'+s_{10}-s_{21}} d\eta'' \int_{s_{21}+\eta''-\eta'}^{\min\{s_{10},\eta''\}} ds_{32}\Big[\tilde{G}(s_{32},\eta'') + 2G_2(s_{32},\eta'')\Big].
\tag{21f}
$$

In obtaining Eq. (21), the ordering $s_{10} \le s_{21} \le \eta'$ was assumed in the arguments of $\bar{\Gamma}$, $\tilde{\Gamma}$, and Γ_2. This is the only region where $\bar{\Gamma}$, $\tilde{\Gamma}$, and Γ_2 appear in any large-N_c & N_f evolution kernel, where the subsequent evolution lifetime in the daughter dipole 20 depends on the smallest transverse distance scale x_{21} in the splitting. Along the way, we also separated the integrals from Eqs. (13c) and (13d) that involve the generalized dipole amplitudes, cf. Eq. (14), into the regions where they reduce to the corresponding ordinary and neighbor dipole amplitudes.

Now, we discretize the integrals in Eq. (21) with step size δ in both directions and define the discretized dipole amplitudes as

$$
\begin{aligned}
Q_{ij} &= Q(i\delta, j\delta), & \bar{\Gamma}_{ikj} &= \bar{\Gamma}(i\delta, k\delta, j\delta), \\
\tilde{G}_{ij} &= \tilde{G}(i\delta, j\delta), & \tilde{\Gamma}_{ikj} &= \tilde{\Gamma}(i\delta, k\delta, j\delta), \\
G_{2,ij} &= G_2(i\delta, j\delta), & \Gamma_{2,ikj} &= \Gamma_2(i\delta, k\delta, j\delta).
\end{aligned}
\tag{22}
$$

As a result, we obtain the following discretized evolution equations,

$$Q_{ij} = Q^{(0)}_{ij} + \frac{1}{2}\delta^2 \sum_{j'=0}^{j-1} \sum_{i'=i+j'-j}^{j'-1} \left[Q_{i'j'} + 2G_{2,i'j'} \right] \\ + \delta^2 \sum_{j'=\max\{0,i\}}^{j-1} \sum_{i'=i}^{j'-1} \left[2\tilde{G}_{i'j'} + 2\tilde{\Gamma}_{ii'j'} + Q_{i'j'} - \bar{\Gamma}_{ii'j'} + 2\Gamma_{2,ii'j'} + 2G_{2,i'j'} \right], \tag{23a}$$

$$\bar{\Gamma}_{ikj} = Q^{(0)}_{ij} + \frac{1}{2}\delta^2 \sum_{j'=0}^{j-1} \sum_{i'=k+j'-j}^{j'-1} \left[Q_{i'j'} + 2G_{2,i'j'} \right] \\ + \delta^2 \sum_{j'=\max\{0,i\}}^{j-1} \sum_{i'=\max\{i,k+j'-j\}}^{j'-1} \left[2\tilde{G}_{i'j'} + 2\tilde{\Gamma}_{ii'j'} + Q_{i'j'} - \bar{\Gamma}_{ii'j'} + 2\Gamma_{2,ii'j'} + 2G_{2,i'j'} \right], \tag{23b}$$

$$\tilde{G}_{ij} = \tilde{G}^{(0)}_{ij} - \frac{N_f}{4N_c}\delta^2 \sum_{j'=0}^{j-1} \sum_{i'=i+j'-j}^{\min\{i,j'\}-1} \left[Q_{i'j'} + 2G_{2,i'j'} \right] \\ + \delta^2 \sum_{j'=\max\{0,i\}}^{j-1} \sum_{i'=i}^{j'-1} \left[3\tilde{G}_{i'j'} + \tilde{\Gamma}_{ii'j'} + 2G_{2,i'j'} + 2\Gamma_{2,ii'j'} - \frac{N_f}{4N_c}\bar{\Gamma}_{ii'j'} - \frac{N_f}{2N_c}\Gamma_{2,ii'j'} \right], \tag{23c}$$

$$\tilde{\Gamma}_{ikj} = \tilde{G}^{(0)}_{ij} - \frac{N_f}{4N_c}\delta^2 \sum_{j'=0}^{i+j-k-1} \sum_{i'=k+j'-j}^{\min\{i,j'\}-1} \left[Q_{i'j'} + 2G_{2,i'j'} \right] \\ + \delta^2 \sum_{j'=\max\{0,i\}}^{j-1} \sum_{i'=\max\{i,k+j'-j\}}^{j'-1} \left[3\tilde{G}_{i'j'} + \tilde{\Gamma}_{ii'j'} + 2G_{2,i'j'} + 2\Gamma_{2,ii'j'} - \frac{N_f}{4N_c}\bar{\Gamma}_{ii'j'} - \frac{N_f}{2N_c}\Gamma_{2,ii'j'} \right], \tag{23d}$$

$$G_{2,ij} = G^{(0)}_{2,ij} + 2\delta^2 \sum_{j'=0}^{j-1} \sum_{i'=i+j'-j}^{\min\{i,j'\}-1} \left[\tilde{G}_{i'j'} + 2G_{2,i'j'} \right], \tag{23e}$$

$$\Gamma_{2,ikj} = G^{(0)}_{2,ij} + 2\delta^2 \sum_{j'=0}^{i+j-k-1} \sum_{i'=k+j'-j}^{\min\{i,j'\}-1} \left[\tilde{G}_{i'j'} + 2G_{2,i'j'} \right]. \tag{23f}$$

Through a careful consideration of Eq. (23), we see that we need to know the values of the following dipole amplitudes in the following regions to determine the values of Q_{ij}, $\tilde{G}_{ij}$ and $G_{2,ij}$ for $0 \le i \le i_{\max}$ and $0 \le j \le j_{\max}$:

(i) Q_{ij}, $\tilde{G}_{ij}$, and $G_{2,ij}$ such that $0 \le j \le j_{\max}$ and $j - j_{\max} \le i \le j$, while also keeping $i \le i_{\max}$.

(ii) $\bar{\Gamma}_{ikj}$, $\tilde{\Gamma}_{ikj}$ and $\Gamma_{2,ikj}$ such that $0 \le i \le k \le j$, with $0 \le j \le j_{\max}$ and $j - j_{\max} \le i \le k \le j$, while keeping $k \le i_{\max}$. This is partly because the neighbor dipole amplitudes only appear in Eqs. (23a)–(23d).

Furthermore, the numerical computation becomes more efficient once we realize recursive relations coming from equation (23). For Q_{ij}, $\tilde{G}_{ij}$, and $G_{2,ij}$, we retrieve the initial conditions in the case where $i = j$. For $i < j$, we can re-write Eqs. (23a), (23c), and (23e) recursively as

$$Q_{ij} = Q^{(0)}_{ij} - Q^{(0)}_{i(j-1)} + Q_{i(j-1)} + \frac{1}{2}\delta^2 \sum_{i'=i-1}^{j-2} \left[Q_{i'(j-1)} + 2G_{2,i'(j-1)} \right] + \frac{1}{2}\delta^2 \sum_{j'=0}^{j-2} \left[Q_{(i+j'-j)j'} + 2G_{2,(i+j'-j)j'} \right] \\ + \delta^2 \sum_{i'=i}^{j-2} \left[2\tilde{G}_{i'(j-1)} + 2\tilde{\Gamma}_{ii'(j-1)} + Q_{i'(j-1)} - \bar{\Gamma}_{ii'(j-1)} + 2\Gamma_{2,ii'(j-1)} + 2G_{2,i'(j-1)} \right], \tag{24a}$$

$$\tilde{G}_{ij} = \tilde{G}^{(0)}_{ij} - \tilde{G}^{(0)}_{i(j-1)} + \tilde{G}_{i(j-1)} - \frac{N_f}{4N_c}\delta^2\left[Q_{(i-1)(j-1)} + 2G_{2,(i-1)(j-1)}\right] - \frac{N_f}{4N_c}\delta^2\sum_{j'=0}^{j-2}\left[Q_{(i+j'-j)j'} + 2G_{2,(i+j'-j)j'}\right]$$
$$+ \delta^2\sum_{i'=i}^{j-2}\left[3\tilde{G}_{i'(j-1)} + \tilde{\Gamma}_{ii'(j-1)} + 2G_{2,i'(j-1)} + 2\Gamma_{2,ii'(j-1)} - \frac{N_f}{4N_c}\bar{\Gamma}_{ii'(j-1)} - \frac{N_f}{2N_c}\Gamma_{2,ii'(j-1)}\right], \tag{24b}$$

$$G_{2,ij} = G^{(0)}_{2,ij} - G^{(0)}_{2,i(j-1)} + G_{2,i(j-1)} + 2\delta^2\left[\tilde{G}_{(i-1)(j-1)} + 2G_{2,(i-1)(j-1)}\right] + 2\delta^2\sum_{j'=0}^{j-2}\left[\tilde{G}_{(i+j'-j)j'} + 2G_{2,(i+j'-j)j'}\right]. \tag{24c}$$

Note that we need to have $j > 0$ in order to have $i < j$.

Turning to $\bar{\Gamma}_{ikj}$, $\tilde{\Gamma}_{ikj}$, and $\Gamma_{2,ikj}$, we note that they similarly reduce to their ordinary dipole counterparts Q_{ij}, $\tilde{G}_{ij}$, and $G_{2,ij}$, respectively, when $i = k$. For $i < k$, Eqs. (23b), (23d) and (23f) can be written in recursive forms as

$$\bar{\Gamma}_{ikj} = Q^{(0)}_{ij} - Q^{(0)}_{i(j-1)} + \bar{\Gamma}_{i(k-1)(j-1)} + \frac{1}{2}\delta^2\sum_{i'=k-1}^{j-2}\left[Q_{i'(j-1)} + 2G_{2,i'(j-1)}\right]$$
$$+ \delta^2\sum_{i'=\max\{i,k-1\}}^{j-2}\left[2\tilde{G}_{i'(j-1)} + 2\tilde{\Gamma}_{ii'(j-1)} + Q_{i'(j-1)} - \bar{\Gamma}_{ii'(j-1)} + 2\Gamma_{2,ii'(j-1)} + 2G_{2,i'(j-1)}\right], \tag{25a}$$

$$\tilde{\Gamma}_{ikj} = \tilde{G}^{(0)}_{ij} - \tilde{G}^{(0)}_{i(j-1)} + \tilde{\Gamma}_{i(k-1)(j-1)}$$
$$+ \delta^2\sum_{i'=\max\{i,k-1\}}^{j-2}\left[3\tilde{G}_{i'(j-1)} + \tilde{\Gamma}_{ii'(j-1)} + 2G_{2,i'(j-1)} + 2\Gamma_{2,ii'(j-1)} - \frac{N_f}{4N_c}\bar{\Gamma}_{ii'(j-1)} - \frac{N_f}{2N_c}\Gamma_{2,ii'(j-1)}\right], \tag{25b}$$

$$\Gamma_{2,ikj} = G^{(0)}_{2,ij} - G^{(0)}_{2,i(j-1)} + \Gamma_{2,i(k-1)(j-1)}. \tag{25c}$$

In the case where $j = 0$, we have $0 = i = k = j$. Consequently, the neighbor dipole amplitudes reduce to their respective initial conditions, as can also be seen directly from Eq. (23).

Notice that the first sum in Eq. (23d), containing the term $Q_{i'j'} + 2G_{2,i'j'}$, does not survive in Eq. (25b). There are two reasons for this, which depend on the values of i, j and k. In particular, if $i + j - k - 1 \geq 0$, then the summation term remains the same once we simultaneously reduce j and k by 1. On the other hand, in the case where $i + j - k - 1 < 0$, which is possible for $i < 0$, the specified term in Eq. (23d) simply vanishes because the upper limit of the sum over j' is now below the corresponding lower limit. As a result, the recursive form in Eq. (25b) holds true in both regimes.

Similar to the computation at large N_c, for each step size, δ, and maximum rapidity, $\eta_{\max}$, we start by computing each dipole amplitude at $j = 0$ using the respective initial condition (the inhomogeneous term). Then, we compute their values at $j = 1$ based on the values at $j = 0$, with the help of Eqs. (24) and (25). Afterwards, the $j = 2$ values can similarly be computed based on the $j = 1$ values, etc. The recursive relations (24) and (25) allow us to calculate the six polarized dipole amplitudes all the way up to $\eta = \eta_{\max}$. For each η, we need to compute the amplitudes for all s_{10} (and s_{21}, if applicable) in the $\eta - \eta_{\max} \leq s_{10} \leq s_{21} \leq \eta$ region [4]. This is due to the fact that the soft-quark emission terms in Eqs. (24a), (24b), (25a) and (25b) have logarithmic divergence in different transverse position regions from their soft-gluon emission counterparts.

Our numerical solution indicates that the asymptotic behavior of the results differs qualitatively between the cases where $N_f \leq 5$ and $N_f = 6$ (both with $N_c = 3$). This warrants separating the discussion of the results into two respective sections, one for each case. In Sec. III B we discuss the numerical solution in the $N_f \leq 5$ case, while the $N_f = 6$ case is discussed in Sec. III C. Note that we are solving the large-N_c & N_f evolution equations: in that limit both N_c and N_f are very large, and only their ratio N_f/N_c is fixed. Here and below, when we talk about particular values of N_f and N_c, this should be understood only as fixing the ratio N_f/N_c while assuming that both N_c and N_f are large. For instance, when we choose $N_f = 4$ and $N_c = 3$, this only implies that $N_f/N_c = 4/3$, and should not be thought of as fixing the values of N_c and N_f.

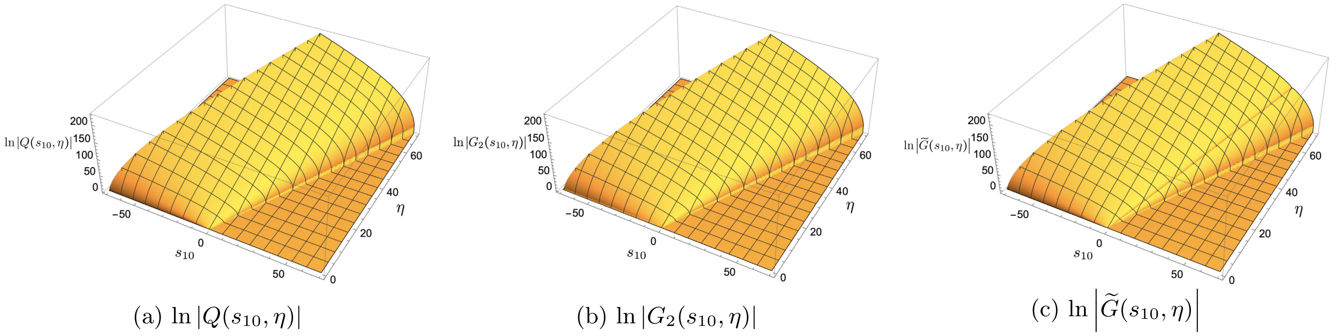

(a) $\ln|Q(s_{10},\eta)|$ (b) $\ln|G_2(s_{10},\eta)|$ (c) $\ln\left|\widetilde{G}(s_{10},\eta)\right|$

FIG. 1. The plots of logarithms of the absolute values of polarized dipole amplitudes Q, G_2 and $\tilde{G}$ at $N_f = 4$ and $N_c = 3$ versus s_{10} and η, for in the $-\eta_{\max} \leq s_{10} \leq \eta_{\max}$, $0 \leq \eta \leq \eta_{\max}$ region with $\eta_{\max} = 70$. The amplitudes are computed numerically using the step size $\delta = 0.1$.

B. Solution for $N_f \leq 5$

Performing the iterative computation outlined in Sec. III A, we obtain the numerical values of $Q(s_{10},\eta)$, $G_2(s_{10},\eta)$ and $\tilde{G}(s_{10},\eta)$ at various s_{10} and η on the grid. In order to extract their large-η asymptotic form, which will later be useful to determine small-x asymptotics of helicity PDFs, additional steps must be performed to the raw numerical results. To describe the subsequent process more clearly, we consider a sample run with step size $\delta = 0.1$ and maximum rapidity $\eta_{\max} = 70$. As for the number of flavors, we first consider $N_f = 4$, which is qualitatively similar to any $N_f \leq 5$. The procedure will be similar for other δ and $\eta_{\max}$ [1,4,7]. Note that we fix the number of quark colors at $N_c = 3$ throughout our large-N_c & N_f calculation, in the sense of the comment made above that only the ratio N_f/N_c is truly fixed.

Furthermore, throughout this Section, we employ the constant "all-one" approximation of initial condition, which upon discretization takes the form,

$$Q_{ij}^{(0)} = \tilde{G}_{ij}^{(0)} = G_{2,ij}^{(0)} = 1. \tag{26}$$

A more detailed discussion about the choices of initial conditions, including a justification for our simplified choice (26), will be given in the next section.

The main goal of this section is two-fold. First, we determine the asymptotic forms of $Q(0,\eta)$, $G_2(0,\eta)$ and $\tilde{G}(0,\eta)$, that is, we only fit the polarized dipole amplitudes along the $s_{10} = 0$ line. These results will provide sufficient ingredients for us to obtain the asymptotic form of helicity PDFs and the g_1 structure function at small x, which is the second part of our goal.

At $N_f = 4$, we perform the numerical computation described above to obtain the dipole amplitudes Q, $\tilde{G}$, and G_2. The logarithms of absolute values of these amplitudes are plotted in Fig. 1 versus η and s_{10}. As mentioned above, these amplitudes are calculated with step size $\delta = 0.1$ and maximum rapidity $\eta_{\max} = 70$. Qualitatively, the plots in Figs. 1(a) and 1(b) indicate the exponential growth with η along the $s_{10} = 0$ line. However, we see a line of cusp in the plot for $\tilde{G}$, which is a new feature not seen in any of the amplitudes in previous similar works [1,4,7]. This cusp only appears in the positive-s_{10} region.

To further understand the results, we plot each amplitude at $s_{10} = 0$ in Fig. 2, with the exception of Fig. 2c for $\tilde{G}$, which contains blue dots for $s_{10} = 0$ and orange dots for $s_{10} = 30$. For each of the plots, the quantity in the vertical axis is the sign of the amplitude multiplied by the logarithm of the absolute value of the amplitude. In the plot for $\tilde{G}$ at

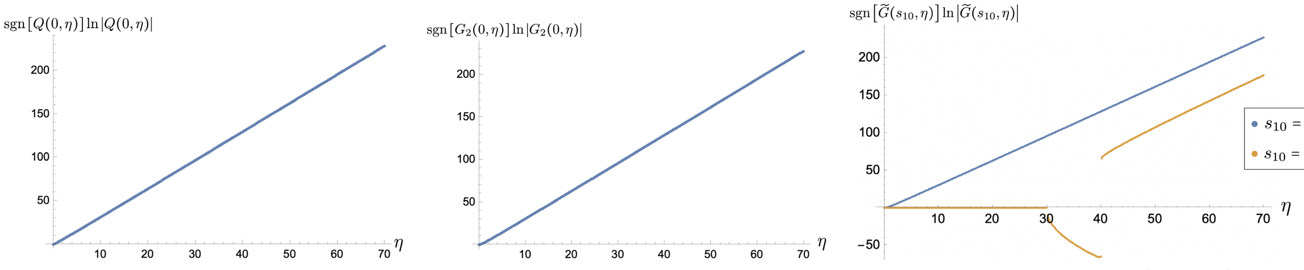

(a) $\mathrm{sgn}[Q(0,\eta)]\ln|Q(0,\eta)|$ (b) $\mathrm{sgn}[G_2(0,\eta)]\ln|G_2(0,\eta)|$ (c) $\mathrm{sgn}\left[\widetilde{G}(0,\eta)\right]\ln\left|\widetilde{G}(0,\eta)\right|$

FIG. 2. The plots of logarithms of the absolute values of polarized dipole amplitudes Q, G_2 and $\tilde{G}$, multiplied by the amplitudes' signs, along the $s_{10} = 0$ line (for all amplitudes) and along the $s_{10} = 30$ line for $\tilde{G}$, versus the rapidity η. The amplitudes are computed numerically with $N_f = 4$, $N_c = 3$ in the range $0 \leq \eta \leq \eta_{\max} = 70$ using step size $\delta = 0.1$.

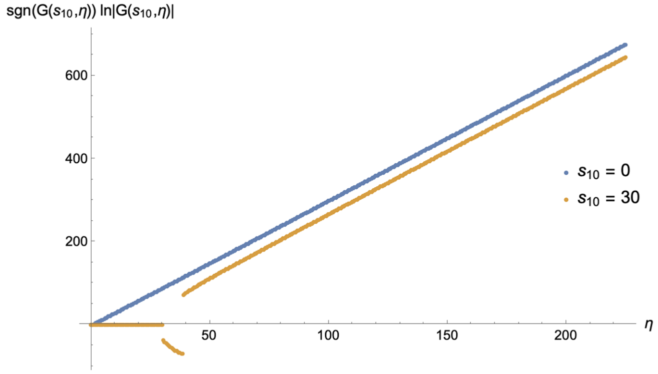

FIG. 3. The plot of the logarithm of the absolute value of polarized dipole amplitude $\tilde{G}$ multiplied by the amplitude's sign along the $s_{10} = 0$ line (blue dots) and the $s_{10} = 30$ line (orange dots), versus the rapidity, η. The amplitudes are computed numerically with $N_f = 4$, $N_c = 3$ in the range $0 \leq \eta \leq \eta_{\max} = 225$ using the step size $\delta = 0.5$.

$s_{10} = 30$, we see that $\tilde{G}(30, \eta)$ grows from the initial condition toward negative values as $\eta > 30$. Now, as η grows past a value near 40, the sign of the amplitude flips and becomes positive once more, while its magnitude keeps growing exponentially. The sign flip appears only once at least up to the maximum rapidity of $\eta_{\max} = 70$, as shown in Fig. 2c. Furthermore, we also confirm this fact of a single sign flip for up to $\eta = 225$ in a separate run with $\delta = 0.5$ and $\eta_{\max} = 225$, whose result for $\tilde{G}(30, \eta)$ is shown in Fig. 3. A similar pattern is exhibited by the amplitude $\tilde{G}$ at any $s_{10} > 0$, with the location of the sign flip forming a straight line of the form $\eta = \kappa s_{10}$ for some positive constant κ. The source of this behavior likely comes from the s_{10}-dependence of the amplitude and does not appear to affect the asymptotic behavior at large η. Hence, understanding this sign reversal is beyond the scope and purpose of this work because, as we will see below, the large-η asymptotics of Q and G_2 at $s_{10} = 0$ is sufficient for us to determine the small-x asymptotics of the helicity PDFs and the g_1 structure function.

Now, along the $s_{10} = 0$ line, Fig. 2 displays the linear increase in the logarithm of the absolute values of the amplitudes once we get sufficiently far away from $\eta = 0$ for the initial conditions and the discretization errors not to be significant any longer. This justifies the following ansätze as large η,

$$Q(s_{10} = 0, \eta) \sim e^{\alpha_Q \eta}, \tag{27a}$$

$$G_2(s_{10} = 0, \eta) \sim e^{\alpha_{G_2} \eta}, \tag{27b}$$

$$\tilde{G}(s_{10} = 0, \eta) \sim e^{\alpha_{\tilde{G}} \eta}. \tag{27c}$$

Here, the parameters α_Q, α_{G_2} and $\alpha_{\tilde{G}}$ (the intercepts) correspond to the slopes of the respective plots in Fig. 2. In particular, the slopes should be extracted from the log-amplitude data where the effects of discretization and initial condition are least significant. In this work, following [1,4,7], we choose to do so in the region where $\eta \in [0.75, 1]\eta_{\max}$.

We extract the intercepts following this recipe for $N_f = 2$, 3, 4 with $\delta = 0.1$ and $\eta_{\max} = 70$. The results are listed in Table I together with their uncertainties, which are calculated from linear regression residual based on the 95% confidence interval, for all the amplitudes and numbers of flavors. For each N_f, the intercepts appear to be the same within the uncertainty for all three polarized dipole amplitudes, Q, G_2 and $\tilde{G}$.

These intercept estimates calculated at $\delta = 0.1$ and $\eta_{\max} = 70$ only provide an initial estimate for the intercepts we would obtain by solving Eq. (13) exactly. However, we will see later that they still differ significantly from the exact values, and the main source of error comes from the fact that we still work with a finite step size δ and a finite maximum rapidity $\eta_{\max}$. To resolve the mismatch, we repeat the computation for other choices of (finite) δ and $\eta_{\max}$. In particular, for each step size δ we numerically compute the intercepts for $\eta_{\max} \in \{10, 20, \ldots, M(\delta)\}$, where $M(\delta)$ is given in Table II.[1]

For each amplitude and at each N_f, we performed a weighted polynomial regression to fit the extracted intercepts as functions of δ and $1/\eta_{\max}$ using the linear, quadratic and cubic models [1]. As a result, the quadratic model performs best based on the Akaike information criterion (AIC) [95] and the significance test on model parameters. Then, we take the model's prediction at $\delta = 1/\eta_{\max} = 0$ to be our estimate for the intercept in the continuum limit. The results are shown in Table III. There, the uncertainty is deduced from the residue of the weighted quadratic regression model. In addition, we include in Fig. 4 the plots showing the intercepts, α_Q, versus δ and $1/\eta_{\max}$, together with the best-fit quadratic surface, for $N_f = 2$, 3, 4 considered here and $N_c = 3$. From Table III, we see that the intercepts for Q, G_2 and $\tilde{G}$ are the same within the uncertainty for each value of N_f. Furthermore, the intercepts decrease as N_f increases. Recall that the large-N_c intercept is 3.66 [1,17], which is greater than the largest intercept in Table III. This is in line with the fact that the large-N_c limit from [1] neglects soft quark emissions and consequently puts $N_f \ll N_c$ or $N_f = 0$ in our terminology. This further reinforces the observation that the intercept decreases with N_f.

Next we study what the large-η asymptotics of the dipole amplitudes imply about the small-x asymptotics of the helicity PDFs and the g_1 structure function. Starting with the gluon helicity PDF, we know that it is related to the

---

[1] We used $\eta_{\max} \in \{10, 21\}$ for $\delta = 0.0375$. Also, for $\delta = 0.05$, we set $M(0.05) = 40$ for $N_f = 4$ and $M(0.05) = 30$ for $N_f = 2$, 3.

TABLE I. Summary of the intercept estimates and uncertainties for all types of polarized dipole amplitudes at $N_f = 2, 3, 4$ along the $s_{10} = 0$ line. Here, the number of quark colors is taken to be $N_c = 3$. The computation is performed with step size, $\delta = 0.1$, maximum rapidity, $\eta_{\max} = 70$, and the all-one initial condition (26).

Number of flavors	α_Q	α_{G_2}	$\alpha_{\tilde{G}}$
$N_f = 2$	3.48990 ± 0.00004	3.48989 ± 0.00005	3.48992 ± 0.00004
$N_f = 3$	3.40163 ± 0.00005	3.40161 ± 0.00005	3.40166 ± 0.00004
$N_f = 4$	3.29297 ± 0.00005	3.29296 ± 0.00005	3.29302 ± 0.00004

TABLE II. The maximum $M(\delta)$ of the $\eta_{\max}$-range computed for each step size δ.

δ	0.016	0.025	0.0375	0.05	0.0625	0.08	0.1
$M(\delta)$	10	20	21	30 or 40	40	50	70

TABLE III. Summary of estimates and uncertainties at the continuum limit ($\delta \to 0$ and $\eta_{\max} \to \infty$) for the intercepts of all types of polarized dipole amplitudes at $N_f = 2, 3, 4$ along the $s_{10} = 0$ line. Here, the number of quark colors is taken to be $N_c = 3$. All the computations are performed with the all-one initial condition (26).

Number of flavors	α_Q	α_{G_2}	$\alpha_{\tilde{G}}$
$N_f = 2$	3.516 ± 0.003	3.516 ± 0.003	3.516 ± 0.003
$N_f = 3$	3.427 ± 0.003	3.426 ± 0.003	3.427 ± 0.003
$N_f = 4$	3.316 ± 0.002	3.316 ± 0.002	3.317 ± 0.002

type-2 polarized dipole amplitude as shown in Eq. (16b), which in the double-logarithmic approximation (DLA) and at $Q^2 = \Lambda^2$ becomes [1]

$$\Delta G(x, Q^2 = \Lambda^2) \approx \frac{2N_c}{\alpha_s \pi^2} G_2\left(s_{10} = 0, \eta = \sqrt{\frac{\alpha_s N_c}{2\pi}} \ln\frac{1}{x}\right). \tag{28}$$

This is because the partial derivative with respect to x_{10}^2 in Eq. (16b) removes a single logarithm, and is, therefore, suppressed in the DLA. As a result, we see that the small-x asymptotics of the gluon helicity PDF is exactly the same as the large-η asymptotics of $G_2(0, \eta)$ with $\eta = \sqrt{\frac{\alpha_s N_c}{2\pi}} \ln\frac{1}{x}$, that is,

$$\Delta G(x, Q^2)|_{Q^2 = \Lambda^2} \sim \left(\frac{1}{x}\right)^{\alpha_{G_2}\sqrt{\frac{\alpha_s N_c}{2\pi}}}. \tag{29}$$

Recall that α_{G_2} depends on N_f.

Next, we consider the flavor-singlet quark helicity PDF and the g_1 structure function. For simplicity, making the approximation that the dipole amplitudes are flavor-independent, we see that the sum over flavors in Eq. (15) becomes a multiplicative factor, leading to the two objects being simply proportional to each other, $g_1 \sim \Delta\Sigma$. Hence, from now on, we proceed with the calculation for the quark helicity PDF.

As a first step, since now Λ is not the IR cutoff, but instead is the scale characterizing the target, we remove $1/\Lambda^2$ from the upper limit of the x_{10}^2-integral in Eq. (16a). (In principle, we should replace it by Λ_{IR}: however, in this work, we simply take Λ_{IR} to be sufficiently large so that the upper limit of $\frac{1}{zQ^2}$ suffices for the transverse integral.) We thus rewrite Eq. (16a) as

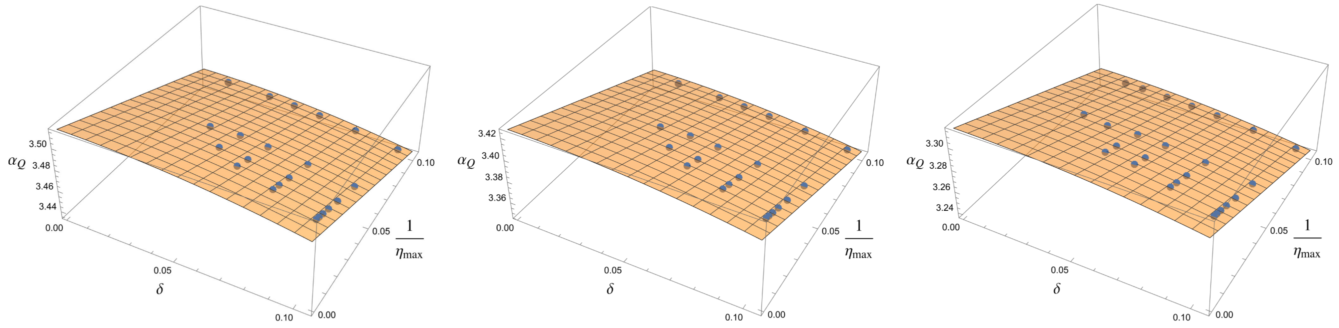

(a) $N_f = 2$ (b) $N_f = 3$ (c) $N_f = 4$

FIG. 4. The plots of estimated intercepts, α_Q, at each N_f, δ and $1/\eta_{\max}$ (blue dots), together with the corresponding best-fitted quadratic extrapolations (yellow surfaces). The continuum limit, $\delta = 1/\eta_{\max} = 0$, corresponds to the lower left corner of each plot.

$$\Delta\Sigma(x,Q^2) = -\frac{N_c N_f}{2\pi^3}\int_{\Lambda^2/s}^{1}\frac{dz}{z}\int_{1/zs}^{1/zQ^2}\frac{dx_{10}^2}{x_{10}^2}\Big[Q(x_{10}^2,zs)+2G_2(x_{10}^2,zs)\Big]. \tag{30}$$

Here, the center-of-mass energy of the interaction is high, such that $x \simeq \frac{Q^2}{s}$ in the small-x regime. Now, in terms of s_{10} and η, the flavor-singlet quark helicity PDF from Eq. (30) can be written as [4]

$$\Delta\Sigma(x,Q^2=\Lambda^2) = -\frac{N_c N_f}{2\pi^3}\int\limits_{0}^{\sqrt{\frac{\alpha_s N_c}{2\pi}}\ln\frac{1}{x}} d\eta \int\limits_{\eta-\sqrt{\frac{\alpha_s N_c}{2\pi}}\ln\frac{1}{x}}^{\eta} ds_{10}\Big[Q(s_{10},\eta)+2G_2(s_{10},\eta)\Big]. \tag{31}$$

In Eq. (31), the quantity, $\sqrt{\frac{\alpha_s N_c}{2\pi}}\ln\frac{1}{x} \equiv \eta_b$, is large when x is small. Here, η_b can be viewed as the maximum rapidity limiting the integration region.

The integral in Eq. (31) can be evaluated as a Riemann sum using our numerical results for the fundamental dipole amplitudes,

$$\Delta\Sigma_j \equiv \Delta\Sigma\left(x=\exp\left[-\sqrt{\frac{2\pi}{\alpha_s N_c}}j\delta\right], Q^2\sim\Lambda^2\right) = -\frac{N_c N_f}{2\pi^3}\delta^2\sum_{j'=0}^{j-1}\sum_{i'=j'-j}^{j'-1}\left[Q_{i'j'}+2G_{2,i'j'}\right], \tag{32}$$

which can be written recursively as

$$\Delta\Sigma_j = \Delta\Sigma_{j-1} - \frac{N_c N_f}{2\pi^3}\delta^2\sum_{j'=0}^{j-2}\Big[Q_{(j'-j)j'}+2G_{2,(j'-j)j'}\Big] - \frac{N_c N_f}{2\pi^3}\delta^2\sum_{i'=-1}^{j-2}\Big[Q_{i'(j-1)}+2G_{2,i'(j-1)}\Big], \tag{33}$$

for $j \geq 1$. Note that $\Delta\Sigma_0 = 0$ in this notation. Physically, since $j=0$ corresponds to $x=1$, the value of $\Delta\Sigma_0$ simply implies that the quark helicity PDF at moderate x is much smaller than its values at small x, as the latter is driven by the polarized dipole amplitudes that grow exponentially in magnitude with $\ln(1/x)$. In a phenomenological calculation, c.f. [4,7,15], one may need to begin this iterative calculation at some $j = j_0 > 0$, corresponding to a value of Bjorken-x that is small enough for our evolution to apply but large enough to have good experimental constraints. Then, the value of $\Delta\Sigma_{j_0}$ should also be deduced from experimental results. However, proper matching of small-x evolution onto the large-x physics is an open problem we are not going to address here.

For the purpose of this work, we perform the numerical integration starting from $j_0 = 0$ employing the dipole amplitudes we numerically obtained previously using $N_c = 3$, $\delta = 0.1$ and $\eta_{\max} = 70$. For each of $N_f = 2$, 3, 4, we obtain the values of quark helicity PDF at the values of Bjorken x such that $\eta_b = \sqrt{\frac{\alpha_s N_c}{2\pi}}\ln\frac{1}{x} = 70, 69.9, 69.8, \ldots$. Here, we take the strong coupling constant to be $\alpha_s \simeq 0.35$ [4]. The result for $N_f = 4$ is given by the plot in Fig. 5. There, the vertical axis of the plot is the sign of the flavor-singlet quark helicity PDF, multiplied by the logarithm of its magnitude. The horizontal axis depicts $\ln x$. The clear linear trend implies that the magnitude of quark helicity PDF grows exponentially with $\ln(1/x)$, which is qualitatively the same as the large-η asymptotics of polarized dipole amplitudes at $s_{10} = 0$. Explicitly, we have

$$\Delta\Sigma(x,Q^2)|_{Q^2=\Lambda^2} \sim g_1(x,Q^2)|_{Q^2=\Lambda^2} \sim \left(\frac{1}{x}\right)^{\alpha_h^{(N_f)}}, \tag{34}$$

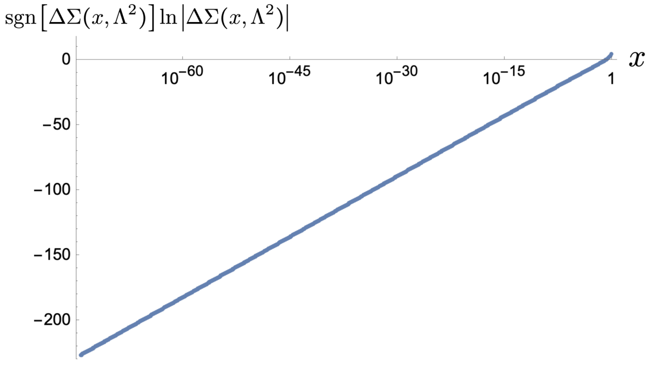

FIG. 5. The plot of $\mathrm{sgn}[\Delta\Sigma(x,Q^2)]\ln|\Delta\Sigma(x,Q^2)|$, numerically computed at $Q^2=\Lambda^2$ using Eq. (33), as a function of Bjorken x. In the calculation, we used the step size of $\delta = 0.1$ and maximum rapidity of $\eta_{\max} = 70$. Other parameters are $N_c = 3$, $N_f = 4$ and $\alpha_s = 0.35$.

where the intercept, $\alpha_h^{(N_f)}$, generally depends on the number of quark flavors, N_f. Next, we perform a linear regression on the data points for $\Delta\Sigma_j$ from Fig. 5 with $0.75 j_{\max} \leq j \leq j_{\max}$. As a result, the intercept for $N_f = 4$, extracted at $\delta = 0.1$ and $\eta_{\max} = 70$, is equal to

$$\alpha_h^{(4)}\Big|_{\delta=0.1,\eta_{\max}=70} = (3.29294 \pm 0.00005)\sqrt{\frac{\alpha_s N_c}{2\pi}}. \quad (35)$$

This value of intercept is within the uncertainties of the intercepts for the large-η asymptotics of the polarized dipole amplitudes, Q, G_2 and $\tilde{G}$, given in Table I for the same $N_f = 4$. This result allows us to assume that a similar agreement would be obtained between the intercepts for $\Delta\Sigma$ and the polarized dipole amplitudes for other values of δ and η_b (or $\eta_{\max}$). We, therefore, deduce the continuum-limit intercept ($\delta \to 0$ and $\eta_{\max} \to \infty$) for $\Delta\Sigma$ by reading off the corresponding continuum-limit results from the bottom row of Table III. Approximately, this gives

$$\alpha_h^{(4)} = 3.32\sqrt{\frac{\alpha_s N_c}{2\pi}}. \quad (36)$$

We repeat the above steps for $N_f = 2$ and $N_f = 3$, using again the amplitudes we computed at $\delta = 0.1$ and $\eta_{\max} = 70$. This results in the following intercepts for the discretized $\Delta\Sigma$,

$$\alpha_h^{(2)}\Big|_{\delta=0.1,\eta_{\max}=70} = (3.48988 \pm 0.00005)\sqrt{\frac{\alpha_s N_c}{2\pi}}, \quad (37a)$$

$$\alpha_h^{(3)}\Big|_{\delta=0.1,\eta_{\max}=70} = (3.40160 \pm 0.00005)\sqrt{\frac{\alpha_s N_c}{2\pi}}. \quad (37b)$$

For each N_f, the intercept of the small-x asymptotics for the flavor-singlet quark helicity PDF is within the uncertainty from the intercepts of the respective large-η asymptotics of the polarized dipole amplitudes we obtained in Table I. This allows us to read off the corresponding continuum-limit results from Table III, which gives

$$\alpha_h^{(2)} = 3.52\sqrt{\frac{\alpha_s N_c}{2\pi}}, \quad (38a)$$

$$\alpha_h^{(3)} = 3.43\sqrt{\frac{\alpha_s N_c}{2\pi}}. \quad (38b)$$

Equations (36) and (38) giving us the intercepts of the g_1 structure function and the quark helicity PDFs are the main results of this subsection. Note that the same intercepts drive the asymptotics of the gluon helicity PDFs, per Eq. (29).

Let us cross check these intercepts against the results obtained using the IREE formalism of BER [34]. We calculated the BER intercepts numerically using the formalism from [34] while applying the large-$N_c\,\&\,N_f$ limit to them. The results are given in Table IV for $N_f = 2$, 3, 4 we considered in this section. The KPS-CTT intercepts we found above are also listed for comparison.

TABLE IV. The intercepts at large $N_c\,\&\,N_f$ for $N_f = 2$, 3, 4 and $N_c = 3$ (that is, for $N_f/N_c = 2/3, 3/3, 4/3$) according to the BER and KPS-CTT evolutions.

N_f	BER intercept	KPS-CTT intercept
2	3.55	3.52
3	3.48	3.43
4	3.41	3.32

Table IV shows that the intercepts of the KPS-CTT evolution calculated at large-$N_c\,\&\,N_f$ differ from the corresponding intercepts of the BER evolution [34]. The discrepancy is at the 2–3% level and increases with N_f. This is a significant improvement relative to the large mismatches found in [4] using the KPS evolution [2,3] that did not include the type-2 polarized dipole amplitude. Furthermore, as shown in [17], the analytic expression for the large-N_c intercept of the KPS-CTT small-x helicity evolution is also different from that of BER, although the difference in that case is only at the 0.1% level. The root cause behind these remaining discrepancies deserves a further study, which is left for a future work.

C. Solution for $N_f = 6$

Now, we consider the $N_f = 6$ case. Again, we begin with the step size $\delta = 0.1$ and maximum rapidity $\eta_{\max} = 70$. This gives us the polarized dipole amplitudes plotted in Fig. 6. There, each plot shows the logarithm of the absolute value of the labeled amplitude. The plots demonstrate an approximately linear rise of $\ln|Q(s_{10},\eta)|$, $\ln|G_2(s_{10},\eta)|$ and $\ln|\tilde{G}(s_{10},\eta)|$ with η, similar to the lower-N_f case presented in Sec. III B. The only difference is that the rise is no longer monotonic and appears to be periodically interrupted by lines of sharp local minima.

To illustrate the origin of this nonmonotonicity, we plot $\mathrm{sgn}[Q(0,\eta)]\ln|Q(0,\eta)|$, $\mathrm{sgn}[G_2(0,\eta)]\ln|G_2(0,\eta)|$ and $\mathrm{sgn}[\tilde{G}(0,\eta)]\ln|\tilde{G}(0,\eta)|$ as functions of η in Fig. 7. From these plots we see that $Q(0,\eta)$, $G_2(0,\eta)$, and $\tilde{G}(0,\eta)$ oscillate with η: the oscillations explain the nonmonotonic behavior we saw in Fig. 6. This emergence of the oscillatory behavior in the amplitude marks the main qualitative difference between the case of $N_f = 6$ and those with fewer quark flavors, for the calculation of small-x asymptotics for the quark helicity distribution at large $N_c\,\&\,N_f$. (More precisely, we see that in the large-$N_c\,\&\,N_f$ limit, the oscillations are absent for $N_f/N_c < 2$ and set in at $N_f/N_c = 2$.) In contrast, a similar study [4] performed at large $N_c\,\&\,N_f$ for the

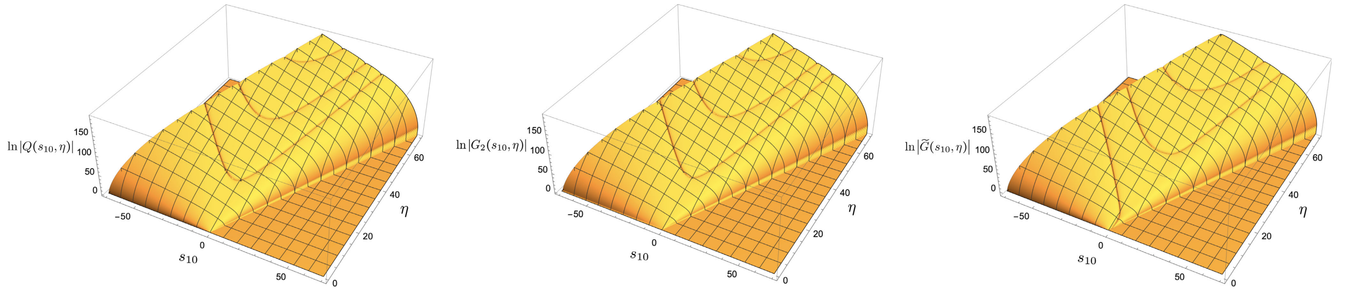

(a) $\ln|Q(s_{10},\eta)|$ (b) $\ln|G_2(s_{10},\eta)|$ (c) $\ln\left|\widetilde{G}(s_{10},\eta)\right|$

FIG. 6. The plots of logarithms of the absolute values of polarized dipole amplitudes Q, G_2 and $\tilde{G}$ at $N_f = 6$, $N_c = 3$ versus s_{10} and η, in the $-\eta_{\max} \le s_{10} \le \eta_{\max}$, $0 \le \eta \le \eta_{\max}$ region with $\eta_{\max} = 70$. The amplitudes were computed numerically using the step size $\delta = 0.1$.

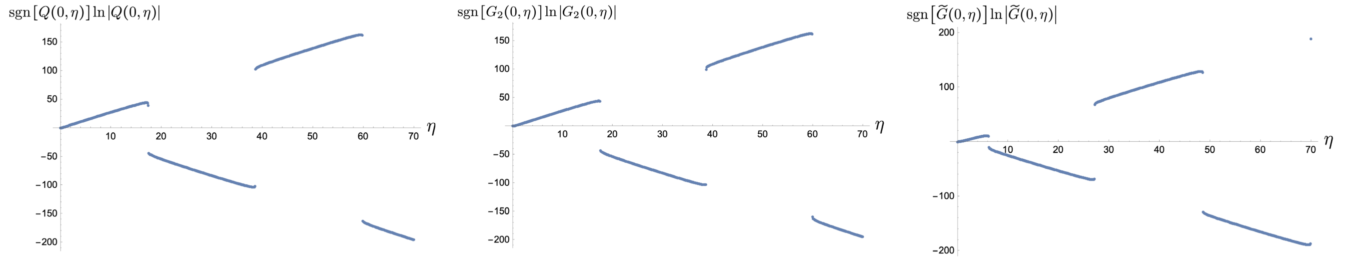

(a) $\mathrm{sgn}[Q(0,\eta)]\ln|Q(0,\eta)|$ (b) $\mathrm{sgn}[G_2(0,\eta)]\ln|G_2(0,\eta)|$ (c) $\mathrm{sgn}\left[\widetilde{G}(0,\eta)\right]\ln\left|\widetilde{G}(0,\eta)\right|$

FIG. 7. The plots of the logarithms of the absolute values of polarized dipole amplitudes Q, G_2 and $\tilde{G}$, multiplied by the signs of the amplitudes, versus the rapidity η along the $s_{10} = 0$ line. The amplitudes are computed numerically in the range $0 \le \eta \le \eta_{\max} = 70$ using step size $\delta = 0.1$ at $N_f = 6$, $N_c = 3$.

evolution equations without the type-2 polarized dipole amplitude saw the oscillatory behavior for any N_f between 2 and 6.

While an analytic solution of Eq. (13) is beyond the scope of this work, we can attempt to find analytic formulas approximating our numerical results, at least in the large-η asymptotics. Combining the oscillations with the exponential growth of the maxima of $|Q(0,\eta)|$, $|G_2(0,\eta)|$ and $|\tilde{G}(0,\eta)|$ with η, we propose the following large-η asymptotic forms for the polarized dipole amplitudes [4]:

$$Q(0,\eta) \sim e^{\alpha_Q \eta} \cos(\omega_Q \eta + \varphi_Q), \tag{39a}$$

$$G_2(0,\eta) \sim e^{\alpha_{G_2} \eta} \cos(\omega_{G_2} \eta + \varphi_{G_2}), \tag{39b}$$

$$\tilde{G}(0,\eta) \sim e^{\alpha_{\tilde{G}} \eta} \cos(\omega_{\tilde{G}} \eta + \varphi_{\tilde{G}}). \tag{39c}$$

For the respective dipole amplitudes, the oscillation frequencies are denoted by ω_Q, ω_{G_2} and $\omega_{\tilde{G}}$, while the initial phases are denoted by φ_Q, φ_{G_2} and $\varphi_{\tilde{G}}$. Furthermore, the amplitudes of oscillations in $Q(0,\eta)$, $G_2(0,\eta)$ and $\tilde{G}(0,\eta)$ grow exponentially with η, with the exponents α_Q, α_{G_2}, and $\alpha_{\tilde{G}}$, respectively.

To extract the parameters from Eq. (39), consider a general function of the form

$$f(\eta) = K e^{\alpha\eta} \cos(\omega\eta + \varphi) \tag{40}$$

with some parameters α, ω, φ, and K. This is the asymptotic form proposed at large η in Eq. (39) for the polarized dipole amplitudes. We see that

$$\frac{d^2}{d\eta^2} \ln|f(\eta)| = \frac{d}{d\eta}[\alpha - \omega \tan(\omega\eta + \varphi)] = -\frac{\omega^2}{\cos^2(\omega\eta + \varphi)}. \tag{41}$$

Then, this second derivative contains local maxima where $\cos(\omega\eta + \varphi) = \pm 1$. As a result, in the context of a numerical calculation, the frequency, ω, can be found from the value of the numerically obtained second derivative at the maximum,

$$\max\left[\frac{d^2}{d\eta^2} \ln|f(\eta)|\right] = -\omega^2. \tag{42}$$

Here, we adopt a convention in which $\omega > 0$ when deducing ω from a local maximum in Eq. (42). In particular, we use the largest-η maximum available in our numerical results to extract ω, in order to get as close as possible to the large-η regime. The extracted value of ω can be cross-checked by comparing π/ω to the spacing between the positions of the local maxima along the η-axis in the numerical solution.

The phase, φ, can then be determined from the second derivative maximum condition $\omega\eta^* + \varphi = \pi n$, where η^* is the numerically-extracted position of the largest-η local maximum from Eq. (42). Here, n is an integer whose value is adjusted so that $\varphi \in (-\pi, \pi]$. In particular, the choice between $\varphi \in (0, \pi]$ and $\varphi \in (-\pi, 0]$ is made by making sure that the sign of $f(\eta^*)$ we calculated numerically matches that of $\cos(\omega\eta^* + \varphi)$.

Finally, we notice that

$$\ln\left|\frac{f(\eta)}{\cos(\omega\eta + \varphi)}\right| = \alpha\eta + \ln K. \tag{43}$$

This allows us to obtain an estimate for the parameter α by performing a linear regression on $\ln|f(\eta)/\cos(\omega\eta + \varphi)|$ as a function of η to determine the slope. Here, it is appropriate to use the parameter estimates of ω and φ that we obtained from the previous step. The uncertainties from the estimates of ω and φ are also propagated to each data point, leading to the weights for the linear regression mentioned above. Given $\eta_{\max}$, once we determine the numerical values of the amplitudes found in the range $\eta \in [0, \eta_{\max}]$, there is always the largest local maximum, η^*, which leads to the definition, $d = \min\{\eta_{\max} - \eta^*, \frac{\pi}{10\omega}\}$. Then, we extract α from the range $\eta \in [\eta^* - d, \eta^* + d]$ and associate α, together with ω and φ we found earlier, with $\eta^* + d$ (instead of $\eta_{\max}$). This eliminates the bias in α that may arise from extracting the slope at different phases in the oscillation, while still allowing us to perform the extraction in the large-η region where the asymptotic behavior dominates. Furthermore, one avoids extracting the slope near the zeros of the cosine function, where Eq. (43) becomes less accurate due to the divergence.

To estimate the uncertainties for these parameters, we first notice that the intercept receives uncertainty from residuals of the linear regression fit to the function in Eq. (43). This provides the uncertainty estimate for α. As for ω and φ, their uncertainty estimates require a more careful consideration.

The oscillation frequency ω receives an uncertainty from the fact that it is estimated by the quantity in Eq. (42), whose values come in discrete steps. To estimate its uncertainty, consider the case where the true local maximum, η_{true}, is off from the estimated location, η^*, by a distance, $\Delta\eta$. We also approximate the function in Eq. (41) to be quadratic around the local maximum, taking the form of $-a(\eta - \eta_{\text{true}})^2 - \omega_{\text{true}}^2$ for some constant $a > 0$. In this notation, we would make the exactly correct frequency estimate, $\hat{\omega} = \omega_{\text{true}}$, when $\eta^* = \eta_{\text{true}}$. Otherwise, the estimated frequency would be

$$\hat{\omega} = \omega_{\text{true}} + \Delta\omega = \sqrt{a(\eta^* - \eta_{\text{true}})^2 + \omega_{\text{true}}^2}. \tag{44}$$

If we assume that $\Delta\omega$ is small relative to ω_{true}, then Eq. (44) yields

$$\Delta\omega \approx \frac{a}{2\omega_{\text{true}}}(\eta^* - \eta_{\text{true}})^2. \tag{45}$$

Equation (45) would lead to the uncertainty, $\Delta\omega$, if we knew the values of a and ω_{true}. To determine these parameters, we first assume that $\eta^* < \eta_{\text{true}}$ without loss of generality. Then, consider the values, $-\omega_1^2$ and $-\omega_2^2$, of $\frac{d^2}{d\eta^2}\ln|f(\eta)|$ at $\eta^* + \delta$ and $\eta^* - \delta$, respectively. Both ω_1 and ω_2 are calculable from the numerical results. Then, through a calculation similar to Eq. (44), it follows that

$$a = \frac{1}{2\delta^2}[(\omega_1^2 - \hat{\omega}^2) + (\omega_2^2 - \hat{\omega}^2)]. \tag{46}$$

Plugging Eq. (46) into Eq. (45) and approximating ω_{true} by $\hat{\omega}$, we obtain

$$\Delta\omega = \frac{1}{4\hat{\omega}\delta^2}(\eta^* - \eta_{\text{true}})^2[(\omega_1^2 - \hat{\omega}^2) + (\omega_2^2 - \hat{\omega}^2)]. \tag{47}$$

Finally, we assume a uniform distribution from $-\frac{\delta}{2}$ to $\frac{\delta}{2}$ for $\eta^* - \eta_{\text{true}}$, which is reasonable given that the true local maximum is equally likely to fall anywhere within the grid. Then, with probability P, we have that $\eta^* - \eta_{\text{true}}$ falls within $(\Delta\eta)_P = \frac{P\delta}{2}$ from zero. As a result, with the same probability, $\Delta\omega$ falls within

$$(\Delta\omega)_P = \frac{P^2}{16\hat{\omega}}[(\omega_1^2 - \hat{\omega}^2) + (\omega_2^2 - \hat{\omega}^2)]. \tag{48}$$

Then, we take this range with $P = 0.95$ to be the uncertainty for our frequency estimate, $\hat{\omega}$. This corresponds to the 95% confidence interval.

Finally, for the initial phase, the method discussed above implies that its uncertainty is equal to that of the product, $\omega_{\text{true}}\eta_{\text{true}}$, which is approximated by $\hat{\omega}\eta^*$ in the notations we used previously. Then, the uncertainty is simply

$$(\Delta\varphi)_P = \hat{\omega}(\Delta\eta)_P + \eta^*(\Delta\omega)_P, \tag{49}$$

where $(\Delta\eta)_P$ and $(\Delta\omega)_P$ can be read off from above. Again, we use $P = 0.95$ to estimate the uncertainty of our best-fitted initial phase, in order to be consistently using 95% confidence interval.

As a first cross check, we plot in Fig. 8 the functions inspired by Eqs. (39)–(41) applied to the polarized dipole amplitudes, namely $\frac{d^2}{d\eta^2}\ln|Q(0,\eta)|$, $\frac{d^2}{d\eta^2}\ln|G_2(0,\eta)|$ and $\frac{d^2}{d\eta^2}\ln|\tilde{G}(0,\eta)|$ for $N_f = 6$ as functions of η. For η above 10, the shape of each graph qualitatively looks like that of the function $\frac{d^2}{d\eta^2}\ln|f(\eta)|$ in Eq. (41), displaying periodic local maxima below the η-axis. This provides another

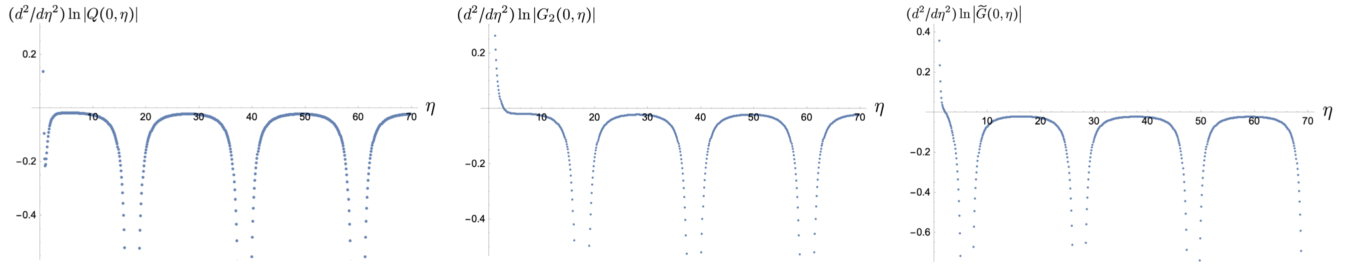

(a) $\frac{d^2}{d\eta^2}\ln|Q(0,\eta)|$ (b) $\frac{d^2}{d\eta^2}\ln|G_2(0,\eta)|$ (c) $\frac{d^2}{d\eta^2}\ln|\widetilde{G}(0,\eta)|$

FIG. 8. Plots of $\frac{d^2}{d\eta^2}\ln|Q(0,\eta)|$, $\frac{d^2}{d\eta^2}\ln|G_2(0,\eta)|$, and $\frac{d^2}{d\eta^2}\ln|\tilde{G}(0,\eta)|$ versus η for $N_f = 6$ and $N_c = 3$. All graphs result from our numerical computation with step size $\delta = 0.1$ and $\eta_{\max} = 70$.

justification for the proposed asymptotic forms (39), which resemble the definition of $f(\eta)$ given in Eq. (40).

Next, we fit our numerical results at $N_f = 6$ with $\delta = 0.1$ and $\eta_{\max} = 70$, following the method outlined above. This leads to the parameter estimates and uncertainties listed in Table V. There, the intercepts seem to be within the uncertainties from one another. In addition, the significant discrepancy in the frequency estimates could be a result of the discretization error that will be addressed shortly. However, the clear discrepancy is in the initial phase for $\tilde{G}$ compared to those of Q and G_2, which is unlikely to be caused by the discretization error alone. This is entirely possible given that $\tilde{G}$ is defined based on an adjoint polarized dipole while Q and G_2 are defined based on the fundamental counterparts. As far as the application of the results is concerned, the initial phase is a parameter that depends not only on the choice of initial condition but also on the value of Bjorken x at which the small-x evolution begins to dominate. In an actual phenomenological fit, one would be able to determine the proper initial phases by the moderate-x data.

Before we address the potential discretization error, we consider as final cross checks for the asymptotic forms (39) the functions, $e^{-\alpha_Q\eta}Q(0,\eta)$, $e^{-\alpha_{G_2}\eta}G_2(0,\eta)$ and $e^{-\alpha_{\tilde{G}}\eta}\tilde{G}(0,\eta)$. In Fig. 9, these functions are plotted against η. We see that the functions display a clear sinusoidal pattern for $\eta \gtrsim 30$, demonstrating oscillatory behavior in the large-η asymptotics, as expected from our ansätze (39). Furthermore, we plot $\ln|\frac{Q(0,\eta)}{\cos(\omega_Q\eta+\varphi_Q)}|$, $\ln|\frac{G_2(0,\eta)}{\cos(\omega_{G_2}\eta+\varphi_{G_2})}|$ and $\ln|\frac{\tilde{G}(0,\eta)}{\cos(\omega_{\tilde{G}}\eta+\varphi_{\tilde{G}})}|$ versus η in Fig. 10. From this second set of plots, we see that the logarithms grow roughly linearly with η, except for minor periodic bumps that occur near the sinusoidal nodes. This implies that the amplitudes divided by the corresponding cosine functions grow exponentially with η. Again, this is consistent with the asymptotic forms (39) proposed earlier.

To address potential biases coming from discretization, we repeat the calculation for different values of step size, δ, and maximum rapidity, $\eta_{\max}$. In particular, we use $\delta = 0.0375$, 0.05, 0.0625, 0.08, 0.1, 0.16, 0.2, 0.25, 0.5. For each δ, we obtain the parameter estimates using the method outlined above at each of the oscillation antinodes below $M(\delta)$, which is listed for each δ in Table VI. Note that the parameter estimation method also implies the corresponding $\eta^* + d$ to be associated with the estimated α, ω and φ. We then perform a weighted polynomial regression against δ and $\eta^* + d$ for each fitted parameter, similar to what we did in Section III B. For all the parameters and the amplitudes, the quadratic model performs the best, resulting in the continuum-limit estimates, which is the model's prediction at $\delta = 1/\eta_{\max} = 0$, shown in Table VII.

From Table VII, we see that the intercepts, α, are the same within the uncertainty for all the amplitudes, while the frequencies, ω, exhibit statistically significant but very small differences. As for the initial phase, φ, it is the same within the uncertainty for Q and G_2, but it is significantly different for $\tilde{G}$. Furthermore, the intercepts

TABLE V. Summary of the parameter estimates and uncertainties for all types of polarized dipole amplitudes along the $s_{10} = 0$ line. Here, the number of quark flavors and colors are taken to be $N_f = 6$ and $N_c = 3$, respectively. The computation is performed with step size $\delta = 0.1$, maximum rapidity $\eta_{\max} = 70$, and the all-one initial condition (26).

Dipole amplitudes	Intercept (α)	Frequency (ω)	Initial phase (φ)
$Q(0,\eta)$	2.801 ± 0.007	0.146803 ± 0.000004	-0.940 ± 0.007
$G_2(0,\eta)$	2.802 ± 0.007	0.146821 ± 0.000004	-0.955 ± 0.007
$\tilde{G}(0,\eta)$	2.802 ± 0.006	0.146294 ± 0.000004	0.764 ± 0.007

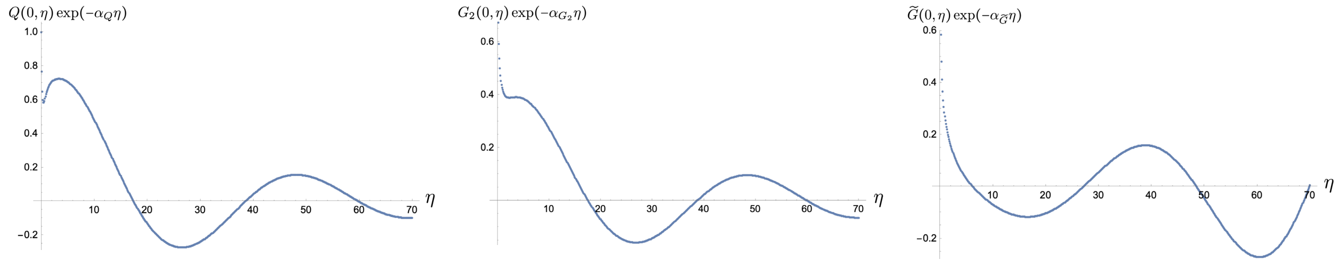

(a) $e^{-\alpha_Q\eta}Q(0,\eta)$ (b) $e^{-\alpha_{G_2}\eta}G_2(0,\eta)$ (c) $e^{-\alpha_{\widetilde{G}}\eta}\widetilde{G}(0,\eta)$

FIG. 9. Plots of $e^{-\alpha_Q\eta}Q(0,\eta)$, $e^{-\alpha_{G_2}\eta}G_2(0,\eta)$ and $e^{-\alpha_{\tilde{G}}\eta}\tilde{G}(0,\eta)$ versus η at $N_f = 6$ and $N_c = 3$. All the graphs are numerically computed with step size $\delta = 0.1$ and $\eta_{\max} = 70$.

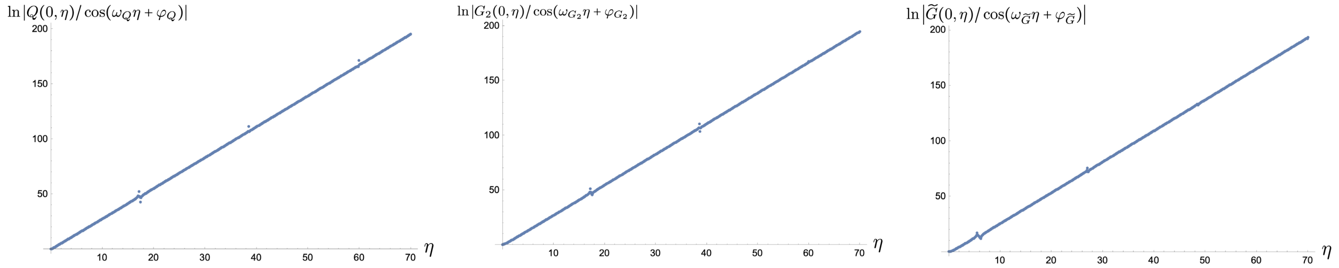

(a) $\ln\left|\frac{Q(0,\eta)}{\cos(\omega_Q\eta+\varphi_Q)}\right|$ (b) $\ln\left|\frac{G_2(0,\eta)}{\cos(\omega_{G_2}\eta+\varphi_{G_2})}\right|$ (c) $\ln\left|\frac{\widetilde{G}(0,\eta)}{\cos(\omega_{\widetilde{G}}\eta+\varphi_{\widetilde{G}})}\right|$

FIG. 10. Plots of $\ln|\frac{Q(0,\eta)}{\cos(\omega_Q\eta+\varphi_Q)}|$, $\ln|\frac{G_2(0,\eta)}{\cos(\omega_{G_2}\eta+\varphi_{G_2})}|$ and $\ln|\frac{\tilde{G}(0,\eta)}{\cos(\omega_{\tilde{G}}\eta+\varphi_{\tilde{G}})}|$ versus η at $N_f = 6$ and $N_c = 3$. All the graphs are numerically computed with step size $\delta = 0.1$ and $\eta_{\max} = 70$.

are below those for $N_f = 4$, continuing the trend we observed earlier that the intercept decreases as we add more quark flavors.

With the qualitatively different results between $N_f \leq 5$ and $N_f = 6$, we examine the possibility that the amplitudes also oscillate at $N_f \leq 5$ but with much longer periods than $\eta_{\max} = 70$, which is the largest rapidity value we used in our calculations to this point for $N_f = 2, 3, 4$. In particular, we repeat the computation at $N_f = 4$ with $\delta = 0.5$ and $\eta_{\max} = 225$. As shown in Fig. 11 up to the rapidity of $\eta = 225$, the logarithms of the absolute values of the dipole amplitudes at $N_f = 4$ still grow linearly with η, displaying no sign of oscillation or other nonexponential behavior. The mathematical reason behind a radical change in the asymptotic behavior of the amplitudes as N_f reaches the value of $2N_c = 6$ remains unclear. It is likely that an analytic solution is necessary to offer a clear explanation of the transition. This is beyond the scope of this paper.

TABLE VI. The maximum, $M(\delta)$, of $\eta_{\max}$ computed for each step size δ in the case where $N_f = 6$, $N_c = 3$.

δ	0.0375	0.05	0.0625	0.08	0.1	0.16	0.2	0.25	0.5
$M(\delta)$	30	40	40	50	70	100	120	150	200

Now that the large-η asymptotics have been established for the polarized dipole amplitudes, we are able to deduce the small-x asymptotics for the gluon helicity PDF, $\Delta G(x, Q^2)$, by reading off the parameter estimates for $G_2(0,\eta)$ from Table VII. In particular, we have

TABLE VII. Summary of the parameter estimates and uncertainties at the continuum limit ($\delta \to 0$ and $\eta_{\max} \to \infty$) for all types of polarized dipole amplitudes along the $s_{10} = 0$ line. Here, the number of quark flavors and colors are taken to be $N_f = 6$ and $N_c = 3$, respectively. The computation is performed with the all-one initial condition (26).

Dipole amplitudes	Intercept (α)	Frequency (ω)	Initial phase (φ)
$Q(0,\eta)$	2.82 ± 0.04	0.15074 ± 0.00008	-0.94 ± 0.10
$G_2(0,\eta)$	2.83 ± 0.04	0.15041 ± 0.00008	-0.90 ± 0.10
$\tilde{G}(0,\eta)$	2.82 ± 0.04	0.14807 ± 0.00005	0.74 ± 0.07

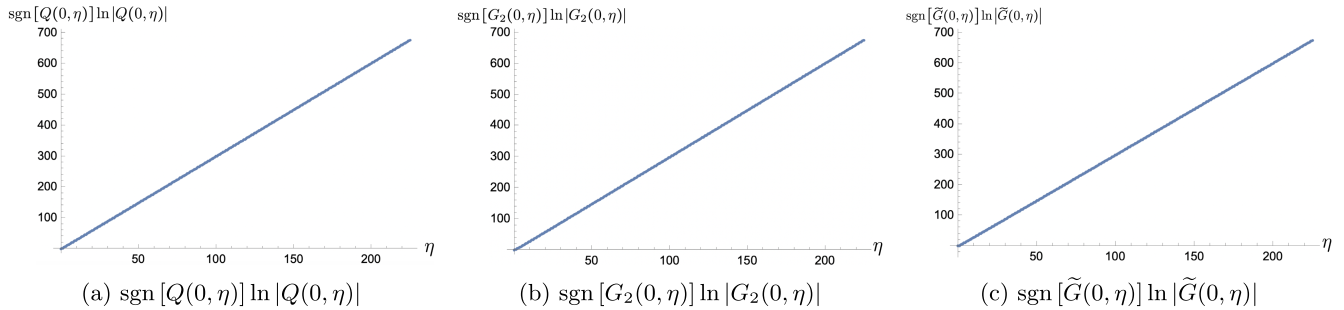

(a) sgn $[Q(0,\eta)]\ln|Q(0,\eta)|$ (b) sgn $[G_2(0,\eta)]\ln|G_2(0,\eta)|$ (c) sgn $[\widetilde{G}(0,\eta)]\ln|\widetilde{G}(0,\eta)|$

FIG. 11. The plots of logarithms of the absolute values of polarized dipole amplitudes Q, G_2, and $\tilde{G}$, multiplied by their signs, along $s_{10} = 0$ line, versus the rapidity, η. The amplitudes are computed numerically in the range $0 \le \eta \le \eta_{\max} = 225$ using step size $\delta = 0.5$ at $N_f = 4$, $N_c = 3$.

$$\Delta G(x,Q^2)|_{Q^2=\Lambda^2} \sim \left(\frac{1}{x}\right)^{(2.83\pm0.04)\sqrt{\frac{\alpha_s N_c}{2\pi}}} \cos\left[(0.15041\pm0.00008)\sqrt{\frac{\alpha_s N_c}{2\pi}}\ln\frac{1}{x} - (0.90\pm0.10)\right]. \tag{50}$$

As for the quark helicity PDF, which we have argued in Section III B to have the same small-x asymptotics as the g_1 structure function, we repeat the numerical calculation for $\Delta\Sigma(x,Q^2)|_{Q^2=\Lambda^2}$ at $N_f = 6$ using the recursive discretized formula (33) with $\Delta\Sigma_0 = 0$ (see Eq. (32) for the definition of $\Delta\Sigma_j$). Here, we begin with step size $\delta = 0.1$ and $\eta_{\max} = 70$. This results in the quark helicity PDF plotted in Fig. 12, which displays similar oscillations together with the exponential growth in $\ln(1/x)$ as we saw previously for the polarized dipole amplitudes as a function of η. We apply the process described earlier in this section to the quark helicity PDF obtaining

$$\begin{aligned}\Delta\Sigma(x,Q^2)|_{Q^2=\Lambda^2} &\sim g_1(x,Q^2)|_{Q^2=\Lambda^2}\\ &\sim \left(\frac{1}{x}\right)^{(2.801\pm0.007)\sqrt{\frac{\alpha_s N_c}{2\pi}}} \cos\left[(0.14689\pm0.00002)\sqrt{\frac{\alpha_s N_c}{2\pi}}\ln\frac{1}{x} + (2.080\pm0.008)\right].\end{aligned} \tag{51}$$

Comparing these parameters to the results in Table V for $\delta = 0.1$ and $\eta_{\max} = 70$, we see that the intercept and oscillation frequency for the quark helicity PDF are similar to those for the polarized fundamental dipole amplitudes, Q and G_2. This allows us to use the continuum-limit estimates for the intercept and the frequency,

$$\alpha_h^{(6)} = 2.83\sqrt{\frac{\alpha_s N_c}{2\pi}}, \tag{52a}$$

$$\omega_h^{(6)} = 0.150\sqrt{\frac{\alpha_s N_c}{2\pi}}, \tag{52b}$$

respectively, to obtain the small-x asymptotics of the quark helicity PDF. As for the initial phase, besides the expected offset by π due to the overall sign flip, which in turn follows from the leading negative sign in Eq. (30), the initial phase estimate for the quark helicity PDF is slightly off from those for both Q and G_2. This makes it inaccurate to directly deduce the initial phase for quark helicity PDF asymptotics without performing the actual calculation. However, as discussed in [4], the initial phase has a strong dependence on the value of x where our small-x evolution begins to dominate, which makes it less important for studies of low-x asymptotics.

Another observation we can make using Fig. 12 is that the oscillation period is large in term of x. Depending on the initial condition and/or the value of x where the evolution begins to dominate, one should be able to observe at most one sign flip in the quark helicity PDF or the g_1 structure function in the kinematics of the future Electron-Ion Collider (EIC) [19,23,24,26]. In fact, Eq. (50) implies the same conclusion for the gluon helicity PDF at $N_f = 6$ as well. With the range of measurements at the EIC, which will not be lower than $x \sim 10^{-4}$ [19,26], we will not be able to observe a full oscillation period in a foreseeable future. (And we have not even mentioned the fact that to reach $N_f = 6$ in helicity measurements one would need to perform double spin asymmetry measurements at unprecedentedly high values of the photon virtuality Q^2.) Furthermore, as x decreases, single-logarithmic effects start to significantly mix in, coming both from the helicity evolution[2] and from the unpolarized BK/JIMWLK

---

[2] See [16] for a partial derivation of the small-x helicity evolution at singlet-logarithmic order, without the type-2 polarized dipole amplitude.

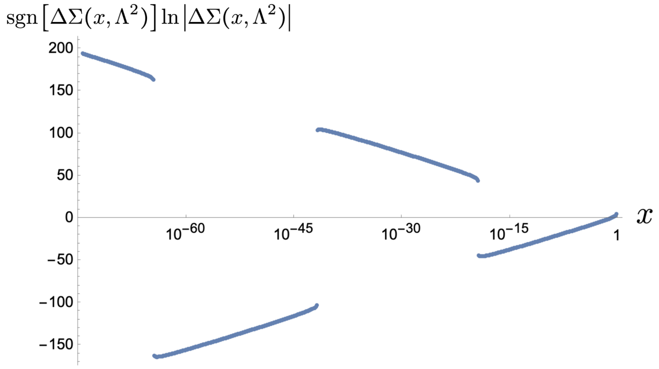

FIG. 12. The plot of $\mathrm{sgn}[\Delta\Sigma(x,Q^2)]\ln|\Delta\Sigma(x,Q^2)|$, numerically computed at $Q^2=\Lambda^2$ using Eq. (33), as a function of Bjorken x. In the calculation, we used the step size of $\delta=0.1$ and maximum rapidity of $\eta_{\max}=70$. Other constants are set such that $N_c=3$, $N_f=6$ and $\alpha_s=0.35$.

evolution. (The situation is further complicated by the impact of running coupling corrections, which also come in at the single-logarithmic order.) Saturation corrections are highly likely to significantly modify all of the small-x helicity asymptotics we have derived above in the linearized approximation, most likely suppressing the contributions to the proton spin coming from very low x. The interplay of all these phenomena needs to be better understood in order to determine if or how the oscillatory pattern we observed in this section will exhibit itself in actual experimental measurements at small x.

IV. CROSS-CHECKS

A. Effect of different initial conditions

In this section we consider two different approximations to the initial conditions discussed in Sec. II B. The first approximation comes from the Born-level amplitude given in Eq. (18). With i and j defined in Eq. (22), the Born-level initial condition for G_2, Eq. (18b), discretizes to

$$G_{2,ij}^{(0)} = -\frac{\alpha_s^2 C_F}{2N_c}\pi\sqrt{\frac{2\pi}{\alpha_s N_c}}\, i\delta. \tag{53}$$

(For simplicity, we have put the θ-function in Eq. (18b) to one.) As for the type-1 dipole amplitudes, the initial condition involves the true infrared cutoff, Λ_{IR}, such that $1/\Lambda_{\mathrm{IR}}$ must be greater than any transverse separation encountered in the calculation. This warrants the definition of $s_{\min}$, such that

$$s_{\min} = \sqrt{\frac{\alpha_s N_c}{2\pi}}\ln\frac{\Lambda^2}{\Lambda_{\mathrm{IR}}^2}. \tag{54}$$

In term of $s_{\min}$, the infrared cutoff condition, $x_{10} \ll \frac{1}{\Lambda_{\mathrm{IR}}}$, becomes $s_{10} > -s_{\min}$. Then, the discretized Born-level initial condition for the type-1 dipole amplitudes is

$$\begin{aligned} Q_{ij}^{(0)} &= \tilde{G}_{ij}^{(0)} \\ &= \frac{\alpha_s^2 C_F}{2N_c}\pi\sqrt{\frac{2\pi}{\alpha_s N_c}}\,\delta\Big[C_F(j+i_{\min}) - 2\ \min\{j-i, j\}\Big], \end{aligned} \tag{55}$$

where we defined $i_{\min}$ such that $s_{\min}=i_{\min}\delta$.

The other constant (or the "all-one") approximation to the initial conditions is

$$Q_{ij}^{(0)} = \tilde{G}_{ij}^{(0)} = G_{2,ij}^{(0)} = 1. \tag{56}$$

Relying on the results from the previous section that the dipole amplitudes grow exponentially in magnitude with η, one would expect that the difference between the dipole amplitudes sourced by this initial condition and by its Born-level counterpart, which grows at most linearly with η, should be negligible, reduced perhaps to the overall normalization factor at large η. This was shown to be the case at large N_c in [1,7,8].

However, at large N_c & N_f, it was argued in [4] for the previous version of our small-x helicity evolution, which did not include the type-2 dipole amplitude, that different initial conditions can lead to a significant difference in detailed behavior of the solution.[3] It is worth noting that [4] compared the initial condition in Eq. (56) against the Born-level initial condition with Λ still taken to be an IR cutoff.

In this section we show that the difference is unlikely to persist for the revised helicity evolution [1] once we select the initial conditions that correctly treat Λ as a scale corresponding to the target's transverse size and use a different scale for the infrared cutoff. Specifically, we show numerically that the initial condition given by Eq. (56) and that given by Eqs. (53) and (55) only result in small differences in the parameters of the asymptotic solutions (27) and (39). Furthermore, the shapes of the amplitudes are qualitatively the same.

The correct treatment of Λ in the Born-level initial condition is of physical importance. When the target size, $1/\Lambda$, also acts as an infrared cutoff for the projectile dipole's size, x_{10}, the target-projectile symmetry of the (linear) evolution is explicitly broken. The target-projectile symmetry is the symmetry under the transformation $x_{10} \leftrightarrow \frac{1}{\Lambda}$ while keeping the center-of-mass energy squared s fixed. Ultimately, if the asymptotic solutions had no significant dependence on the choices of initial conditions, as long as the latter respect the target-projectile symmetry and do not grow faster than a polynomial of η and s_{10}, the

---

[3] In [4], the solution also takes the similar form of an exponential in η multiplied by a sinusoidal function of η. There, different initial conditions result in the same intercept and oscillation frequency, but they lead to different initial phases for the oscillation.

TABLE VIII. Summary of the parameter estimates and uncertainties for all types of polarized dipole amplitudes along the $s_{10} = 0$ line. Here, the number of quark flavors and colors are taken to be $N_f = 4$ and $N_c = 3$, respectively. The computation is performed with step size $\delta = 0.1$, maximum rapidity $\eta_{\max} = 50$, and the all-one initial condition (56).

Dipole amplitudes	Intercept (α)
$Q(0,\eta)$	3.28966 ± 0.00008
$G_2(0,\eta)$	3.28963 ± 0.00008
$\tilde{G}(0,\eta)$	3.28975 ± 0.00008

TABLE X. Summary of the parameter estimates and uncertainties for all types of polarized dipole amplitudes along the $s_{10} = 0$ line. Here, the number of quark flavors and colors are taken to be $N_f = 4$ and $N_c = 3$, respectively. The computation is performed with the step size $\delta = 0.1$, maximum rapidity $\eta_{\max} = 50$, and the Born-level initial condition from Eqs. (53) and (55).

Dipole amplitudes	Intercept (α)
$Q(0,\eta)$	3.28968 ± 0.00008
$G_2(0,\eta)$	3.28958 ± 0.00008
$\tilde{G}(0,\eta)$	3.28984 ± 0.00007

conclusion of the target-projectile symmetry of our helicity evolution would generalize to the exact initial condition derived from the experimental results at moderate x. Consequently, the asymptotic results from our numerical calculation obtained with the simpler initial condition (56) could be applied in the small-x region for rigorous large-N_c & N_f phenomenological studies.

Another consequence of the fact that initial conditions negligibly affect the solution is that they can be linearly combined without any significant change to the results. A useful consequence of this is our freedom in choosing the fixed value of $s_{\min}$ from Eq. (54), as any change in $s_{\min}$ has the same result as adding a multiple of initial condition,

$$Q_{ij}^{(0)} = \tilde{G}_{ij}^{(0)} = 1 \quad \text{and} \quad G_{2,ij}^{(0)} = 0, \tag{57}$$

which respects the target-projectile symmetry, to the Born-level initial condition from Eqs. (53) and (55).

To compare the two choices of initial conditions, we perform the numerical computation as described in Sec. II at $N_f = 4$, 6 and $N_c = 3$, using the step size $\delta = 0.1$ and maximum rapidity $\eta_{\max} = 50$. First we employ the initial condition (56). The method is the same as the one described in Sec. III, resulting in the parameter estimates given in Table VIII for $N_f = 4$ and Table IX for $N_f = 6$.

For the second part, we repeat the calculation with the same numbers of flavors, step size ($\delta = 0.1$) and maximum rapidity ($\eta_{\max} = 50$). However, this time, we employ the Born-level initial conditions given in Eqs. (53) and (55), with $s_{\min} = 50$. Recall from above that the arbitrary choice of $s_{\min}$ merely amounts to adding multiples of initial condition (57) to the Born-level initial condition. Performing the parameter estimation process described in Sec. II, we obtain the results shown in Table X for $N_f = 4$ and Table XI for $N_f = 6$.

For $N_f = 4$, we compare Table VIII to Table X. The resulting intercepts for all amplitudes are the same up to their uncertainties, implying no significant difference in parameter estimates regardless of the choice of initial conditions. This numerically justifies our choice of using the all-one initial condition (56), which we decided to use for simplicity in Sec. II, instead of the Born-level approximation given in Eqs. (53) and (55).

As for $N_f = 6$, comparing Table IX to Table XI, we see that the frequencies and the phases differ from their respective counterparts by greater amounts than the associated uncertainties. However, once we compare the differences to the continuum-limit uncertainties, c.f. Table VII, the discrepancies become insignificant for the initial phase. As for the frequency, there is still a statistically significant but very small difference.

Finally, we show in Figs. 13 (for $N_f = 4$) and 14 (for $N_f = 6$) the plots of the logarithms of the absolute values of the dipole amplitudes along the $s_{10} = 0$ line. In each plot, corresponding to the specified polarized dipole amplitude, the blue dots are made of the values at discrete steps computed using the all-one initial condition (56), while the orange dots resulted from the Born-level initial conditions (53) and (55). All six plots show minimal differences in the values of the dipole amplitudes at $N_f = 4$ and $N_f = 6$. The only significant difference visible from the plots is on the initial phases of the oscillation at $N_f = 6$ in Fig. 14, which also seem to be minor themselves.

TABLE IX. Summary of the parameter estimates and uncertainties for all types of polarized dipole amplitudes along the $s_{10} = 0$ line. Here, the number of quark flavors and colors are taken to be $N_f = 6$ and $N_c = 3$, respectively. The computation is performed with the step size $\delta = 0.1$, maximum rapidity $\eta_{\max} = 50$, and the all-one initial condition (56).

Dipole amplitudes	Intercept (α)	Frequency (ω)	Initial phase (φ)
$Q(0,\eta)$	2.79 ± 0.01	0.146549 ± 0.000004	-0.947 ± 0.007
$G_2(0,\eta)$	2.79 ± 0.01	0.146604 ± 0.000004	-0.978 ± 0.007
$\tilde{G}(0,\eta)$	2.80 ± 0.01	0.145510 ± 0.000004	0.783 ± 0.007

TABLE XI. Summary of the parameter estimates and uncertainties for all types of polarized dipole amplitudes along the $s_{10} = 0$ line. Here, the number of quark flavors and colors are taken to be $N_f = 6$ and $N_c = 3$, respectively. The computation is performed with the step size $\delta = 0.1$, maximum rapidity, $\eta_{\max} = 50$, and the Born-level initial condition from Eqs. (53) and (55).

Dipole amplitudes	Intercept (α)	Frequency (ω)	Initial phase (φ)
$Q(0,\eta)$	2.79 ± 0.01	0.146895 ± 0.000004	-1.003 ± 0.007
$G_2(0,\eta)$	2.79 ± 0.01	0.146841 ± 0.000004	-1.014 ± 0.007
$\tilde{G}(0,\eta)$	2.80 ± 0.01	0.145141 ± 0.000004	0.753 ± 0.007

Most importantly, all qualitative features in the amplitudes are the same regardless of the choices of initial conditions. From this observation, we conclude that the all-one initial condition (26) is a viable simplification for all the computation in the large-N_c & N_f limit aimed at determining the small-x asymptotics, assuming any possible error caused by the choice of initial condition to be negligible.[4]

B. Target-projectile symmetry

In this section, we examine the target-projectile symmetry, which we briefly discussed in Sec. IV A, in the context of the Born-level initial condition. Target–projectile symmetry is indeed only possible if one treats the target and projectile on equal footing. Perhaps the cleanest process is to consider the double-spin asymmetry in the scattering of two transversely polarized virtual photons, $\gamma^* + \gamma^*$, each of which splits into a $q\bar{q}$ dipole: the dipoles then interact with each other in a polarization-dependent way. In [1] it was shown that a single virtual photon generates a dipole which interacts with the polarized target via the $Q + 2G_2$ linear combination of the dipole amplitudes. This combination gives the g_1 structure function, which in turn relates to the cross section of the helicity-dependent DIS process. Since our goal here is to verify the target-projectile symmetry of our helicity evolution (13), we will not consider the full $\gamma^* + \gamma^*$ scattering with the corresponding Born-level initial conditions, and will instead employ our evolution with the all-one initial conditions (56), concentrating on studying the properties of the $Q + 2G_2$ linear combination of dipole amplitudes under the target-projectile interchange.

Under the exchange between target and projectile, we switch $x_{10} \leftrightarrow \frac{1}{\Lambda}$, while keeping the center-of-mass energy squared, s, fixed. In terms of η and s_{10}, c.f. Eq. (20), this corresponds to the transformation

$$Q(s_{10},\eta) \to Q'(s_{10},\eta) \equiv Q(-s_{10},\eta - s_{10}),$$
$$G_2(s_{10},\eta) \to G_2'(s_{10},\eta) \equiv G_2(-s_{10},\eta - s_{10}). \qquad (58)$$

Thus, to check for target-projectile symmetry in the asymptotic solution, we need to check whether $Q + 2G_2 = Q' + 2G_2'$.

We start with the qualitative check through plots. First, notice that the dipole amplitudes and their primed counterparts are trivially equal along the $s_{10} = 0$ line, since $s_{10} = 0$ implies that $x_{10} = 1/\Lambda$. As a result, we need to examine the amplitudes at $s_{10} \neq 0$ in order to check for the target-projectile symmetry. In particular, we plot the logarithms of the absolute values of the dipole amplitudes along the $s_{10} = 10$ line. For the $N_f \leq 5$ case, we consider $N_f = 4$, which is qualitatively the same as the cases where $N_f = 2$, 3 or 5. The results are plotted in Fig. 15, where the blue dots describe the original amplitudes, while the orange dots describe the primed amplitudes with the target and the projectile interchanged.

In Fig. 15, we see that the curves are mostly parallel, implying that intercepts appear unchanged under the target-projectile exchange. However, the lines seem to shift slightly downward after the exchange, implying that $\frac{Q+2G_2}{Q'+2G_2'}$ approaches 1 for sufficiently large η, roughly for $\eta \gtrsim 20$. Hence, from the plot, the linear combination of primed and unprimed amplitudes seem to have the same leading asymptotic behavior.

To make the comparison more quantitative, we employ the same method as in Sec. III B to estimate the intercept at large η along the $s_{10} = 10$ line. Repeating the process for the values of the step size δ and maximum rapidity $\eta_{\max}$ listed in Table II, we obtain the intercepts for each amplitude and each N_f in the continuum limit ($\delta \to 0$ and $\eta_{\max} \to \infty$) listed in Table XII. Similar to Sec. III B, the quadratic model fits the best with the intercept results. In Table XII the uncertainty accounts for the residue from the quadratic model. It is slightly higher than its counterpart in Sec. III B because we have fewer data points at $s_{10} = 10$ than at $s_{10} = 0$, as our helicity evolution only takes place at $\eta \geq s_{10}$. For each N_f, we see from Table XII that the intercepts for the primed and unprimed amplitudes are the same within the uncertainty. This implies that $Q + 2G_2$ respects the target-projectile symmetry in their large-η asymptotics for the $N_f \leq 5$ cases where there is no oscillation.

Now, we move on to consider the case where $N_f = 6$, for which the plot for $\ln|Q(10,\eta) + 2G_2(10,\eta)|$ and its primed

---

[4] This simplifying assumption was also employed in [4] where the large-N_c & N_f equations without the type-2 dipole amplitude were solved numerically.

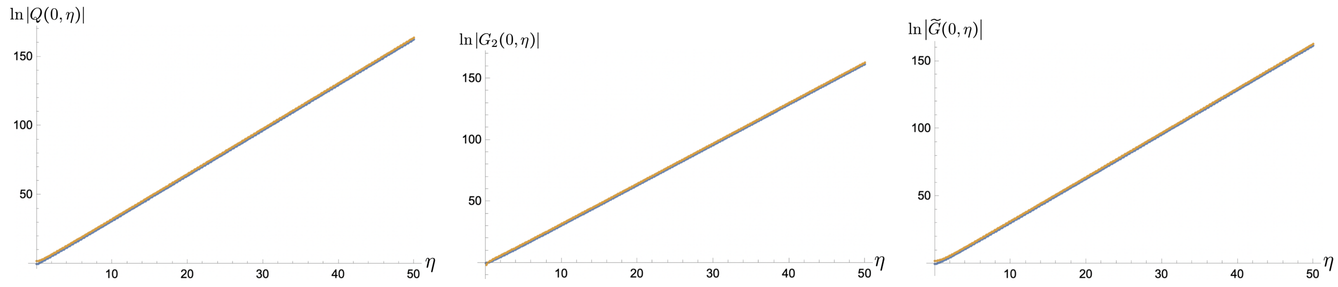

(a) $\ln|Q(0,\eta)|$ (b) $\ln|G_2(0,\eta)|$ (c) $\ln\left|\widetilde{G}(0,\eta)\right|$

FIG. 13. Plots of $\ln|Q(0,\eta)|$, $\ln|G_2(0,\eta)|$ and $\ln|\tilde{G}(0,\eta)|$ versus η at $N_f = 4$ and $N_c = 3$. All the graphs are numerically computed with step size $\delta = 0.1$ and $\eta_{\max} = 50$. In each plot, the blue dots are computed using the all-one initial condition (26), while the orange dots are computed using the Born-level initial conditions (53) and (55).

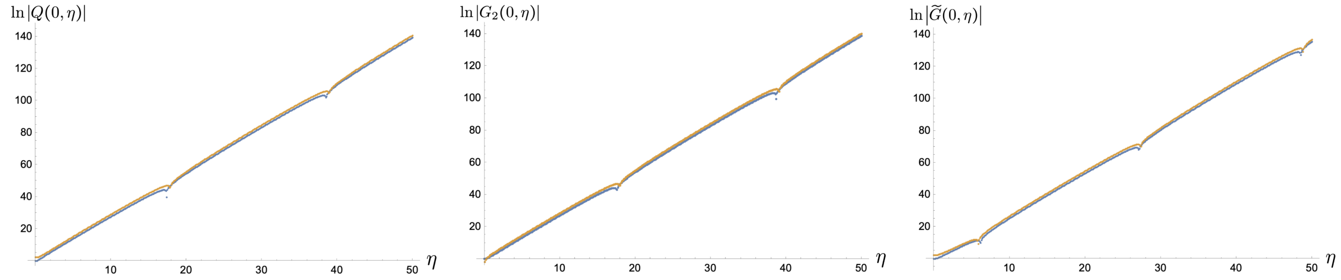

(a) $\ln|Q(0,\eta)|$ (b) $\ln|G_2(0,\eta)|$ (c) $\ln\left|\widetilde{G}(0,\eta)\right|$

FIG. 14. Plots of $\ln|Q(0,\eta)|$, $\ln|G_2(0,\eta)|$ and $\ln|\tilde{G}(0,\eta)|$ versus η at $N_f = 6$ and $N_c = 3$. All the graphs are numerically computed with step size $\delta = 0.1$ and $\eta_{\max} = 50$. In each plot, the blue dots are computed using the all-one initial condition (26), while the orange dots are computed using the Born-level initial conditions (53) and (55).

counterparts is shown in Fig. 16. Qualitatively, the only parameter that may significantly violate target-projectile symmetry is the initial phase.

To see the potential violation more clearly, we compute the parameter estimates for the large-η asymptotics of the amplitudes and their primed counterparts along the $s_{10} = 10$ line. Repeating the computation and the parameter evaluation steps outlined in Sec. III C for several values of step size δ and maximum rapidity $\eta_{\max}$, we deduce the continuum-limit estimates, $\delta = 1/\eta_{\max} = 0$, through the weighted polynomial regression method described in Sec. III C. At the end, we obtain the continuum-limit parameter estimates listed in Table XIII. Surprisingly, the initial phase discrepancies are within the uncertainties, but the frequencies do have significant discrepancies. However, the difference itself is only within 0.15%. Altogether, we conclude that $Q + 2G_2$, which is the object that yields the g_1 structure function, respects the target-projectile symmetry for any general N_f.

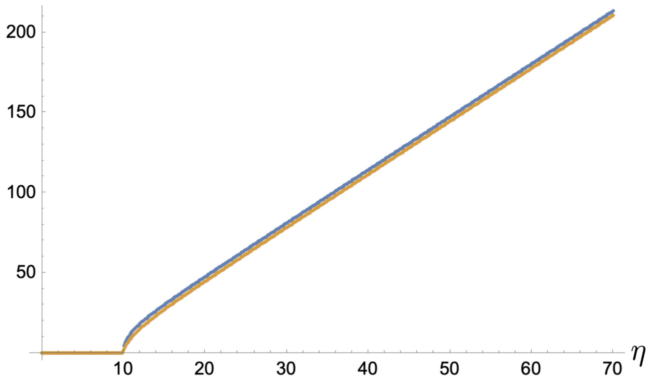

FIG. 15. Plot of $\ln|Q(10,\eta) + 2G_2(10,\eta)|$ (blue) and $\ln|Q'(10,\eta) + 2G_2'(10,\eta)|$ (orange) versus η at $N_f = 4$, $N_c = 3$, and $s_{10} = 10$. Both curves are numerically computed using the all-one initial condition with step size $\delta = 0.1$ and $\eta_{\max} = 70$.

TABLE XII. Summary of the estimates and uncertainties of the intercepts, α, for $Q + 2G_2$ and $Q' + 2G_2'$ along the $s_{10} = 10$ line. Here, the number of quark colors is taken to be $N_c = 3$. The computation is performed with the all-one initial condition (56).

N_f	$Q(10,\eta) + 2G_2(10,\eta)$	$Q'(10,\eta) + 2G_2'(10,\eta)$
2	3.52 ± 0.02	3.52 ± 0.03
3	3.42 ± 0.02	3.43 ± 0.02
4	3.32 ± 0.01	3.33 ± 0.01

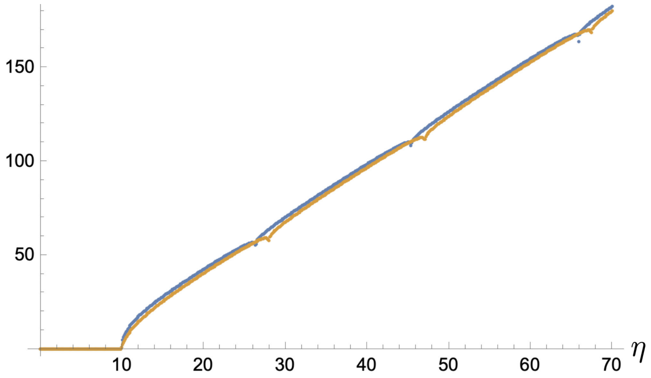

FIG. 16. Plot of $\ln|Q(10,\eta)+2G_2(10,\eta)|$ (blue) and $\ln|Q'(10,\eta)+2G_2'(10,\eta)|$ (orange) versus η at $N_f=6$, $N_c=3$ and $s_{10}=10$. Both curves are numerically computed using the all-one initial condition with step size $\delta=0.1$ and $\eta_{\max}=70$.

V. COMPARISON WITH THE POLARIZED DGLAP EVOLUTION

Similar to what was done in [1] for the large-N_c version of our helicity evolution, let us now attempt an iterative cross-check of the large-N_c & N_f version of helicity evolution. While it would be better to solve Eq. (13) analytically (cf. [17] for the large-N_c limit), in absence of such a solution at present we will solve Eq. (13) iteratively and compare the results to the finite-order calculations based on the Dokshitzer-Gribov-Lipatov-Altarelli-Parisi (DGLAP) evolution equations [81,82,96].

The polarized DGLAP evolution equation [81,82,96] is the renormalization group equation for the quark and gluon helicity PDFs. Physically, each step of the evolution corresponds to an emission of a daughter parton in such a way that the transverse momenta of the partons are strongly ordered. As a result, the small-x limit of DGLAP equations should be contained in the KPS-CTT evolution, particularly in the terms driven by the type-2 polarized dipole amplitude, $G_2(x_{10}^2, zs)$. Hence, it is useful to further cross-check the large-N_c & N_f KPS-CTT evolution by investigating whether or not its iteration reproduces the small-x limit of the polarized DGLAP kernels. There are several caveats in such a comparison, which we will outline below.

Throughout this section, we re-introduce the role of Λ as the infrared cutoff for the transverse dipole size in the KPS-CTT evolution, in order to be in line with how the polarized DGLAP evolution is set up. Treating Λ as the IR cutoff was important in the comparison of the iterative solution of the large-N_c helicity evolution to polarized DGLAP equation in [1]. This results in the following large-N_c & N_f evolution equations with the IR cutoff Λ:

$$\begin{aligned} Q(x_{10}^2, zs) = {} & Q^{(0)}(x_{10}^2, zs) + \frac{\alpha_s N_c}{2\pi} \int_{1/sx_{10}^2}^{z} \frac{dz'}{z'} \int_{1/z's}^{x_{10}^2} \frac{dx_{21}^2}{x_{21}^2} \Big[2\tilde{G}(x_{21}^2, z's) + 2\tilde{\Gamma}(x_{10}^2, x_{21}^2, z's) \\ & + Q(x_{21}^2, z's) - \bar{\Gamma}(x_{10}^2, x_{21}^2, z's) + 2\Gamma_2(x_{10}^2, x_{21}^2, z's) + 2G_2(x_{21}^2, z's) \Big] \\ & + \frac{\alpha_s N_c}{4\pi} \int_{\Lambda^2/s}^{z} \frac{dz'}{z'} \int_{1/z's}^{\min\{x_{10}^2 z/z', 1/\Lambda^2\}} \frac{dx_{21}^2}{x_{21}^2} \Big[Q(x_{21}^2, z's) + 2G_2(x_{21}^2, z's) \Big], \end{aligned} \tag{59a}$$

$$\begin{aligned} \bar{\Gamma}(x_{10}^2, x_{21}^2, z's) = {} & Q^{(0)}(x_{10}^2, z's) + \frac{\alpha_s N_c}{2\pi} \int_{1/sx_{10}^2}^{z'} \frac{dz''}{z''} \int_{1/z''s}^{\min\{x_{10}^2, x_{21}^2 z'/z''\}} \frac{dx_{32}^2}{x_{32}^2} \Big[2\tilde{G}(x_{32}^2, z''s) \\ & + 2\tilde{\Gamma}(x_{10}^2, x_{32}^2, z''s) + Q(x_{32}^2, z''s) - \bar{\Gamma}(x_{10}^2, x_{32}^2, z''s) + 2\Gamma_2(x_{10}^2, x_{32}^2, z''s) + 2G_2(x_{32}^2, z''s) \Big] \\ & + \frac{\alpha_s N_c}{4\pi} \int_{\Lambda^2/s}^{z'} \frac{dz''}{z''} \int_{1/z''s}^{\min\{x_{21}^2 z'/z'', 1/\Lambda^2\}} \frac{dx_{32}^2}{x_{32}^2} \Big[Q(x_{32}^2, z''s) + 2G_2(x_{32}^2, z''s) \Big], \end{aligned} \tag{59b}$$

TABLE XIII. Summary of the parameter estimates and uncertainties at the continuum limit ($\delta \to 0$ and $\eta_{\max} \to \infty$) for $Q(10,\eta)+2G_2(10,\eta)$ and $Q'(10,\eta)+2G_2'(10,\eta)$ along the $s_{10}=10$ line. Here, the number of quark flavors and colors are taken to be $N_f=6$ and $N_c=3$, respectively. The computation is performed with the all-one initial condition (56).

Dipole amplitudes	Intercept (α)	Frequency (ω)	Initial phase (φ)
$Q(10,\eta)+2G_2(10,\eta)$	2.81 ± 0.04	0.16146 ± 0.00008	-1.62 ± 0.07
$Q'(10,\eta)+2G_2'(10,\eta)$	2.82 ± 0.04	0.16169 ± 0.00008	-1.55 ± 0.09

$$\begin{aligned}\tilde{G}(x_{10}^2, zs) &= \tilde{G}^{(0)}(x_{10}^2, zs) + \frac{\alpha_s N_c}{2\pi}\int_{1/sx_{10}^2}^{z}\frac{dz'}{z'}\int_{1/z's}^{x_{10}^2}\frac{dx_{21}^2}{x_{21}^2}\Big[3\tilde{G}(x_{21}^2, z's) + \tilde{\Gamma}(x_{10}^2, x_{21}^2, z's)\\ &\quad + 2G_2(x_{21}^2, z's) + \left(2 - \frac{N_f}{2N_c}\right)\Gamma_2(x_{10}^2, x_{21}^2, z's) - \frac{N_f}{4N_c}\bar{\Gamma}(x_{10}^2, x_{21}^2, z's)\Big]\\ &\quad - \frac{\alpha_s N_f}{8\pi}\int_{\Lambda^2/s}^{z}\frac{dz'}{z'}\int_{\max\{x_{10}^2, 1/z's\}}^{\min\{x_{10}^2 z/z', 1/\Lambda^2\}}\frac{dx_{21}^2}{x_{21}^2}\Big[Q(x_{21}^2, z's) + 2G_2(x_{21}^2, z's)\Big],\end{aligned} \tag{59c}$$

$$\begin{aligned}\tilde{\Gamma}(x_{10}^2, x_{21}^2, z's) &= \tilde{G}^{(0)}(x_{10}^2, z's) + \frac{\alpha_s N_c}{2\pi}\int_{1/sx_{10}^2}^{z'}\frac{dz''}{z''}\int_{1/z''s}^{\min\{x_{10}^2, x_{21}^2 z'/z''\}}\frac{dx_{32}^2}{x_{32}^2}\Big[3\tilde{G}(x_{32}^2, z''s)\\ &\quad + \tilde{\Gamma}(x_{10}^2, x_{32}^2, z''s) + 2G_2(x_{32}^2, z''s) + \left(2 - \frac{N_f}{2N_c}\right)\Gamma_2(x_{10}^2, x_{32}^2, z''s) - \frac{N_f}{4N_c}\bar{\Gamma}(x_{10}^2, x_{32}^2, z''s)\Big]\\ &\quad - \frac{\alpha_s N_f}{8\pi}\int_{\Lambda^2/s}^{z'x_{21}^2/x_{10}^2}\frac{dz''}{z''}\int_{\max\{x_{10}^2, 1/z''s\}}^{\min\{x_{21}^2 z'/z'', 1/\Lambda^2\}}\frac{dx_{32}^2}{x_{32}^2}\Big[Q(x_{32}^2, z''s) + 2G_2(x_{32}^2, z''s)\Big],\end{aligned} \tag{59d}$$

$$G_2(x_{10}^2, zs) = G_2^{(0)}(x_{10}^2, zs) + \frac{\alpha_s N_c}{\pi}\int_{\frac{\Lambda^2}{s}}^{z}\frac{dz'}{z'}\int_{\max[x_{10}^2, \frac{1}{z's}]}^{\min\{\frac{z}{z'}x_{10}^2, 1/\Lambda^2\}}\frac{dx_{21}^2}{x_{21}^2}[\tilde{G}(x_{21}^2, z's) + 2G_2(x_{21}^2, z's)], \tag{59e}$$

$$\Gamma_2(x_{10}^2, x_{21}^2, z's) = G_2^{(0)}(x_{10}^2, z's) + \frac{\alpha_s N_c}{\pi}\int_{\frac{\Lambda^2}{s}}^{z'\frac{x_{21}^2}{x_{10}^2}}\frac{dz''}{z''}\int_{\max[x_{10}^2, \frac{1}{z''s}]}^{\min\{\frac{z'}{z''}x_{21}^2, 1/\Lambda^2\}}\frac{dx_{32}^2}{x_{32}^2}[\tilde{G}(x_{32}^2, z''s) + 2G_2(x_{32}^2, z''s)]. \tag{59f}$$

A. The setup

The polarized DGLAP equation written in the integral form reads

$$\begin{pmatrix}\Delta\Sigma(x, Q^2)\\ \Delta G(x, Q^2)\end{pmatrix} = \begin{pmatrix}\Delta\Sigma(x, \Lambda^2)\\ \Delta G(x, \Lambda^2)\end{pmatrix} + \int_{\Lambda^2}^{Q^2}\frac{d\mu^2}{\mu^2}\int_x^1\frac{dz}{z}\begin{pmatrix}\Delta P_{qq}(z) & \Delta P_{qG}(z)\\ \Delta P_{Gq}(z) & \Delta P_{GG}(z)\end{pmatrix}\begin{pmatrix}\Delta\Sigma(\frac{x}{z}, \mu^2)\\ \Delta G(\frac{x}{z}, \mu^2)\end{pmatrix}, \tag{60}$$

where the polarized splitting functions, $\Delta P_{ij}(z)$, depend on the longitudinal momentum fraction z. Generally, the splitting functions depend on the renormalization scheme. In the $\overline{\mathrm{MS}}$ scheme, their small-x limits at large-N_c & N_f are [81,82,84,88],

$$\Delta\tilde{P}_{qq}(x) = \left(\frac{\alpha_s}{4\pi}\right)N_c + \left(\frac{\alpha_s}{4\pi}\right)^2\frac{N_c}{2}(N_c - 4N_f)\ln^2\frac{1}{x} + \left(\frac{\alpha_s}{4\pi}\right)^3\frac{N_c^2}{12}(N_c - 20N_f)\ln^4\frac{1}{x} + \mathcal{O}(\alpha_s^4), \tag{61a}$$

$$\Delta\tilde{P}_{qG}(x) = -\left(\frac{\alpha_s}{4\pi}\right)2N_f - \left(\frac{\alpha_s}{4\pi}\right)^2 5N_c N_f\ln^2\frac{1}{x} - \left(\frac{\alpha_s}{4\pi}\right)^3\frac{N_c N_f}{3}(17N_c - 3N_f)\ln^4\frac{1}{x} + \mathcal{O}(\alpha_s^4), \tag{61b}$$

$$\Delta\tilde{P}_{Gq}(x) = \left(\frac{\alpha_s}{4\pi}\right)2N_c + \left(\frac{\alpha_s}{4\pi}\right)^2 5N_c^2\ln^2\frac{1}{x} + \left(\frac{\alpha_s}{4\pi}\right)^3\frac{2}{3}N_c^2(9N_c - N_f)\ln^4\frac{1}{x} + \mathcal{O}(\alpha_s^4), \tag{61c}$$

$$\Delta\tilde{P}_{GG}(x) = \left(\frac{\alpha_s}{4\pi}\right)8N_c + \left(\frac{\alpha_s}{4\pi}\right)^2 2N_c(8N_c - N_f)\ln^2\frac{1}{x} + \left(\frac{\alpha_s}{4\pi}\right)^3\frac{N_c^2}{3}(56N_c - 11N_f)\ln^4\frac{1}{x} + \mathcal{O}(\alpha_s^4). \tag{61d}$$

From now on, we use tildes to denote the polarized splitting functions and the helicity PDFs ($\Delta\tilde{\Sigma}$, $\Delta\tilde{G}$) in the $\overline{\mathrm{MS}}$ scheme.

In general, the g_1 structure function can be written as a linear combination of the quark and gluon helicity PDFs convoluted (over x) with the coefficient functions. While both the hPDFs and the coefficient functions are renormalization scheme-dependent, the g_1 structure function is indeed a physical observable and is independent of a scheme. In our small-x

formalism, defining $\Delta q_f^+ = \Delta q_f + \Delta\bar{q}_f$ [15,97] with Δq_f and $\Delta\bar{q}_f$ the quark and antiquark helicity distributions for each quark flavor f, we can write [1] (also cf. Eqs. (15) and (16a) above)

$$g_1(x,Q^2) = \frac{1}{2}\sum_f Z_f^2 \Delta q_f^+(x,Q^2), \tag{62a}$$

$$\Delta\Sigma(x,Q^2) = \sum_f \Delta q_f^+(x,Q^2), \tag{62b}$$

with

$$\Delta q_f^+(x,Q^2) = -\frac{N_c}{2\pi^3}\int_{\Lambda^2/s}^{1}\frac{dz}{z} \times \int_{\frac{1}{zs}}^{\min\left\{\frac{1}{zQ^2},\frac{1}{\Lambda^2}\right\}} \frac{dx_{10}^2}{x_{10}^2}\left[Q(x_{10}^2,zs) + 2G_2(x_{10}^2,zs)\right]. \tag{63}$$

These relations are valid to all orders in $\alpha_s \ln^2(1/x)$ and $\alpha_s \ln(1/x)\ln(Q^2/\Lambda^2)$. Note the particularly simple relation (62a) between the g_1 structure function and quark hPDFs. This is similar to the DIS scheme [98], in which the $F_2(x,Q^2)$ structure function is also related to the unpolarized quark PDFs, $q_f^+ = q_f + \bar{q}_f$, to all orders in α_s, via the simple leading-order (LO) relation, $F_2(x,Q^2) = \sum_f Z_f^2 x q_f^+(x,Q^2)$. Therefore, our calculation, preserving the LO relation (62a) to all orders in α_s, can be thought of as being in the "polarized DIS scheme" or "pDIS scheme." Below, the helicity PDFs and polarized splitting functions in our pDIS scheme will be written without the tilde, in contrast to their counterparts in the $\overline{\mathrm{MS}}$ scheme.

If we choose flavor-independent initial conditions for the evolution equation (13), we obtain a simple relation between the g_1 structure function and $\Delta\Sigma$,

$$g_1(x,Q^2) = \frac{1}{2N_f}\left(\sum_f Z_f^2\right)\Delta\Sigma(x,Q^2). \tag{64}$$

We conclude that, when comparing to the fixed-order calculations, our $\Delta\Sigma$ should be compared to the results for g_1 structure function, while taking the proportionality factor between the two from Eq. (64) into account.

The factorized structure function g_1 can be written as the convolution of the coefficient functions and hPDFs (see the discussion in [91]). We, therefore, write the quark hPDF in the pDIS scheme at next-to-leading order (NLO) as

$$\Delta\Sigma(x,Q^2) = \Delta\tilde{\Sigma}(x,Q^2) + \int_x^1\frac{dz}{z}\left[\Delta c_q(z)\Delta\tilde{\Sigma}\left(\frac{x}{z},Q^2\right) + \Delta c_G(z)\Delta\tilde{G}\left(\frac{x}{z},Q^2\right)\right], \tag{65}$$

in terms of the quark and gluon hPDFs $\Delta\tilde{\Sigma}$ and $\Delta\tilde{G}$ in the $\overline{\mathrm{MS}}$ scheme. Here the small-x large-N_c & N_f coefficient functions are [83]

$$\Delta c_q(z) = \frac{\alpha_s N_c}{4\pi}\ln\frac{1}{z} + \frac{5}{12}\left(\frac{\alpha_s N_c}{4\pi}\right)^2\left[1 - 4\frac{N_f}{N_c}\right]\ln^3\frac{1}{z} + \mathcal{O}(\alpha_s^3), \tag{66a}$$

$$\Delta c_G(z) = -\frac{\alpha_s N_f}{2\pi}\ln\frac{1}{z} - \frac{11}{2}\left(\frac{\alpha_s}{4\pi}\right)^2 N_c N_f \ln^3\frac{1}{z} + \mathcal{O}(\alpha_s^3). \tag{66b}$$

However, the order-by-order in α_s solution of the small-x helicity evolution equation we are about to perform should be compared to the unfactorized partonic structure function $\hat{g}_1$. That means, instead of Eq. (65) we should write [83,91]

$$\Delta\hat{\Sigma}_j(x,\epsilon) = \sum_{i=q,G}\left[\Delta C_i(\epsilon)\otimes Z_{ij}(\epsilon)\right](x) \tag{67}$$

for the quark hPDF sourced by the parton $j = q, G$. Here the transition matrix is $Z_{ij} = 1 + \frac{1}{\epsilon}\Delta\tilde{P}_{ij}^{(1)}(z) + \cdots$ with $\Delta\tilde{P}_{ij}^{(1)}(z)$ the order-α_s contribution to the splitting functions from Eq. (61). The dimensional regularization parameter is $\epsilon = d - 4$ with d the number of space-time dimensions. We defined the $\otimes$ operation such that

$$[f\otimes g](x,Q^2) = \int_x^1\frac{dz}{z}[f(z)]\left[g\left(\frac{x}{z}\right)\right], \tag{68}$$

for any pair of functions f and g.

The coefficient functions now are (see, e.g., [87])

$$\Delta C_i(z,\epsilon) = \delta_{iq}\delta(1-z) + \sum_{l=1}^{\infty}\left[\Delta c_i^{(l)}(z) + \epsilon\Delta a_i^{(l)}(z) + \epsilon^2\Delta b_i^{(l)}(z) + \ldots\right], \tag{69}$$

with the coefficient functions in Eq. (66) given by the $\epsilon \to 0$ limit of Eq. (69),

$$\Delta c_i(z) = \delta_{iq}\delta(1-z) + \sum_{l=1}^{\infty}\Delta c_i^{(l)}(z). \tag{70}$$

Here the superscript l denotes the order of α_s in each term.

The coefficients $\Delta a_i^{(l)}(z)$ and $\Delta b_i^{(l)}(z)$ contribute at finite orders in α_s. Below we will find it useful that for the $\hat{g}_1$ structure function and the corresponding quark hPDF sourced by a gluon, the finite (in the $\epsilon \to 0$ limit) term at the order-α_s^2 is [83]

$$\Delta\hat{\Sigma}_G(x) \supset \Delta c_g^{(2)} + \Delta P_{GG}^{(1)} \otimes \Delta a_G^{(1)} + \Delta P_{qG}^{(1)} \otimes \Delta a_q^{(1)} \tag{71}$$

with [83]

$$\Delta a_G^{(1)}(z) = -\frac{\alpha_s N_f}{8\pi}\ln^2 z, \qquad \Delta a_q^{(1)} = \frac{\alpha_s N_c}{16\pi}\ln^2 z \tag{72}$$

in the $z \ll 1$ and the large-N_c & N_f limits.

As discussed earlier, the DGLAP-type parton emission is driven in the KPS-CTT evolution by the terms involving the type-2 polarized dipole amplitude. In order to perform the crosscheck, it is then reasonable to work, for simplicity, with the initial condition such that only $G_2(x_{10}^2, zs)$ is nonzero (cf. [1]). In particular, we take

$$G_2^{(0)} = \frac{\alpha_s \pi^2}{2N_c} \quad \text{and} \quad Q^{(0)} = \tilde{G}^{(0)} = 0 \tag{73}$$

as the initial condition of our small-x evolution. With the help of Eq. (16), this translates to the following helicity PDFs in our pDIS scheme:

$$\Delta G^{(0)}(x, Q^2) = 1 \quad \text{and} \quad \Delta\Sigma^{(0)}(x, Q^2) = 0. \tag{74}$$

Below we will calculate ΔG and $\Delta\Sigma$ order-by-order in α_s, such that

$$\Delta\Sigma(x, Q^2) = \Delta\Sigma^{(0)}(x, Q^2) + \Delta\Sigma^{(1)}(x, Q^2) + \Delta\Sigma^{(2)}(x, Q^2) + \dots, \tag{75a}$$

$$\Delta G(x, Q^2) = \Delta G^{(0)}(x, Q^2) + \Delta G^{(1)}(x, Q^2) + \Delta G^{(2)}(x, Q^2) + \dots, \tag{75b}$$

where the index in the superscript corresponds to the power of α_s correction to $\Delta\Sigma^{(0)}$ and $\Delta G^{(0)}$ from Eq. (74).

B. Order-α_s corrections

Before iterating the small-x evolution, we substitute the initial condition (73) into Eq. (16a) for the quark helicity PDF. This gives

$$\Delta\Sigma^{(1)}(x, Q^2) = -\frac{\alpha_s N_f}{2\pi}\left[\frac{1}{2}\ln^2\frac{1}{x} + \ln\frac{1}{x}\ln\frac{Q^2}{\Lambda^2}\right], \tag{76}$$

which is of order-α_s. Hence, the result (76) is more properly associated with the first-order quark helicity PDF. This shift in the order is consistent with the fact that the operator definition of $\Delta\Sigma$ already involves one parton loop at small x [1,3]. Finally, notice that the additional power of α_s brings two additional logarithmic factors, each of which is either transverse ($\ln\frac{Q^2}{\Lambda^2}$) or longitudinal ($\ln\frac{1}{x}$). This is consistent with the DLA nature of the small-x helicity evolution.

Now, we are ready to iterate the evolution. First, we substitute Eq. (73) into the KPS-CTT evolution equations (59). From Eq. (59e), we obtain the first-order polarized dipole amplitude,

$$G_2^{(1)}(x_{10}^2, zs) = \frac{2\alpha_s N_c}{\pi}\ln(zsx_{10}^2)\ln\left(\frac{1}{x_{10}^2\Lambda^2}\right)G_2^{(0)}, \tag{77}$$

which, via Eq. (16b), yields the first-order gluon helicity PDF of

$$\Delta G^{(1)}(x, Q^2) = \frac{2\alpha_s N_c}{\pi}\ln\frac{1}{x}\ln\frac{Q^2}{\Lambda^2}. \tag{78}$$

Let us compare the results in Eqs. (76) and (78) to the predictions of the finite-order DGLAP-based calculations. First we note that the initial conditions (73) for small-x evolution in pDIS scheme may not map precisely onto the initial conditions for the DGLAP evolution (60) in the $\overline{\text{MS}}$ scheme. We thus write, in full generality,

$$\Delta\tilde{G}(x, \Lambda^2) = 1 + \sum_{n=1}^{\infty} a_n\left(\alpha_s \ln^2\frac{1}{x}\right)^n, \tag{79a}$$

$$\Delta\tilde{\Sigma}(x, \Lambda^2) = \sum_{n=1}^{\infty} b_n\left(\alpha_s \ln^2\frac{1}{x}\right)^n, \tag{79b}$$

with a_n's and b_n's some unknown parameters.

Employing Eq. (79) along with Eq. (61) in Eq. (60) yields the order-α_s hPDFs in the $\overline{\text{MS}}$ scheme:

$$\Delta\tilde{G}^{(1)}(x, Q^2) = \alpha_s\left[a_1\ln^2\frac{1}{x} + \frac{2N_c}{\pi}\ln\frac{1}{x}\ln\frac{Q^2}{\Lambda^2}\right], \tag{80a}$$

$$\Delta\tilde{\Sigma}^{(1)}(x, Q^2) = \alpha_s\left[b_1\ln^2\frac{1}{x} - \frac{N_f}{2\pi}\ln\frac{1}{x}\ln\frac{Q^2}{\Lambda^2}\right]. \tag{80b}$$

While a direct comparison of Eq. (80) to the hPDFs in Eqs. (76) and (78) is impossible, since the two sets of hPDFs are potentially in different schemes, we can employ Eq. (65), which readily yields

$$\Delta\Sigma^{(1)}(x, Q^2) = \Delta\tilde{\Sigma}^{(1)}(x, Q^2) + \int_x^1 \frac{dz}{z}\Delta c_G^{(1)}(z)\Delta\tilde{G}^{(0)}\left(\frac{x}{z}, Q^2\right) \tag{81}$$

for $b_1 = 0$. Here $\Delta c_g^{(1)}(z)$ is the order-α_s term in Eq. (66b). It appears that for the scheme-independent quantity, $\Delta\Sigma \sim g_1$, we have an agreement between the two approaches at this leading nontrivial order in α_s. The agreement requires that $b_1 = 0$.

We also note that Eq. (77) is in agreement with Eq. (80a) for $a_1 = 0$ in the latter, though at this point we cannot equate the two gluon distributions.

C. Order-α_s^2 corrections

Similar to the above, substituting Eq. (73) into Eq. (59a), we obtain

$$Q^{(1)}(x_{10}^2, zs) = \frac{\alpha_s N_c}{\pi}\left[\frac{5}{4}\ln^2(zsx_{10}^2) + \frac{1}{2}\ln\left(\frac{1}{x_{10}^2\Lambda^2}\right)\ln(zsx_{10}^2)\right]G_2^{(0)}. \tag{82}$$

Further, substituting Eqs. (77) and (82) into Eq. (16a) yields the second-order quark helicity PDF,

$$\Delta\Sigma^{(2)}(x, Q^2) = -\left(\frac{\alpha_s N_c}{\pi}\right)\left(\frac{\alpha_s N_f}{4\pi}\right)\left[\frac{7}{24}\ln^4\frac{1}{x} + \frac{7}{6}\ln^3\frac{1}{x}\ln\frac{Q^2}{\Lambda^2} + \frac{9}{8}\ln^2\frac{1}{x}\ln^2\frac{Q^2}{\Lambda^2}\right]. \tag{83}$$

Once again, using Eqs. (73) in Eq. (59c) gives us the first-order type-1 adjoint dipole amplitude,

$$\tilde{G}^{(1)} = \left[\frac{\alpha_s N_c}{2\pi}\left(2 - \frac{N_f}{4N_c}\right)\ln^2(zsx_{10}^2) - \frac{\alpha_s N_f}{4\pi}\ln(zsx_{10}^2)\ln\frac{1}{x_{10}^2\Lambda^2}\right]G_2^{(0)}. \tag{84}$$

We then substitute this result, together with Eq. (77), into Eq. (59e) in order to obtain the order-α_s^2 type-2 dipole amplitude, $G_2^{(2)}$. With the help of Eq. (16b), this result gives us the second-order gluon helicity PDF,

$$\Delta G^{(2)}(x, Q^2) = \left(\frac{\alpha_s N_c}{\pi}\right)^2\left[\frac{1}{3}\left(1 - \frac{N_f}{8N_c}\right)\ln^3\frac{1}{x}\ln\frac{Q^2}{\Lambda^2} + \left(1 - \frac{N_f}{16N_c}\right)\ln^2\frac{1}{x}\ln^2\frac{Q^2}{\Lambda^2}\right]. \tag{85}$$

Employing the initial conditions (79) with $b_1 = 0$ in Eq. (60) we obtain the following $\overline{\mathrm{MS}}$ hPDFs at the order-α_s^2:

$$\Delta\tilde{G}^{(2)}(x, Q^2) = \alpha_s^2\left\{a_2\ln^4\frac{1}{x} + \frac{2N_c}{3\pi}\left[\frac{N_c}{16\pi}\left(8 - \frac{N_f}{N_c}\right) + a_1\right]\ln^3\frac{1}{x}\ln\frac{Q^2}{\Lambda^2} + \frac{N_c^2}{\pi^2}\left(1 - \frac{N_f}{16N_c}\right)\ln^2\frac{1}{x}\ln^2\frac{Q^2}{\Lambda^2}\right\}, \tag{86a}$$

$$\Delta\tilde{\Sigma}^{(2)}(x, Q^2) = \alpha_s^2\left[b_2\ln^4\frac{1}{x} - \frac{N_f}{6\pi}\left(a_1 + \frac{5N_c}{8\pi}\right)\ln^3\frac{1}{x}\ln\frac{Q^2}{\Lambda^2} - \frac{9N_cN_f}{32\pi^2}\ln^2\frac{1}{x}\ln^2\frac{Q^2}{\Lambda^2}\right]. \tag{86b}$$

The agreement between Eqs. (83) and (86b) is obtained by using Eq. (65) augmented by Eq. (71), which at this order in α_s gives

$$\begin{aligned}\Delta\Sigma^{(2)}(x, Q^2) = \Delta\tilde{\Sigma}^{(2)}(x, Q^2) + \int_x^1\frac{dz}{z}\Big\{&\Delta c_q^{(1)}(z)\Delta\tilde{\Sigma}^{(1)}\left(\frac{x}{z}, Q^2\right) + \Delta c_G^{(1)}(z)\Delta\tilde{G}^{(1)}\left(\frac{x}{z}, Q^2\right)\\ &+ \left[\Delta c_G^{(2)} + \Delta P_{GG}^{(1)}\otimes\Delta a_G^{(1)} + \Delta P_{qG}^{(1)}\otimes\Delta a_q^{(1)}\right](z)\Delta\tilde{G}^{(0)}\left(\frac{x}{z}, Q^2\right)\Big\}.\end{aligned} \tag{87}$$

The agreement requires that

$$a_1 = 0, \qquad b_2 = \frac{23}{48}\frac{N_cN_f}{8\pi^2}. \tag{88}$$

Further, putting $a_2 = 0$ would make the $\overline{\mathrm{MS}}$ gluon hPDF contribution in Eq. (86a) agree with Eq. (85), though we do not expect these two hPDFs to be necessarily equal, as they may be in different renormalization schemes.

D. Order-α_s^3 corrections

Further iterations of small-x evolution equations Eq. (59), involving the calculation of the first-order neighbor dipole amplitudes and the second-order ordinary dipole amplitudes of all types lead to the third-order quark and gluon helicity PDFs,

$$\Delta\Sigma^{(3)}(x,Q^2) = -\frac{\alpha_s^3 N_c^2 N_f}{16\pi^3}\left[\frac{1}{1440}\left(221-20\frac{N_f}{N_c}\right)\ln^6\frac{1}{x}+\frac{1}{240}\left(221-20\frac{N_f}{N_c}\right)\ln^5\frac{1}{x}\ln\frac{Q^2}{\Lambda^2}\right.$$
$$\left.+\frac{1}{96}\left(151-12\frac{N_f}{N_c}\right)\ln^4\frac{1}{x}\ln^2\frac{Q^2}{\Lambda^2}+\frac{1}{72}\left(73-4\frac{N_f}{N_c}\right)\ln^3\frac{1}{x}\ln^3\frac{Q^2}{\Lambda^2}\right], \tag{89a}$$

$$\Delta G^{(3)}(x,Q^2) = \left(\frac{\alpha_s N_c}{\pi}\right)^3\left[\frac{1}{960}\left(56-13\frac{N_f}{N_c}\right)\ln^5\frac{1}{x}\ln\frac{Q^2}{\Lambda^2}\right.$$
$$\left.+\frac{1}{384}\left(64-15\frac{N_f}{N_c}\right)\ln^4\frac{1}{x}\ln^2\frac{Q^2}{\Lambda^2}+\frac{1}{576}\left(128-17\frac{N_f}{N_c}\right)\ln^3\frac{1}{x}\ln^3\frac{Q^2}{\Lambda^2}\right]. \tag{89b}$$

Thus, starting with the initial condition (73), we have determined the helicity PDFs at small x up to the third order in α_s through an iterative calculation of the evolution kernel in the KPS-CTT equations.

The corresponding $\overline{\mathrm{MS}}$ hPDFs at the order-α_s^3 are

$$\Delta\tilde{\Sigma}^{(3)}(x,Q^2) = -\frac{\alpha_s N_f}{4\pi}\left(\frac{\alpha_s N_c}{2\pi}\right)^2\left[\frac{1}{60}\left(17-3\frac{N_f}{N_c}\right)\ln\frac{Q^2}{\Lambda^2}\ln^5\frac{1}{x}+\frac{1}{48}\left(39-4\frac{N_f}{N_c}\right)\ln^2\frac{Q^2}{\Lambda^2}\ln^4\frac{1}{x}\right.$$
$$\left.+\frac{1}{72}\left(73-4\frac{N_f}{N_c}\right)\ln^3\frac{Q^2}{\Lambda^2}\ln^3\frac{1}{x}\right]+\alpha_s^3 b_3\ln^6\frac{1}{x}+\frac{\alpha_s^3}{20\pi}(N_c b_2-2N_f a_2)\ln\frac{Q^2}{\Lambda^2}\ln^5\frac{1}{x}, \tag{90a}$$

$$\Delta\tilde{G}^{(3)}(x,Q^2) = \left(\frac{\alpha_s N_c}{\pi}\right)^3\left[\frac{1}{3840}\left(224-39\frac{N_f}{N_c}\right)\ln^5\frac{1}{x}\ln\frac{Q^2}{\Lambda^2}+\frac{1}{384}\left(64-13\frac{N_f}{N_c}\right)\ln^4\frac{1}{x}\ln^2\frac{Q^2}{\Lambda^2}\right.$$
$$\left.+\frac{1}{576}\left(128-17\frac{N_f}{N_c}\right)\ln^3\frac{1}{x}\ln^3\frac{Q^2}{\Lambda^2}\right]+\alpha_s^3 a_3\ln^6\frac{1}{x}+\frac{\alpha_s^3 N_c}{10\pi}(b_2+4a_2)\ln\frac{Q^2}{\Lambda^2}\ln^5\frac{1}{x}. \tag{90b}$$

Concentrating on the cubic and quadratic terms in $\ln(Q^2/\Lambda^2)$ contributing to $\Delta\Sigma^{(3)}$, we observe that

$$\Delta\Sigma^{(3)}-\Delta\tilde{\Sigma}^{(3)}-\delta c_q^{(1)}\otimes\Delta\tilde{\Sigma}^{(2)}-\delta c_G^{(1)}\otimes\Delta G^{(2)}$$
$$=-\frac{\alpha_s N_f}{4\pi}\left(\frac{\alpha_s N_c}{2\pi}\right)^2\left[\frac{1}{1440}\left(221-20\frac{N_f}{N_c}\right)\ln^6\frac{1}{x}+\frac{1}{60}\left(29-\frac{N_f}{N_c}\right)\ln\frac{Q^2}{\Lambda^2}\ln^5\frac{1}{x}\right]. \tag{91}$$

The comparison of the linear terms in $\ln(Q^2/\Lambda^2)$ and the terms independent of Q^2 would require knowledge of $\Delta a_G^{(2)}$, $\Delta a_q^{(2)}$, $\Delta b_G^{(1)}$, and $\Delta b_q^{(1)}$, which can be found in [92]. However, it is clear that any values of those coefficients can be accommodated by an appropriate choice of b_3 and a_2. This may lead to disagreement between $\Delta G^{(2)}+\Delta G^{(3)}$ and $\Delta\tilde{G}^{(2)}+\Delta\tilde{G}^{(3)}$, but it is possible that such disagreement could be ascribed to the scheme dependence of the gluon hPDF.

E. Exploring the scheme dependence

At this point it appears that there is a difference between the hPDFs resulting from the iterative solution of our large-N_c & N_f evolution equation (59) and the $\overline{\mathrm{MS}}$ hPDFs. Here we explore the possibility that the difference is solely due to the scheme dependence.

Suppose the hPDFs we obtained using Eq. (59) satisfy DGLAP evolution equations

$$\frac{\partial}{\partial\ln Q^2}\begin{pmatrix}\Delta\Sigma(x,Q^2)\\ \Delta G(x,Q^2)\end{pmatrix} = \int_x^1\frac{dz}{z}\begin{pmatrix}\Delta P_{qq}(z) & \Delta P_{qG}(z)\\ \Delta P_{Gq}(z) & \Delta P_{GG}(z)\end{pmatrix}\begin{pmatrix}\Delta\Sigma(\frac{x}{z},Q^2)\\ \Delta G(\frac{x}{z},Q^2)\end{pmatrix}$$
$$\equiv\left[\Delta\mathbf{P}\otimes\begin{pmatrix}\Delta\Sigma\\ \Delta G\end{pmatrix}\right](x,Q^2) \tag{92}$$

with some unknown helicity splitting functions $\Delta P_{ij}(z)$. If Eq. (92) holds for our hPDFs, then perturbative expansions of the splitting functions $\Delta P_{ij}(z)$ can be obtained using the results of the above iterative solution.

Substituting Eqs. (74), (76), (78), (83), (85), and (89) into Eq. (75), and using it in Eq. (92) order-by-order in α_s, after some algebra we end up with the following splitting functions (at small x and large N_c & N_f) in the pDIS scheme:

$$\Delta P_{qq}(z) = \frac{\alpha_s N_c}{4\pi} + \frac{1}{8}\left(1 - 8\frac{N_f}{N_c}\right)\left(\frac{\alpha_s N_c}{2\pi}\right)^2 \ln^2\frac{1}{z} + \mathcal{O}(\alpha_s^3), \tag{93a}$$

$$\Delta P_{qG}(z) = -\frac{\alpha_s N_f}{2\pi} - \frac{13}{16}\frac{\alpha_s^2 N_c N_f}{\pi^2}\ln^2\frac{1}{z} + \mathcal{O}(\alpha_s^3), \tag{93b}$$

$$\Delta P_{Gq}(z) = \frac{\alpha_s N_c}{2\pi} + \frac{1}{2}\left(\frac{\alpha_s N_c}{\pi}\right)^2 \ln^2\frac{1}{z} + \mathcal{O}(\alpha_s^3), \tag{93c}$$

$$\Delta P_{GG}(z) = 2\frac{\alpha_s N_c}{\pi} + \left(\frac{\alpha_s N_c}{\pi}\right)^2 \ln^2\frac{1}{z} + \mathcal{O}(\alpha_s^3). \tag{93d}$$

Note that the coefficients $\Delta a_i^{(l)}$ and $\Delta b_i^{(l)}$ do not contribute to the splitting functions (93) at the shown orders in α_s: at the orders α_s and α_s^2 these coefficients do not contribute to Eq. (92), while at the order α_s^3 they only affect the Q^2-independent terms, which contribute to the polarized splitting functions only at NNLO. Therefore, for the LO + NLO splitting functions (93) we can ignore the difference between the factorized and unfactorized expressions for the g_1 structure function and $\Delta\Sigma$.

If our hPDFs were different from the ones in the $\overline{\text{MS}}$ scheme only by the scheme dependence, then the two would be related by (see e.g. [86,88])

$$\begin{pmatrix} \Delta\Sigma(x, Q^2) \\ \Delta G(x, Q^2) \end{pmatrix} = \left[\mathbf{\Delta C} \otimes \begin{pmatrix} \Delta\tilde{\Sigma} \\ \Delta\tilde{G} \end{pmatrix}\right](x, Q^2), \tag{94}$$

with some unknown matrix of coefficient functions,

$$\mathbf{\Delta C}(z) = \begin{pmatrix} z\delta(1-z) + \alpha_s \Delta C_{qq}^{(1)} \ln\frac{1}{z} + \alpha_s^2 \Delta C_{qq}^{(2)} \ln^3\frac{1}{z} + \dots & \alpha_s \Delta C_{qG}^{(1)} \ln\frac{1}{z} + \alpha_s^2 \Delta C_{qG}^{(2)} \ln^3\frac{1}{z} + \dots \\ \alpha_s \Delta C_{Gq}^{(1)} \ln\frac{1}{z} + \alpha_s^2 \Delta C_{Gq}^{(2)} \ln^3\frac{1}{z} + \dots & z\delta(1-z) + \alpha_s \Delta C_{GG}^{(1)} \ln\frac{1}{z} + \alpha_s^2 \Delta C_{GG}^{(2)} \ln^3\frac{1}{z} + \dots \end{pmatrix}. \tag{95}$$

Equation (94) implies that

$$\mathbf{\Delta P} = \mathbf{\Delta C} \otimes \mathbf{\Delta\tilde{P}} \otimes \mathbf{\Delta C}^{-1}, \tag{96}$$

with $\tilde{\mathbf{P}}$ the splitting function matrix in the $\overline{\text{MS}}$ scheme. Rewriting Eq. (96) as

$$\mathbf{\Delta P} \otimes \mathbf{\Delta C} = \mathbf{\Delta C} \otimes \mathbf{\Delta\tilde{P}} \tag{97}$$

allows one to construct the coefficients (95) order-by-order in α_s.

At the order-α_s the splitting functions are the same in pDIS and $\overline{\text{MS}}$ schemes, cf. Eqs. (61) and (61). Hence Eq. (97) is trivially satisfied at this order.

At the order-α_s^2, Eq. (97) gives the following conditions,

$$N_f \Delta C_{Gq}^{(1)} + N_c \Delta C_{qG}^{(1)} = -\frac{N_c N_f}{2\pi}, \tag{98a}$$

$$\frac{N_f}{2}\Delta C_{qq}^{(1)} - \frac{7}{4}N_c \Delta C_{qG}^{(1)} - \frac{N_f}{2}\Delta C_{GG}^{(1)} = \frac{N_c N_f}{\pi}, \tag{98b}$$

$$\Delta C_{qq}^{(1)} + \frac{7}{2}\Delta C_{Gq}^{(1)} - \Delta C_{GG}^{(1)} = -\frac{3N_c}{4\pi}. \tag{98c}$$

Equation (98) do not have a solution for $N_f \neq 0$. Therefore, the difference between our hPDFs and the ones in the $\overline{\text{MS}}$ scheme cannot be entirely attributed to the scheme dependence, putting our interpretation of the earlier cross-checks in question.

F. Further discussion

The origin of the discrepancies found above is not clear to us at the moment. Indeed, since all the discrepancies come with a factor of N_f, one may suspect that some quark contributions are missing in the evolution of [1]. A possible missing piece could be due to the terms where an s-channel quark becomes a gluon (and *vice versa*) after interacting with the shock wave. Such contributions were considered in [2], see Sec. IV there, where they were argued not to contribute to the flavor-singlet helicity evolution at DLA. These contributions appear to contribute to the flavor nonsinglet helicity evolution, as was argued in [3], but at the subleading-N_c order. The contribution of quark-to-gluon and gluon-to-quark transition terms has been studied in detail in [14]. If such terms do contribute to the flavor-singlet helicity evolution, perhaps due to some loophole in the arguments of [2,3], it appears difficult to include them into any closed-form evolution equations at large-N_c & N_f.

However, let us explore another possibility here, by considering the exact solution of small-x helicity evolution equations in the large-N_c case from [17]. For our initial condition (73), we substitute Eqs. (63) from [17] into

Eq. (58) in the same reference, multiply the result by $\alpha_s \pi^2/(2N_c)$, obtaining

$$\Delta\Sigma(x, Q^2) = -\frac{N_f}{4N_c} \int \frac{d\omega}{2\pi i} e^{\omega \ln\frac{1}{x}} \left[\frac{1}{\omega - \Delta\gamma_{GG}(\omega)} e^{\Delta\gamma_{GG}(\omega) \ln(\frac{Q^2}{\Lambda^2})} - \frac{1}{\omega} \right]. \tag{99}$$

Similarly, Eq. (64) in [17], multiplied by $\alpha_s \pi^2/(2N_c)$, gives

$$\Delta G(x, Q^2) = \int \frac{d\omega}{2\pi i} e^{\omega \ln\frac{1}{x} + \Delta\gamma_{GG}(\omega) \ln(\frac{Q^2}{\Lambda^2})} \frac{1}{\omega}. \tag{100}$$

The anomalous dimension $\Delta\gamma_{GG}(\omega)$ is given in Eq. (65) of the same reference,

$$\Delta\gamma_{GG}(\omega) = \frac{\omega}{2} \left[1 - \sqrt{1 - \frac{16\bar{\alpha}_s}{\omega^2} \sqrt{1 - \frac{4\bar{\alpha}_s}{\omega^2}}} \right] \tag{101}$$

with

$$\bar{\alpha}_s \equiv \frac{\alpha_s N_c}{2\pi}. \tag{102}$$

Next, let us compare this to the solution of DGLAP equations in the same approximation. At fixed coupling (as is the case in DLA), the solution of DGLAP equation (92) is

$$\begin{pmatrix} \Delta\Sigma(x, Q^2) \\ \Delta G(x, Q^2) \end{pmatrix} = \int \frac{d\omega}{2\pi i} e^{\omega \ln\frac{1}{x}} \begin{pmatrix} \Delta\Sigma_\omega(Q^2) \\ \Delta G_\omega(Q^2) \end{pmatrix} = \int \frac{d\omega}{2\pi i} e^{\omega \ln\frac{1}{x}} \exp\left\{ \begin{pmatrix} \Delta\gamma_{qq}(\omega) & \Delta\gamma_{qG}(\omega) \\ \Delta\gamma_{Gq}(\omega) & \Delta\gamma_{GG}(\omega) \end{pmatrix} \ln\frac{Q^2}{\Lambda^2} \right\} \begin{pmatrix} \Delta\Sigma_\omega(\Lambda^2) \\ \Delta G_\omega(\Lambda^2) \end{pmatrix}. \tag{103}$$

Defining the eigenvalues

$$\lambda_1 = \frac{1}{2} \left[\Delta\gamma_{qq} + \Delta\gamma_{GG} + \sqrt{(\Delta\gamma_{qq} - \Delta\gamma_{GG})^2 + 4\Delta\gamma_{qG}\Delta\gamma_{Gq}} \right] \ln\frac{Q^2}{\Lambda^2}, \tag{104a}$$

$$\lambda_2 = \frac{1}{2} \left[\Delta\gamma_{qq} + \Delta\gamma_{GG} - \sqrt{(\Delta\gamma_{qq} - \Delta\gamma_{GG})^2 + 4\Delta\gamma_{qG}\Delta\gamma_{Gq}} \right] \ln\frac{Q^2}{\Lambda^2}, \tag{104b}$$

we rewrite Eq. (103) as

$$\begin{pmatrix} \Delta\Sigma(x, Q^2) \\ \Delta G(x, Q^2) \end{pmatrix} = \int \frac{d\omega}{2\pi i} e^{\omega \ln\frac{1}{x}} \begin{pmatrix} \frac{e^{\lambda_1} + e^{\lambda_2}}{2} + (\Delta\gamma_{qq} - \Delta\gamma_{GG}) \frac{e^{\lambda_1} - e^{\lambda_2}}{2(\lambda_1 - \lambda_2)} \ln\frac{Q^2}{\Lambda^2} & \Delta\gamma_{qG} \frac{e^{\lambda_1} - e^{\lambda_2}}{\lambda_1 - \lambda_2} \ln\frac{Q^2}{\Lambda^2} \\ \Delta\gamma_{Gq} \frac{e^{\lambda_1} - e^{\lambda_2}}{\lambda_1 - \lambda_2} \ln\frac{Q^2}{\Lambda^2} & \frac{e^{\lambda_1} + e^{\lambda_2}}{2} - (\Delta\gamma_{qq} - \Delta\gamma_{GG}) \frac{e^{\lambda_1} - e^{\lambda_2}}{2(\lambda_1 - \lambda_2)} \ln\frac{Q^2}{\Lambda^2} \end{pmatrix} \begin{pmatrix} \Delta\Sigma_\omega(\Lambda^2) \\ \Delta G_\omega(\Lambda^2) \end{pmatrix}. \tag{105}$$

If we take $\Delta\Sigma(x, \Lambda^2) = 0$, $\Delta G(x, \Lambda^2) = 1$ initial conditions, as we did above, then $\Delta\Sigma_\omega(\Lambda^2) = 0$ and $\Delta G_\omega(\Lambda^2) = 1/\omega$. Further, we remove all quarks except for the "last one" giving $\Delta\Sigma$, that is put $\Delta\gamma_{qq} = \Delta\gamma_{Gq} = 0$ everywhere and $\Delta\gamma_{qG} = 0$ everywhere except for the explicit factor of $\Delta\gamma_{qG}$ in the upper right corner of the matrix in Eq. (105). This leads to $\lambda_1 = \Delta\gamma_{GG} \ln\frac{Q^2}{\Lambda^2}$ and $\lambda_2 = 0$. Using all this in Eq. (105) yields

$$\begin{pmatrix} \Delta\Sigma(x, Q^2) \\ \Delta G(x, Q^2) \end{pmatrix} = \int \frac{d\omega}{2\pi i} e^{\omega \ln\frac{1}{x}} \begin{pmatrix} 1 & \Delta\gamma_{qG} \frac{e^{\Delta\gamma_{GG} \ln\frac{Q^2}{\Lambda^2}} - 1}{\Delta\gamma_{GG}} \\ 0 & e^{\Delta\gamma_{GG} \ln\frac{Q^2}{\Lambda^2}} \end{pmatrix} \begin{pmatrix} 0 \\ \frac{1}{\omega} \end{pmatrix}. \tag{106}$$

Specifically, for $\Delta\Sigma$ we get

$$\Delta\Sigma(x,Q^2) = \int \frac{d\omega}{2\pi i} \frac{\Delta\gamma_{qG}(\omega)}{\Delta\gamma_{GG}(\omega)} e^{\omega \ln\frac{1}{x}} \left[e^{\Delta\gamma_{GG}(\omega)\ln\frac{Q^2}{\Lambda^2}} - 1 \right] \frac{1}{\omega}, \tag{107}$$

while for ΔG we get exactly Eq. (100).

Equation (107) is not the same as Eq. (99). The anomalous dimensions in the exponents are the same, $\Delta\gamma_{GG}(\omega)$ and 0. However, the prefactors of the exponents are different. If we expand the prefactors in Eqs. (99) and (107) to the lowest order in α_s we would get

$$\Delta\Sigma(x,Q^2) \approx -\frac{N_f}{\alpha_s 2\pi^2} \int \frac{d\omega}{2\pi i} e^{\omega \ln\frac{1}{x}} \left[e^{\gamma_{\omega}^{-} \ln(\frac{Q^2}{\Lambda^2})} - 1 \right] \frac{1}{\omega} \tag{108}$$

from both of them, since

$$\frac{\Delta\gamma_{qG}^{(1)}(\omega)}{\Delta\gamma_{GG}^{(1)}(\omega)} = -\frac{N_f}{4N_c}. \tag{109}$$

However, the agreement between Eqs. (99) and (107) ends beyond this leading order in α_s in the prefactor. Moreover, no scheme dependence, that is, no choice of $\Delta\gamma_{qG}$ and $\Delta\gamma_{GG}$ beyond LO would make Eqs. (99) and (107) agree. Therefore, already at large N_c we cannot attribute the difference between our result and that of DGLAP + coefficient functions calculation to a different scheme.

If we modify the initial conditions for DGLAP evolution to be (note the nontrivial quark hPDF)

$$\begin{pmatrix} \Delta\Sigma_\omega(\Lambda^2) \\ \Delta G_\omega(\Lambda^2) \end{pmatrix} = \begin{pmatrix} -\frac{N_f}{4N_c} \frac{1}{\omega} \frac{\Delta\gamma_{GG}(\omega)}{\omega - \Delta\gamma_{GG}(\omega)} \\ \frac{1}{\omega} \end{pmatrix} \tag{110}$$

and rewrite Eq. (106) as

$$\begin{pmatrix} \Delta\Sigma(x,Q^2) \\ \Delta G(x,Q^2) \end{pmatrix} = \int \frac{d\omega}{2\pi i} e^{\omega\ln\frac{1}{x}} \begin{pmatrix} 1 & \Delta\gamma_{qG} \frac{e^{\Delta\gamma_{GG}\ln\frac{Q^2}{\Lambda^2}} - 1}{\Delta\gamma_{GG}} \\ 0 & e^{\Delta\gamma_{GG}\ln\frac{Q^2}{\Lambda^2}} \end{pmatrix} \times \begin{pmatrix} -\frac{N_f}{4N_c} \frac{1}{\omega} \frac{\Delta\gamma_{GG}(\omega)}{\omega - \Delta\gamma_{GG}(\omega)} \\ \frac{1}{\omega} \end{pmatrix}, \tag{111}$$

then ΔG would remain the same, while $\Delta\Sigma$ would agree with Eq. (99) if the following relation holds for the large-N_c small-x anomalous dimensions:

$$\Delta\gamma_{qG}(\omega) = -\frac{N_f}{4N_c} \frac{\omega\Delta\gamma_{GG}(\omega)}{\omega - \Delta\gamma_{GG}(\omega)}. \tag{112}$$

However, this relation appears to be unlikely to hold to all orders in α_s: it already breaks down beyond the leading order in α_s in the $\overline{\text{MS}}$ scheme.

Let us finally add that the gluon hPDF in Eq. (100), satisfying large-N_c small-x DGLAP evolution, is obtained in the exact solution from [17] only for a very specific initial conditions, corresponding to $\Delta G^{(0)}(x,Q^2) = \text{const}$ and $\Delta\Sigma^{(0)}(x,Q^2) = 0$. Other initial conditions for the small-x large-N_c helicity evolution result in expressions for $\Delta G(x,Q^2)$ which, while still containing the anomalous dimension (101), do not look quite as simple as Eq. (100). Therefore, our efforts to compare iterative solution of Eq. (59) also appear to be strongly dependent on the choice of the initial conditions, making the choice in Eq. (73) just one option, which does not necessarily make the resulting hPDFs agree with the DGLAP-based approaches. This conclusion is further corroborated by the fact that modifying the initial conditions (73) to

$$G_2^{(0)} = \frac{\alpha_s\pi^2}{2N_c}\delta(zsx_{10}^2 - 1), \qquad Q^{(0)} = \tilde{G}^{(0)} = 0, \tag{113}$$

results in disagreement between the polarized DGLAP and the iterative solution of Eq. (59) at lower orders in α_s than what we observed above.

VI. CONCLUSIONS

To conclude, let us reiterate our main results. We have numerically solved the revised version of the large-N_c & N_f helicity evolution equations at small-x [1], given above in Eq. (13). The solution exhibited qualitatively different behavior depending on whether $N_f < 2N_c$ or $N_f = 2N_c$. For $N_f < 2N_c$ all the polarized dipole amplitudes grow exponentially in rapidity (or, equivalently, with the logarithm of energy). The corresponding intercepts are summarized in Table III. Comparing these intercepts with the earlier work by BER [34] in Table IV, we observe the discrepancy at the 2%–3% level, larger than our numerical precision but small enough not to be important for phenomenological applications. Similar, albeit smaller ($< 0.1\%$) discrepancy with BER has recently been observed in the analytic solution of the revised large-N_c helicity evolution equations from [1] constructed in [17], where the origin of the discrepancy was traced down to the difference in the resummed polarized GG anomalous dimensions.

For $N_f = 2N_c$ our numerical solution of Eq. (13) oscillates in $\ln(1/x)$ with the exponentially growing amplitude. This behavior of the solution for the revised evolution equations at $N_f = 2N_c$ is reminiscent of the solution for the earlier version of the large-N_c & N_f helicity evolution equations constructed in [4]. The relevant parameters are summarized in the Table VII above. We noted that the oscillation period may be too high for the experimental detection of these oscillations.

In addition, we have studied the dependence of the small-x asymptotics on the initial conditions for the evolution. We found that the intercepts and the oscillation frequency (the latter for $N_f = 2N_c$) are rather insensitive to the initial conditions (see Tables VIII–XI). The initial phase of the oscillations (also for $N_f = 2N_c$) appears to depend rather strongly on the initial conditions (cf. [4]). We have also verified the target–projectile symmetry of the revised equations solution: this symmetry appeared to be missing in the earlier helicity evolution equations [2,3,6].

Finally, we have performed some limited cross-checks of the iterative solution of the revised large-N_c & N_f helicity evolution equations against the known finite-order calculations in the collinear factorization framework [81–92]. The results were inconclusive: despite observing a good degree of agreement between the two approaches, we found some discrepancies as well, potentially related to our choice of the initial conditions for the helicity evolution. The investigation into the origin of these discrepancies is left for future work, which may involve an exact analytic solution of Eq. (59) using the technique of [17]. Using our disagreement with BER at large-N_c & N_f as an estimate of the potential error in our approach, and given the smallness of this disagreement, we are optimistic that our difference with polarized DGLAP evolution must also be comparably small. This would imply that our evolution should be sufficiently accurate to be used in further developing phenomenological predictions for the EIC along the lines of [15].

ACKNOWLEDGMENTS

The authors would like to thank Dr. Florian Cougoulic and Dr. Andrey Tarasov for the useful discussion about various aspects of this work. One of the authors (Y. K.) is grateful to Professors Sven-Olaf Moch and Johannes Bluemlein for very helpful and informative discussions of perturbative QCD calculations of helicity parton distributions and the g_1 structure function. This material is based upon work supported by the U.S. Department of Energy, Office of Science, Office of Nuclear Physics under contract No. DE-AC05-06OR23177 and Award No. DE-SC0004286. Y. T. is supported by the Academy of Finland, the Centre of Excellence in Quark Matter and project No. 346567, under the European Union's Horizon 2020 research and innovation programme by the European Research Council (ERC, Grant agreement No. ERC-2018-ADG-835105 YoctoLHC) and by the STRONG-2020 project (Grant agreement No. 824093). The content of this article does not reflect the official opinion of the European Union and responsibility for the information and views expressed therein lies entirely with the authors. The work is performed within the framework of the Saturated Glue (SURGE) Topical Theory Collaboration.

---

[1] F. Cougoulic, Y. V. Kovchegov, A. Tarasov, and Y. Tawabutr, Quark and gluon helicity evolution at small x: Revised and updated, J. High Energy Phys. 07 (2022) 095.

[2] Y. V. Kovchegov, D. Pitonyak, and M. D. Sievert, Helicity evolution at small-x, J. High Energy Phys. 01 (2016) 072.

[3] Y. V. Kovchegov and M. D. Sievert, Small-x helicity evolution: An operator treatment, Phys. Rev. D **99**, 054032 (2019).

[4] Y. V. Kovchegov and Y. Tawabutr, Helicity at small x: Oscillations generated by bringing back the quarks, J. High Energy Phys. 08 (2020) 014.

[5] Y. Hatta, Y. Nakagawa, F. Yuan, Y. Zhao, and B. Xiao, Gluon orbital angular momentum at small-x, Phys. Rev. D **95**, 114032 (2017).

[6] Y. V. Kovchegov, D. Pitonyak, and M. D. Sievert, Helicity evolution at small x: Flavor singlet and non-singlet observables, Phys. Rev. D **95**, 014033 (2017).

[7] Y. V. Kovchegov, D. Pitonyak, and M. D. Sievert, Small-x Asymptotics of the Quark Helicity Distribution, Phys. Rev. Lett. **118**, 052001 (2017).

[8] Y. V. Kovchegov, D. Pitonyak, and M. D. Sievert, Small-x asymptotics of the quark helicity distribution: Analytic results, Phys. Lett. B **772**, 136 (2017).

[9] Y. V. Kovchegov, D. Pitonyak, and M. D. Sievert, Small-x asymptotics of the gluon helicity distribution, J. High Energy Phys. 10 (2017) 198.

[10] Y. V. Kovchegov, Orbital angular momentum at small x, J. High Energy Phys. 03 (2019) 174.

[11] R. Boussarie, Y. Hatta, and F. Yuan, Proton spin structure at small-x, Phys. Lett. B **797**, 134817 (2019).

[12] F. Cougoulic and Y. V. Kovchegov, Helicity-dependent generalization of the JIMWLK evolution, Phys. Rev. D **100**, 114020 (2019).

[13] F. Cougoulic and Y. V. Kovchegov, Helicity-dependent extension of the McLerran-Venugopalan model, Nucl. Phys. **A1004**, 122051 (2020).

[14] G. A. Chirilli, High-energy operator product expansion at sub-eikonal level, J. High Energy Phys. 06 (2021) 096.

[15] D. Adamiak, Y. V. Kovchegov, W. Melnitchouk, D. Pitonyak, N. Sato, and M. D. Sievert, First analysis of world polarized DIS data with small-x helicity evolution, Phys. Rev. D **104**, L031501 (2021).

[16] Y. V. Kovchegov, A. Tarasov, and Y. Tawabutr, Helicity evolution at small x: The single-logarithmic contribution, J. High Energy Phys. 03 (2022) 184.

[17] J. Borden and Y. V. Kovchegov, Analytic solution for the revised helicity evolution at small x and large N_c:

New resummed gluon-gluon polarized anomalous dimension and intercept, Phys. Rev. D **108**, 014001 (2023).

[18] C. A. Aidala, S. D. Bass, D. Hasch, and G. K. Mallot, The spin structure of the nucleon, Rev. Mod. Phys. **85**, 655 (2013).

[19] A. Accardi *et al.*, Electron ion collider: The next QCD frontier, Eur. Phys. J. A **52**, 268 (2016).

[20] E. Leader and C. Lorcé, The angular momentum controversy: What's it all about and does it matter?, Phys. Rep. **541**, 163 (2014).

[21] E. C. Aschenauer *et al.*, The RHIC spin program: Achievements and future opportunities, arXiv:1304.0079.

[22] E.-C. Aschenauer *et al.*, The RHIC SPIN Program: Achievements and future opportunities, arXiv:1501.01220.

[23] D. Boer *et al.*, Gluons and the quark sea at high energies: Distributions, polarization, tomography, arXiv:1108.1713.

[24] *Proceedings, Probing Nucleons and Nuclei in High Energy Collisions: Dedicated to the Physics of the Electron Ion Collider: Seattle (WA), United States, 2018*, edited by A. Prokudin, Y. Hatta, Y. Kovchegov, and C. Marquet (World Scientific Press, Singapore, 2020).

[25] X. Ji, F. Yuan, and Y. Zhao, What we know and what we don't know about the proton spin after 30 years, Nat. Rev. Phys. **3**, 27 (2021).

[26] R. Abdul Khalek *et al.*, Science requirements and detector concepts for the electron-ion collider: EIC Yellow Report, Nucl. Phys. **A1026**, 122447 (2022).

[27] R. L. Jaffe and A. Manohar, The G(1) problem: Fact and fantasy on the spin of the proton, Nucl. Phys. **B337**, 509 (1990).

[28] X.-D. Ji, Gauge-Invariant Decomposition of Nucleon Spin, Phys. Rev. Lett. **78**, 610 (1997).

[29] S. Bashinsky and R. L. Jaffe, Quark and gluon orbital angular momentum and spin in hard processes, Nucl. Phys. **B536**, 303 (1998).

[30] P. Hagler and A. Schafer, Evolution equations for higher moments of angular momentum distributions, Phys. Lett. B **430**, 179 (1998).

[31] A. Harindranath and R. Kundu, On orbital angular momentum in deep inelastic scattering, Phys. Rev. D **59**, 116013 (1999).

[32] Y. Hatta and S. Yoshida, Twist analysis of the nucleon spin in QCD, J. High Energy Phys. 10 (2012) 080.

[33] X. Ji, X. Xiong, and F. Yuan, Probing parton orbital angular momentum in longitudinally polarized nucleon, Phys. Rev. D **88**, 014041 (2013).

[34] J. Bartels, B. Ermolaev, and M. Ryskin, Flavor singlet contribution to the structure function G(1) at small x, Z. Phys. C **72**, 627 (1996).

[35] J. Bartels, B. Ermolaev, and M. Ryskin, Nonsinglet contributions to the structure function g1 at small x, Z. Phys. C **70**, 273 (1996).

[36] V. G. Gorshkov, V. N. Gribov, L. N. Lipatov, and G. V. Frolov, Doubly logarithmic asymptotic behavior in quantum electrodynamics, Sov. J. Nucl. Phys. **6**, 95 (1968).

[37] R. Kirschner and L. Lipatov, Double logarithmic asymptotics and Regge singularities of quark amplitudes with flavor exchange, Nucl. Phys. **B213**, 122 (1983).

[38] R. Kirschner, Reggeon interactions in perturbative QCD, Z. Phys. C **65**, 505 (1995).

[39] R. Kirschner, Regge asymptotics of scattering with flavor exchange in QCD, Z. Phys. C **67**, 459 (1995).

[40] S. Griffiths and D. Ross, Studying the perturbative Reggeon, Eur. Phys. J. C **12**, 277 (2000).

[41] J. Blumlein and A. Vogt, On the behavior of nonsinglet structure functions at small x, Phys. Lett. B **370**, 149 (1996).

[42] J. Blümlein and A. Vogt, The singlet contribution to the structure function g1 (x, Q**2) at small x, Phys. Lett. B **386**, 350 (1996).

[43] B. I. Ermolaev, M. Greco, and S. I. Troian, QCD running coupling effects for the nonsinglet structure function at small x, Nucl. Phys. **B571**, 137 (2000).

[44] B. I. Ermolaev, M. Greco, and S. I. Troyan, Intercepts of the nonsinglet structure functions, Nucl. Phys. **B594**, 71 (2001).

[45] B. I. Ermolaev, M. Greco, and S. I. Troyan, Running coupling effects for the singlet structure function g_1 at small x, Phys. Lett. B **579**, 321 (2004).

[46] B. I. Ermolaev, M. Greco, and S. I. Troyan, Overview of the spin structure function g_1 at arbitrary x and Q^2, Riv. Nuovo Cimento **33**, 57 (2010).

[47] A. H. Mueller, Soft gluons in the infinite momentum wave function and the BFKL pomeron, Nucl. Phys. **B415**, 373 (1994).

[48] A. H. Mueller and B. Patel, Single and double BFKL pomeron exchange and a dipole picture of high-energy hard processes, Nucl. Phys. **B425**, 471 (1994).

[49] A. H. Mueller, Unitarity and the BFKL pomeron, Nucl. Phys. **B437**, 107 (1995).

[50] I. Balitsky, Operator expansion for high-energy scattering, Nucl. Phys. **B463**, 99 (1996).

[51] I. Balitsky, Factorization and high-energy effective action, Phys. Rev. D **60**, 014020 (1999).

[52] Y. V. Kovchegov, Small-x F_2 structure function of a nucleus including multiple pomeron exchanges, Phys. Rev. D **60**, 034008 (1999).

[53] Y. V. Kovchegov, Unitarization of the BFKL pomeron on a nucleus, Phys. Rev. D **61**, 074018 (2000).

[54] J. Jalilian-Marian, A. Kovner, and H. Weigert, The Wilson renormalization group for low x physics: Gluon evolution at finite parton density, Phys. Rev. D **59**, 014015 (1998).

[55] J. Jalilian-Marian, A. Kovner, A. Leonidov, and H. Weigert, The Wilson renormalization group for low x physics: Towards the high density regime, Phys. Rev. D **59**, 014014 (1998).

[56] H. Weigert, Unitarity at small Bjorken x, Nucl. Phys. **A703**, 823 (2002).

[57] E. Iancu, A. Leonidov, and L. D. McLerran, The renormalization group equation for the color glass condensate, Phys. Lett. B **510**, 133 (2001).

[58] E. Iancu, A. Leonidov, and L. D. McLerran, Nonlinear gluon evolution in the color glass condensate. I, Nucl. Phys. **A692**, 583 (2001).

[59] E. Ferreiro, E. Iancu, A. Leonidov, and L. McLerran, Nonlinear gluon evolution in the color glass condensate. II, Nucl. Phys. **A703**, 489 (2002).

[60] L. V. Gribov, E. M. Levin, and M. G. Ryskin, Semihard processes in QCD, Phys. Rep. **100**, 1 (1983).

[61] E. Iancu and R. Venugopalan, The color glass condensate and high-energy scattering in QCD, in *QuarkGluon Plasma 3* (World Scientific, Singapore, 2003).

[62] H. Weigert, Evolution at small x_{bj}: The color glass condensate, Prog. Part. Nucl. Phys. **55**, 461 (2005).

[63] J. Jalilian-Marian and Y. V. Kovchegov, Saturation physics and deuteron-Gold collisions at RHIC, Prog. Part. Nucl. Phys. **56**, 104 (2006).

[64] F. Gelis, E. Iancu, J. Jalilian-Marian, and R. Venugopalan, The color glass condensate, Annu. Rev. Nucl. Part. Sci. **60**, 463 (2010).

[65] J. L. Albacete and C. Marquet, Gluon saturation and initial conditions for relativistic heavy ion collisions, Prog. Part. Nucl. Phys. **76**, 1 (2014).

[66] Y. V. Kovchegov and E. Levin, *Quantum Chromodynamics at High Energy* (Cambridge University Press, Cambridge, England, 2012), Vol. 33.

[67] A. Morreale and F. Salazar, Mining for gluon saturation at colliders, Universe **7**, 312 (2021).

[68] T. Altinoluk, N. Armesto, G. Beuf, M. Martinez, and C. A. Salgado, Next-to-eikonal corrections in the CGC: Gluon production and spin asymmetries in pA collisions, J. High Energy Phys. 07 (2014) 068.

[69] I. Balitsky and A. Tarasov, Rapidity evolution of gluon TMD from low to moderate x, J. High Energy Phys. 10 (2015) 017.

[70] I. Balitsky and A. Tarasov, Gluon TMD in particle production from low to moderate x, J. High Energy Phys. 06 (2016) 164.

[71] G. A. Chirilli, Sub-eikonal corrections to scattering amplitudes at high energy, J. High Energy Phys. 01 (2019) 118.

[72] J. Jalilian-Marian, Quark jets scattering from a gluon field: From saturation to high p_t, Phys. Rev. D **99**, 014043 (2019).

[73] J. Jalilian-Marian, Rapidity loss, spin and angular asymmetries in scattering of a quark from color field of a proton (nucleus), Phys. Rev. D **102**, 014008 (2020).

[74] T. Altinoluk, G. Beuf, A. Czajka, and A. Tymowska, Quarks at next-to-eikonal accuracy in the CGC I: Forward quark-nucleus scattering, Phys. Rev. D **104**, 014019 (2021).

[75] Y. V. Kovchegov and M. G. Santiago, Quark sivers function at small x: Spin-dependent odderon and the sub-eikonal evolution, J. High Energy Phys. 11 (2021) 200.

[76] T. Altinoluk and G. Beuf, Quark and scalar propagators at next-to-eikonal accuracy in the CGC through a dynamical background gluon field, Phys. Rev. D **105**, 074026 (2022).

[77] Y. V. Kovchegov and M. G. Santiago, T-odd leading-twist quark TMDs at small x, J. High Energy Phys. 11 (2022) 098.

[78] T. Altinoluk, G. Beuf, A. Czajka, and A. Tymowska, DIS dijet production at next-to-eikonal accuracy in the CGC, Phys. Rev. D **107**, 074016 (2023).

[79] T. Altinoluk, N. Armesto, and G. Beuf, Probing quark transverse momentum distributions in the color glass condensate: Quark-gluon dijets in deep inelastic scattering at next-to-eikonal accuracy, arXiv:2303.12691.

[80] T. Altinoluk, G. Beuf, and J. Jalilian-Marian, Renormalization of the gluon distribution function in the background field formalism, arXiv:2305.11079.

[81] G. Altarelli and G. Parisi, Asymptotic freedom in parton language, Nucl. Phys. **B126**, 298 (1977).

[82] Y. L. Dokshitzer, Calculation of the structure functions for deep inelastic scattering and e^+e^- annihilation by perturbation theory in quantum chromodynamics, Sov. Phys. JETP **46**, 641 (1977).

[83] E. B. Zijlstra and W. L. van Neerven, Order-α_s^2 corrections to the polarized structure function $g_1(x, Q^2)$, Nucl. Phys. **B417**, 61 (1994).

[84] R. Mertig and W. L. van Neerven, The calculation of the two loop spin splitting functions P(ij)(1)(x), Z. Phys. C **70**, 637 (1996).

[85] S. Moch and J. A. M. Vermaseren, Deep inelastic structure functions at two loops, Nucl. Phys. **B573**, 853 (2000).

[86] W. L. van Neerven and A. Vogt, NNLO evolution of deep inelastic structure functions: The singlet case, Nucl. Phys. **B588**, 345 (2000).

[87] J. A. M. Vermaseren, A. Vogt, and S. Moch, The third-order QCD corrections to deep-inelastic scattering by photon exchange, Nucl. Phys. **B724**, 3 (2005).

[88] S. Moch, J. A. M. Vermaseren, and A. Vogt, The three-loop splitting functions in QCD: The helicity-dependent case, Nucl. Phys. **B889**, 351 (2014).

[89] J. Blümlein, P. Marquard, C. Schneider, and K. Schönwald, The three-loop polarized singlet anomalous dimensions from off-shell operator matrix elements, J. High Energy Phys. 01 (2022) 193.

[90] J. Blümlein and M. Saragnese, The N3LO scheme-invariant QCD evolution of the non-singlet structure functions F2NS(x,Q2) and g1NS(x,Q2), Phys. Lett. B **820**, 136589 (2021).

[91] J. Davies, C. H. Kom, S. Moch, and A. Vogt, Resummation of small-x double logarithms in QCD: Inclusive deep-inelastic scattering, J. High Energy Phys. 08 (2022) 135.

[92] J. Blümlein, P. Marquard, C. Schneider, and K. Schönwald, The massless three-loop Wilson coefficients for the deep-inelastic structure functions F_2, F_L, xF_3 and g_1, J. High Energy Phys. 11 (2022) 156.

[93] G. 't Hooft, A planar diagram theory for strong interactions, Nucl. Phys. **B72**, 461 (1974).

[94] G. Veneziano, Some aspects of a unified approach to gauge, dual and Gribov theories, Nucl. Phys. **B117**, 519 (1976).

[95] H. Akaike, A new look at the statistical model identification, IEEE Trans. Autom. Control **19**, 716 (1974).

[96] V. N. Gribov and L. N. Lipatov, Deep inelastic e p scattering in perturbation theory, Sov. J. Nucl. Phys. **15**, 438 (1972).

[97] J. Ethier, N. Sato, and W. Melnitchouk, First Simultaneous Extraction of Spin-Dependent Parton Distributions and Fragmentation Functions from a Global QCD Analysis, Phys. Rev. Lett.**119**, 132001 (2017).

[98] G. Altarelli, R. K. Ellis, and G. Martinelli, Large perturbative corrections to the Drell-Yan process in QCD, Nucl. Phys. **B157**, 461 (1979).